Progress in Nuclear Magnetic Resonance Spectroscopy 57 (2010) 241–292

Contents lists available at ScienceDirect

Progress in Nuclear Magnetic Resonance Spectroscopy

journal homepage: www.elsevier.com/locate/pnmrs

Single-scan multidimensional magnetic resonance

Assaf Tal, Lucio Frydman *

The Department of Chemical Physics, Weizmann Institute of Science, Israel

ARTICLE INFO

Article history:
Received 22 January 2010
Accepted 23 March 2010
Available online 22 April 2010

Contents

* Corresponding author. Tel.: +972 8 9344903; fax: +972 8 9344123.
E-mail address: lucio.frydman@weizmann.ac.il (L. Frydman).

0079-6565/$ - see front matter
doi:10.1016/j.pnmrs.2010.04.001

1. Introduction

Nuclear Magnetic Resonance (NMR, also known as Magnetic Resonance Spectroscopy; MRS, in an *in-vivo* setting) enables one to probe the structure and dynamics of matter in a noninvasive manner. It allows one to study molecular properties and interactions with unparalleled detail [1–3], and it can be combined with localization techniques to perform Magnetic Resonance Imaging (MRI), i.e., to obtain spatial distribution maps of these and other properties without ever having to "see" the sample [4–6].

The introduction of ever more advanced theories and of more sophisticated concepts has enabled the constant development of increasingly elaborate methods in both NMR and MRI. Also involved in this 60+-years saga have been constant improvements in the hardware and software used to collect the MR data. These developments began in the early days of continuous wave NMR and have continued unabated ever since. In this review we discuss one such development, which departs from the usual time and frequency domain experiments, and relies on spatial encoding; that is, on the selective excitation of spins situated at different positions in the sample in a discriminative manner, and on the subsequent acquisition in the presence of spatial gradients. New manipulations will be examined, and it will be shown how they can be used advantageously. In NMR spectroscopy, such excitations will be useful for acquiring 2D, and in general nD, spectra on a sub-second timescale and in a single-scan [7–9]. Such methods will be dubbed ultrafast 2D NMR (UFNMR). In MRI it will be shown that spatial encoding offers a novel approach to single-scan imaging, which can overcome certain complications affecting more traditional schemes, such as field inhomogeneities and chemical-shift related distortions [10–12]. Such single-scan nD methods will be dubbed ultrafast spatially encoded (SPEN) nD MRI (UF SPEN MRI). This article will describe new approaches to collect both NMR spectra and images based on the spatial encodings of the spin interactions in a single-scan. Given the diversity of these worlds, we deem it convenient for the sake of clarity to confine our description to a simplified setting. These simplifications will be many, yet are not meant to confine the generality of the concepts to be discussed, which can often be extended in a straightforward manner. These simplifications will include: (i) a focus on describing the evolution of the spins based on magnetization vectors rather than on spin coherences; (ii) a focus on the chemical shifts in a liquid as the sole internal interaction affecting these magnetizations, while disregarding potential effects of spin–spin couplings, as well as anisotropic or solid media; (iii) a focus on 2D experiments rather than on general nD acquisitions, and (iv) a focus on linear field gradients as the sole source of inhomogeneous broadening affecting the nD NMR/MRI parallelization, even though non-linear gradients and/or orientational effects could also be used.

With these forewords as background, we turn next to spatial encoding and to its uses in 2D NMR and nD MRI.

1.1. Spatial encoding and single-scan 2D NMR spectroscopy

The one-site ↔ one-peak correspondence typical of NMR spectroscopy has powerful connotations regarding the analytical capabilities of the technique. It appeals to the view of molecules as composed of atoms located in chemically distinct sites (as opposed, for example, to views defined by molecular vibrations, masses or electronic transitions) and is aided by the highly predictable nature of the chemical shifts for any given molecular structure. Still, as chemical complexity grows – particularly in the realms of bio-organic and biological systems – the spectral and chemical resolution of basic 1D NMR is found lacking. A solution to this problem came with the dispersion of NMR data into multiple dimensions; these experiments were triggered by a scheme put forward by J. Jeener in the early 1970s [13], and generalized by R.R. Ernst and his coworkers [14]. In two-dimensional (2D) NMR, one begins by suitably exciting the spins onto the $\hat{x}\hat{y}$-plane; following an evolution period of duration t_1, one then applies a mixing sequence, and finally concludes by acquiring a signal proportional to the spins' transverse magnetization during a time t_2:

$$\text{Excitation} - \text{Evolution}\ (t_1) - \text{Mixing} - \text{Acquisition}\ (t_2). \qquad (1)$$

The mixing sequence is designed beforehand, according to the type of interaction involved and/or the information being sought. Ideally, its purpose in correlation experiments is to transfer magnetization from one chemical site to another if a particular kind of interaction exists between them. In less common separation experiments, the evolving spin remains the same during t_1 and t_2, and it is the nature of the interaction affecting it that changes. Many types of mixing sequences have been devised throughout the years, including those highlighting homonuclear *J*-couplings (TOCSY [15] and COSY [16,17]), heteronuclear couplings (HSQC [18], HMQC [19]), and cross-relaxation or chemical exchange (NOESY [20], EXSY [21]). Yet, regardless of the mixing process, all these experiments consist of repeating the basic block in Eq. (1) for many different – and usually equispaced – values of t_1, with each repetition requiring an independent scan. A 2D time-domain data set results from this,

and is subsequently Fourier transformed along both the t_1 and t_2 dimensions to yield the two-dimensional spectrum being sought.

A drawback of this otherwise extremely powerful data acquisition approach is that the acquisition time it involves may end up being dictated by sampling rather than by sensitivity considerations. Moreover, since for maximizing the steady-state response of the t_1 series one must wait a time $\sim T_1$ before repeating the experiment with a different t_1 value, the acquisition of a full 2D spectrum may take minutes, solely on the basis of the indirect-domain sampling considerations. This problem gets exponentially compounded as the dimensionality of the experiment increases, and its compensation has been the subject of extensive efforts over the last years. Indeed, the reduction of such long experimental times would be highly beneficial not just from the practical acquisition-time point of view, but also from a fundamental one: long acquisition processes preclude one from monitoring many processes and/or unstable systems, which would otherwise be ammenable to nD NMR. These include monitoring the dynamics of reactions which occur on short time scales, such as protein folding or chemical exchange reactions of chemically unstable biomolecules, and the use of metastable spin states, such as those arising from hyperpolarization procedures.

The multi-scan nature of nD NMR was found particularly confining within the context of MRI, which is an inherently multidimensional experiment carried out on a sample with ample sensitivity. Proposals that have been made over the years to reduce the minimal number of scans required to collect the nD NMR/MRI data include departing from fast Fourier transform (FT) algorithms and relying instead on techniques such as non-linear sampling, maximum entropy, projection-reconstruction or least square fitting procedures to bypass the typical Nyquist-imposed sampling criteria. Proposals also include the use of small angle excitations and/or other relaxation-enhancement means to shorten to a minimum the time intervals between scans, as well as reliance on multiple receivers. Still, the most dramatic reduction in the time required by experiments came with Mansfield's introduction of Echo Planar Imaging (EPI), which exploits the man-made, gradient-driven nature of the spin interactions arising in MRI to sample entire volumes of the relevant time-domain within a single-scan, as a function of a single acquisition time, t. This extremely powerful concept enabled - among other developments - the advent of real-time, functional MRI. However, its generalization to the acquisition of arbitrary configurations, involving chemical shifts and/or J-couplings which cannot be dictated "at will", has proven much more elusive.

Still, it was shown in 2002 that a dramatic reduction in the number of scans required by any nD NMR/MRI experiments could be achieved, if the canonical Jeener–Ernst paradigm of serial time-domain multi-scan encodings were replaced by an analogous but *parallel* idea [8]: instead of performing N_1 experiments sequentially in time, increasing the value of t_1 with each increment, the sample could be spatially partitioned into spatial elements, and a different t_1 value ascribed to the different partitions. This spatial encoding is a process that can actually be imparted in a single, one-shot fashion. Acquiring the signals originating from the various positions could result in the retrieval of an otherwise conventional spectrum, but in a single-scan. This is the route taken by so-called spatially encoded ultrafast (UF) nD NMR spectroscopy, and by related nD MRI localization methods (Fig. 1).

The upcoming sections will address numerous aspects of these experiments, including how to partition the sample into slices, how to *spatially encode* arbitrary Ω_1 couplings, and how to exploit the position-dependent FIDs to retrieve 2D spectra and images in a single-scan. Before doing so, however, we deem it convenient to

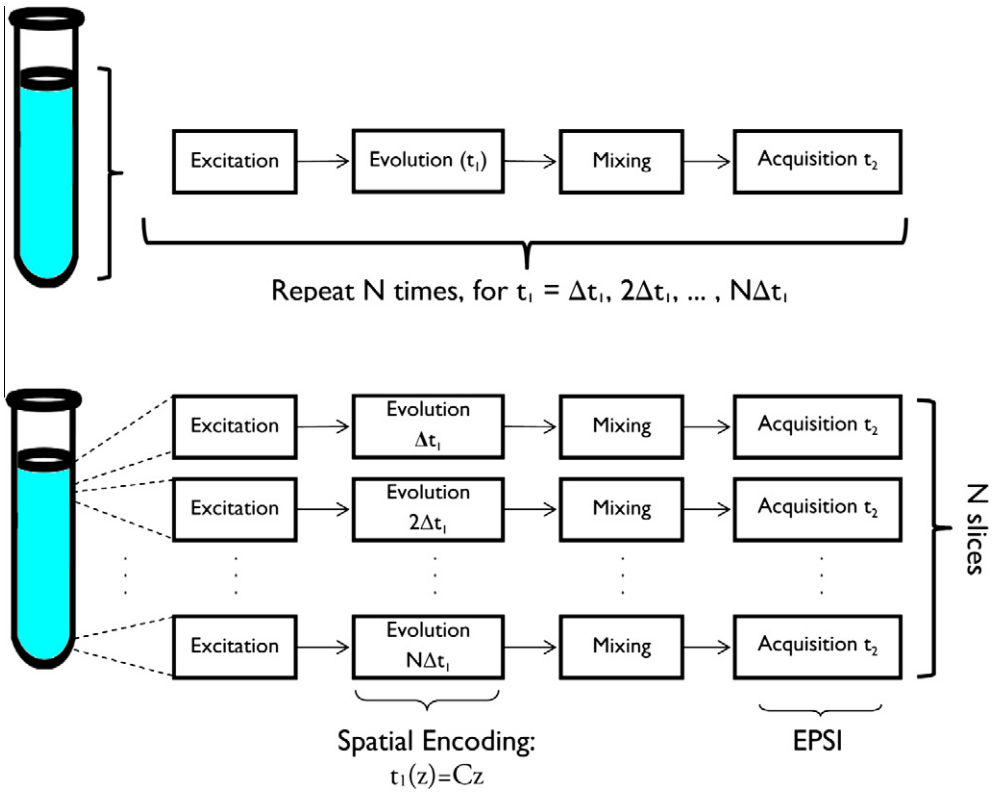

Fig. 1. Above: outline of a conventional 2D NMR experiment. A 1D experiment is repeated N times, each time varying the evolution time t_1. Below: spatially encoded magnetic resonance spectroscopy (UF2DNMR). Instead of executing N experiments sequentially, the sample is spatially partitioned into slices. A set of N different experiments, each with a different t_1 value, are carried out in parallel. A suitable acquisition method capable of probing the magnetization as a function of position is then used to recover the Free Induction Decay (FID) from each slice, once again simultaneously. Thus, it is possible to complete a full 2D NMR acquisition within a single-scan.

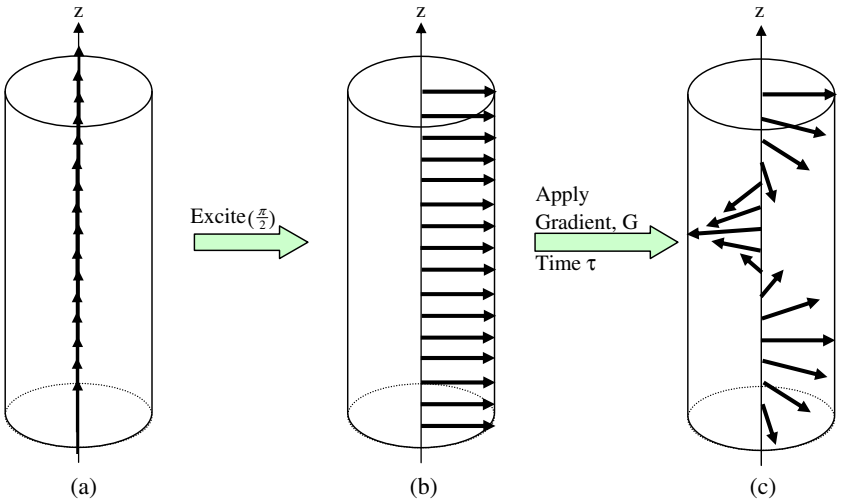

Fig. 2. The effect of a z-gradient, $\mathbf{G} = G\mathbf{z}$. (a) The spins, initially in thermal equilibrium, point in the direction of the field. They are then excited onto the $\hat{x}\hat{y}$-plane (b) using a hard $\frac{\pi}{2}$-pulse. (c) The application of a gradient G for a time τ will cause spins at different positions to precess at different rates, effectively *winding* them along the z-axis. Note that chemical shift evolution is not taken into account in this figure.

introduce a discussion of the effect of linear field gradients – a topic of central importance in contemporary NMR and MRI in general, and in UF 2D NMR/MRI in particular.

2. Elements of spatial encoding

One of the main ingredients involved in the spatial encoding of the indirect-domain interactions is the joint application of field gradients and of frequency-swept pulses. After defining the action of a gradient, this section will elaborate upon the use of pulses whose frequencies are swept linearly in time – also known as chirped pulses [22,23]. Specifically, it will be shown how they can be used to excite, store and flip the spins of the sample sequentially in time and space, and how this can ultimately lead to a different effective t_1 value in each physical portion of the sample.

2.1. The effect of spatial field gradients in NMR

When a sample is placed in a homogeneous magnetic field[1] $\mathbf{B} = B_0\hat{\mathbf{z}}$, the spins in the sample precess about the main field. Different spins will precess at slightly different frequencies, $\gamma(B_0 + \Delta B_0) \equiv \omega_L + \Delta\omega$, where γ is a nucleus-dependent constant known as the *gyromagnetic ratio* of the nucleus; $\omega_L = \gamma B_0$ is the Larmor frequency; and $\Delta\omega = \gamma\Delta B_0$ is a small quantity which depends on the precise chemical environment of the spins as is given by their chemical shift. The ω_L term is shared by all spins of a particular species, and can be accounted for using the so-called rotating frame transformation; hence, in what follows, ω_L will be omitted. Furthermore, a single, particular chemical shift, $\Delta\omega = \Omega_1$, will be the focus of the present analysis.

Linear magnetic field gradients induce a small distortion of the nuclear precession frequencies, which vary linearly throughout the sample along the gradient's direction. Mathematically, these field variations are described by a vector $\mathbf{G}$, specified in units of field per unit length (e.g., Gauss per centimeter, milli-Tesla per meter, etc). The overall precession frequency in the rotating frame in the presence of such a gradient will be given, for a particular chemical site, by a superposition of the chemical shift Ω_1 and an additional term, $\gamma\mathbf{G}\cdot\mathbf{r}$:

$$\omega(\mathbf{r}, t) = \Omega_1 + \gamma\mathbf{G}(t)\cdot\mathbf{r}. \tag{2}$$

Most NMR/MRI spectrometers allow one to vary the gradient, $\mathbf{G}$, as a function of time, and hence a time-dependence has been noted in Eq. (2).

Fig. 2 illustrates the evolution induced by a pulsed DC gradient along the z-axis, $\mathbf{G} = G\mathbf{z}$, following a $\frac{\pi}{2}$ excitation pulse. The spins, initially in thermal equilibrium along the Bloch sphere's $\hat{z}$-axis, are thus tipped onto the $\hat{x}\hat{y}$ plane. Following this, each spin precesses with a frequency proportional to its position, $\omega(z) = \Omega_1 + \gamma Gz$. Pictorially, the effect of such pulsing and constant gradient combination can be described as a winding of the spins (Fig. 2c), as for a given time interval τ, each spin has precessed by a different angle, depending on its z-coordinate. One can also describe this evolution as inducing a *dephasing* of the bulk signal: since the NMR/MRI experiment monitors a vectorial sum over all spins in a sample, the signal from an ensemble of spins facing different directions adds up destructively. Indeed, a spin at position $\mathbf{r}$ will, under the influence of a general time-dependent gradient $G(t)$ acting between times t_1 and t_2, acquire a phase $\Delta\phi_G$ given by:

$$\Delta\phi_G(\mathbf{r}, t_1, t_2) = \int_{t_1}^{t_2} \omega(\mathbf{r}, t')dt' = \gamma\int_{t_1}^{t_2} \mathbf{G}(t')\cdot\mathbf{r}dt'. \tag{3}$$

It is often customary to introduce the notation:

$$\mathbf{k}(t) = \gamma\int_{t_1}^{t} \mathbf{G}(t')dt'. \tag{4}$$

by which the acquired phase due to the gradient in the time interval $t' \in [t_1, t_2]$ can be written:

$$\Delta\phi_G(\mathbf{r}, t) = \mathbf{k}(t)\cdot\mathbf{r}. \tag{5}$$

This notation draws out the Fourier conjugacy of the variables $\mathbf{r}$ and $\mathbf{k}$, similar to the conjugacy between time and frequency in usual pulsed NMR experiments. This also suggests that monitoring NMR signals over an array of $\mathbf{k}$-values and Fourier transforming the acquired data will deliver spatially-dependent information. To visualize this, we can describe the magnetization as:

$$\begin{aligned}\mathbf{M}(\mathbf{r}, t) &\propto \rho_0(\mathbf{r})(\cos(\mathbf{k}(t)\cdot\mathbf{r})\hat{\mathbf{x}} + \sin(\mathbf{k}(t)\cdot\mathbf{r})\hat{\mathbf{y}}) \\ &\equiv M_x(\mathbf{r}, t)\hat{\mathbf{x}} + M_y(\mathbf{r}, t)\hat{\mathbf{y}}.\end{aligned} \tag{6}$$

[1] It is important at this point to make a distinction between two sets of coordinates used in NMR. The physical, Cartesian coordinates of real space will be marked (x, y, z), while the rotating frame of spin-space, wherein the magnetization vectors evolve, will be marked by $(\hat{x}, \hat{y}, \hat{z})$. These two systems can be considered independent of each other [24].

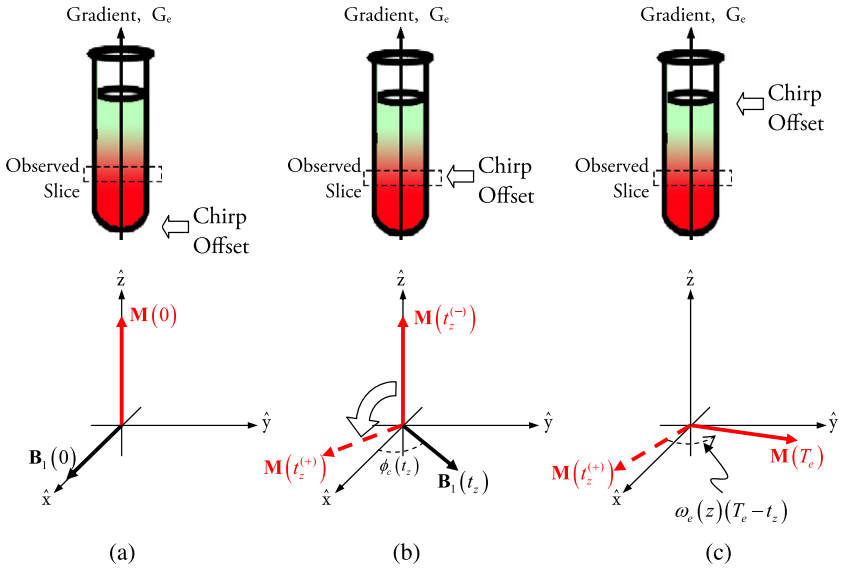

Fig. 3. Intuitive illustration of the effect of a chirped $\frac{\pi}{2}$ excitation pulse of duration T_e on a spin at a point z along the sample, having an off-resonance frequency $\omega_e(z) = \Omega_1 + \gamma G_e z$. (a) Initially, the phase of the RF pulse is 0, and the spin is in thermal equilibrium along the $\hat{z}$-axis. (b) At time t_z, the offset $\omega_c(t_z)$ of the chirp matches $\omega_e(z)$ and instantaneously tips the magnetization onto the $\hat{x}\hat{y}$-plane at a right-angle to the RF pulse. Here $\mathbf{M}(t_z^{(-)})$ represents the magnetization an instant before the chirp's action, and $\mathbf{M}(t_z^{(+)})$ an infinitesimal time step after. (c) For the remaining duration of the pulse, $T_e - t_z$, the spin precesses freely, acquiring an additional phase $\omega_e(z)(T_e - t_z)$.

It is convenient at this point to switch to a complex notation, where $M_+ \equiv M_x + \imath M_y \propto \rho_0(\mathbf{r})e^{\imath\mathbf{k}(t)\cdot\mathbf{r}}$. The signal picked up by the receiver coil is proportional to the vectorial sum of the $\hat{x}\hat{y}$-components of the magnetization: $s \propto \int M_+(\mathbf{r})d\mathbf{r}$, where the integration is carried out over the entire sample. (The proportionality constant depends on the geometry of the coil and the electronics – for a non-ideal receiver, one would have to introduce some weighting function $w(\mathbf{r})$ to account for the spatially-dependent sensitivity, $s \propto \int_{\text{sample}} w(\mathbf{r})M_+(\mathbf{r})d\mathbf{r}$. In what follows an ideal receiver will be assumed, for which $w(\mathbf{r}) = 1$.) Acquiring in the presence of a gradient, one thus measures:

$$s(t) \propto \int M_+(\mathbf{r},t)d\mathbf{r} \propto \int \rho_0(\mathbf{r})e^{\imath\mathbf{k}\cdot\mathbf{r}}d\mathbf{r}. \tag{7}$$

For a constant density $\rho_0(\mathbf{r})$, the signal $s(t) \propto \frac{\sin(\gamma GtL)}{\gamma GtL}$ and the observable will decay rapidly for large γGt values. Designating $\mathbf{r}$ and $\mathbf{k}(t)$ as conjugate variables, it is clear that Eq. (7) represents a 3-D Fourier transformation of the spin density $\rho_0(\mathbf{r})$: the acquired signal is proportional to the Fourier transform of $\rho_0(\mathbf{r})$. By changing $\mathbf{G}_a(t)$, and hence the conjugate variable $\mathbf{k}(t)$, one can sample this over the so-called $\mathbf{k}$-space over enough values to perform an inverse Fourier transform and reconstruct $\rho_0(\mathbf{r})$. This basic observation lies at the heart of MRI, and will be further elaborated later on.

2.2. Chirped excitation pulses

Fig. 2 shows the action of a constant, hard RF pulse, followed by a gradient. Consider next the action of an RF pulse acting simultaneously with a gradient, which, for simplicity, we shall assume is applied along the spatial z-axis. With the aid of a linearly swept (chirped) RF pulse, this field gradient allows one to excite the spins from a point z_a to a point z_b sequentially in time. This is an important ingredient in the spatial encoding of the spin interactions, whose properties we consider next.

Unlike the usual NMR hard-pulse, which (when viewed in its on-resonance rotating frame) has a fixed phase and a bandwidth defined by its duration, a chirped RF pulse has a frequency, $\omega_c(t)$, which varies as a function of time. It will, in general, be described by:

$$\mathbf{B}(t) = B_1(t)[\cos(\phi_c(t))\hat{\mathbf{x}} + \sin(\phi_c(t))\hat{\mathbf{y}}], \tag{8}$$

where $B_1(t)$ is a slowly varying envelope, and

$$\phi_c(t) = \int_0^t \omega_c(t')dt', \tag{9}$$

is the phase accumulated by the RF. Note that the trivial case in which $B_1(t)$ and $\omega_c(t)$ are constant corresponds to a simple rectangular pulse with an off-resonance offset ω_c. If $\omega_c(t)$ varies with time as

$$\omega_c(t) = O_i + Rt, \tag{10}$$

the RF is said to be linearly chirped. O_i is the initial sweep frequency (in, e.g., rad/s) and R is the *rate* of the chirp, having dimensions of angular frequency per unit time (e.g., rad/s^2). One can define $R = \Delta O/T_e$, where T_e is the chirped pulse's duration and ΔO is the chirp's *bandwidth*: $\Delta O = O_f - O_i$, where $O_f \equiv \omega_c(T_e), O_i \equiv \omega_c(0)$. ΔO represents the range of frequencies affected by the pulse throughout its duration. Fig. 4 shows the basic parameters and features of a typical linearly chirped pulse: amplitude, frequency and phase characteristics.

The spin evolution imparted by the chirped excitation RF pulse can be described as illustrated in Fig. 3: at each instant in time, the chirped pulse has a well defined instantaneous frequency, $\omega_c(t) = d\phi_c/dt$. The pulse will affect spins having a precession frequency close to this resonant frequency, and have a weaker effect on spins with resonant frequencies far away from it; the extent and reach of this influence will depend on the strength of the applied B_1 field and on the rate, R. To a first approximation, we shall assume that this excitation width can be taken to be negligibly small. Hence, at a certain time, t', the chirp pulse will only affect those spins with an off-resonance frequency equal to $\omega_c(t')$, and tip them about the RF field onto the $\hat{x}\hat{y}$ plane.[2] Thus, a linearly swept chirp pulse, having a linear $\omega_c(t)$, will sequentially affect all frequencies from O_i to O_f. In addition, the phase $\phi_c(t)$ of the RF pulse at time t' will serve to determine about which axis the spins having an off-resonance frequency $\omega_c(t')$ will be tipped.

[2] The tilt angle will be proportional to the power of the chirp at that particular instance in time, that is to $B_1(t')$. The actual tilt angle can be calibrated by changing this B_1 value – see Section 2.2.1.

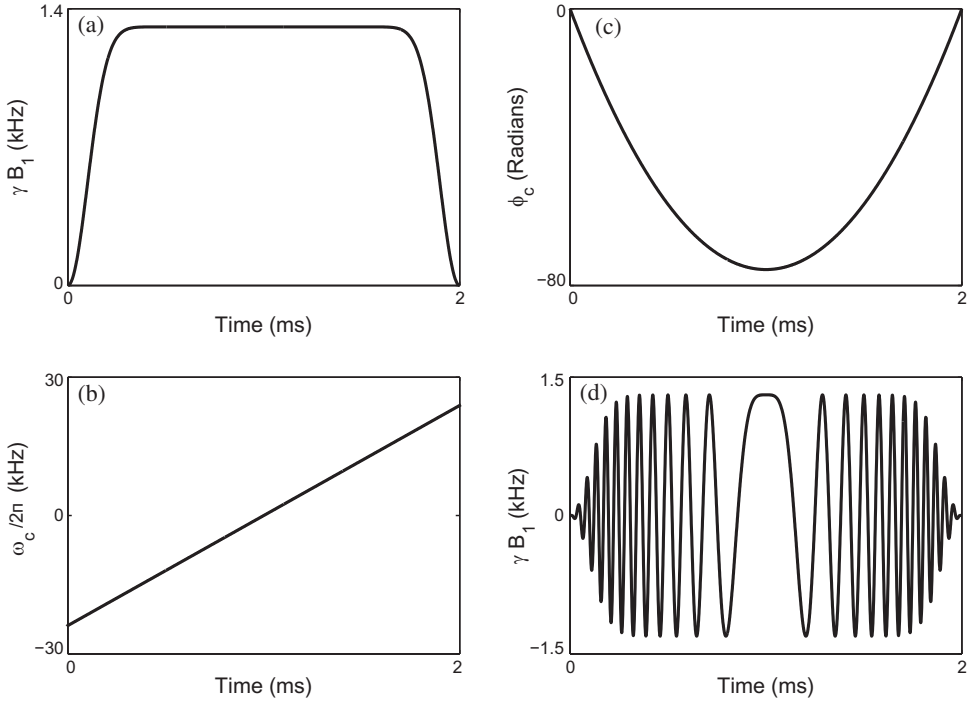

Fig. 4. Features of a linearly swept chirp RF pulse (see Eq. (8)), covering a bandwidth of $\Delta O = 48$ kHz over a time $T_e = 2$ ms, and calibrated for a $\frac{\pi}{2}$ excitation. (a) The chirp's amplitude envelope, $\gamma B_1(t) \propto 1 - \cos^{40}(\pi t/T_e)$. This envelope, termed *wurst* [78], helps smooth out the chirp's frequency response. (b) The chirp's instantaneous frequency, $\omega_c = d\phi_c/dt$, in kHz rad: a linear function of the form shown in Eq. (10). (c) The chirp's phase, $\phi_c(t)$. Note its quadratic time-dependence, chosen to ensure the chirp's sweep's linearity. (d) The RF field's x-component. Notice the oscillations slowing down near $t \approx 1$ ms, as ω_c crosses 0.

Fig. 3 highlights this feature, assuming for concreteness that the spread in the spins' intrinsic precession frequencies arises due to the presence of a field gradient acting along the z-axis. The gradient creates a one-to-one correspondence between position and frequency via $\omega_e(\mathbf{r}) = \Omega_1 + \gamma \mathbf{G}\cdot\mathbf{r} = \Omega_1 + \gamma G_e z$. A linear chirped excitation having initial and final frequencies O_i, O_f, will then sequentially excite all spins from $z_a = \omega_c(0)/\gamma G_e$ to $z_b = \omega_c T_e/\gamma G_e$. Fig. 3 follows the magnetization corresponding to a particular slice z throughout the chirp's duration, T_e. This spin packet will remain unaffected until a time t_z, at which the instantaneous frequency of the chirp matches its own. At that time it gets instantaneously flipped, and will continue to precess freely until the end of the RF pulse.

2.2.1. The spins' response to chirped excitation pulses

The above reasoning can be made formal and used to compute the position-dependent phase of the spins in the $\hat{x}\hat{y}$-plane following a chirped excitation pulse of duration T_e. Let

$$\omega_e(z) = \Omega_1 + \gamma G_e z, \tag{11}$$

be the position-dependent off-resonance frequency of the spins (in rad kHz), where Ω_1 is the chemical shift of the spins in question. Let t_z be the time at which the frequency of the chirp matches the off-resonance frequency of the spins at z, at which $\omega_e(z) = \omega_c(t_z)$. Assuming a linear chirp (Eq. (10)) and solving for t_z, one obtains:

$$t_z = \frac{\gamma G_e z + \Omega_1 - O_i}{R}. \tag{12}$$

The total phase $\Phi_e(z)$ acquired by the spins at z will be the sum of two contributions: that of the RF pulse imparting the nutation,[3] and that accrued after being tipped onto the $\hat{x}\hat{y}$-plane. Indeed, spins are excited onto the $\hat{x}\hat{y}$ plane at a time t_z by an RF pulse having a particular orientation in the $\hat{x}\hat{y}$-plane at that time, determined by its phase, $\phi_c(t_z)$, at time t_z. That is, they are rotated from their thermal equilibrium position along the $\hat{z}$-axis onto the $\hat{x}\hat{y}$-plane about an axis in that plane, subtending an angle $\phi_c(t_z)$ with the $\hat{x}$-axis. Furthermore, having been tilted onto the $\hat{x}\hat{y}$-plane, spins will precess with a frequency $\omega_e(z)$ for the remainder of the pulse. Thus:

$$\Phi_e(z) = \left(\phi_c(t_z) - \frac{\pi}{2}\right) + \omega_e(z)(T_e - t_z). \tag{13}$$

Substituting Eqs. (11), (10) into Eq. (13), and using $\phi_c(t) = \int_0^t \omega_c(t')dt'$, one ends up with a quadratic dependence of the spins' phase on position:

$$\Phi_e(z) = -\frac{(\gamma G_e)^2}{2R} z^2 + \gamma G_e \left(T_e + \frac{O_i - \Omega_1}{R}\right) z + \left(-\frac{(O_i - \Omega_1)^2}{R} + \Omega_1 T_e - \frac{\pi}{2}\right). \tag{14}$$

A common weakness of both these intuitive and theoretical descriptions appears to lie in the instantaneous effects attributed to the sweeping of the RF's offset. Nevertheless, numerical simulations (and experiments) vouch for the reliability of this important approximation. Fig. 5 illustrates this with simulations of the time evolution of the magnetization components of spins at different positions along a 20 mm sample in response to a swept pulse, applied in the presence of a gradient. Note how the spins are negligibly affected by the chirped pulse, except during a very short time instant during which they get tipped almost instantaneously. Numerical simulations also vouch for the quantitative accuracy of the final result in Eq. (14), as illustrated by the plots in Fig. 6.

In discussing chirped pulses so far, it has been assumed that their power has been calibrated so as to effect the appropriate tilt angle; e.g., that the $\frac{\pi}{2}$ chirped excitation pulses have tipped the spins by precisely 90° onto the $\hat{x}\hat{y}$-plane. It is possible to show

[3] In general, spins excited onto the $\hat{x}\hat{y}$-plane by a hard-pulse with a phase ϕ (measured with respect to the $\hat{x}$-axis) will get tilted perpendicularly to it and end up making an angle $\phi - \frac{\pi}{2}$ with the $\hat{x}$-axis. For example, a hard-pulse about the $\hat{x}$ axis ($\phi = 0°$) will tilt spins onto the $-\hat{y}$ axis ($\phi = -90°$). In this treatment, when the frequency of the spins at z matches that of the chirped pulse at the time t_z, its action is approximated by a hard-pulse having a phase $\phi_c(t_z)$.

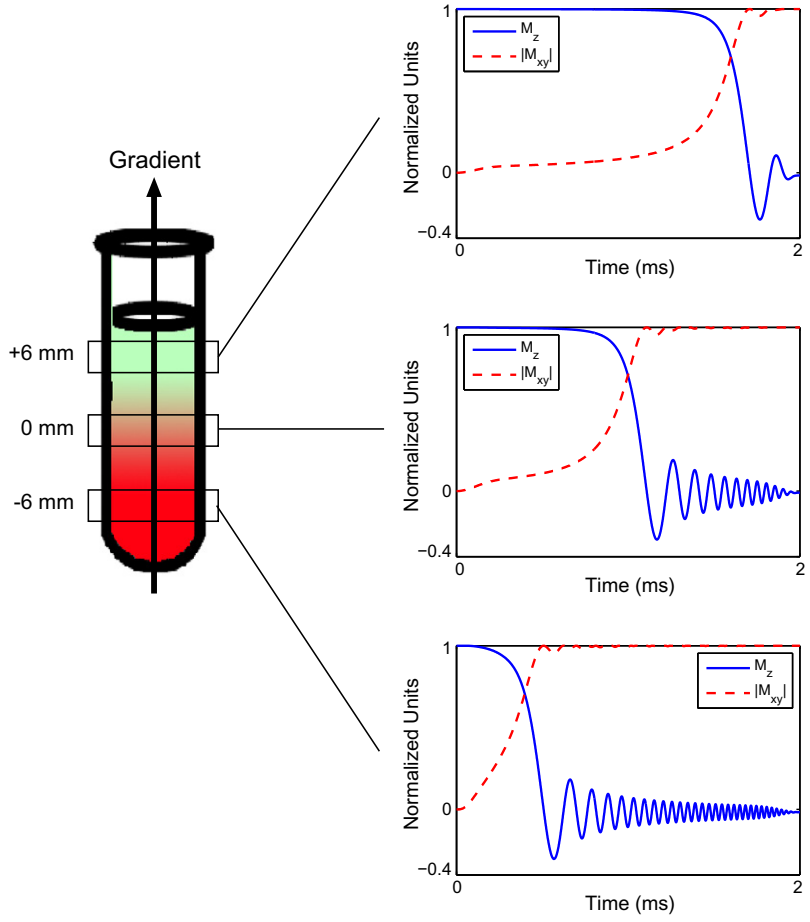

Fig. 5. Calculated evolution for a magnetization's longitudinal and transverse components as a function of time, under the effect of the chirped $\frac{\pi}{2}$ excitation pulse shown in Fig. 4, in the presence of a field gradient $G_e = 5.6$ Gauss/cm. The figure shows the evolution of spins at three different positions along the sample. Top: $z = 6$ mm; Middle: $z = 0$ mm; Bottom: $z = -6$ mm.

[10] that the tilt angle of a chirped excitation at low powers and until reaching adiabatic-passage conditions is proportional to $\sqrt{R}$, where R is the sweeping rate of the chirp, as defined by Eq. (10). The precise constant needed to ensure a $\frac{\pi}{2}$ angle can be found, for instance, via numerical simulations. Hence,

$$\gamma B_1 = 2\pi \times 0.27 \times \sqrt{R}, \tag{15}$$

constitutes a proper power level calibration for a constant $n/2$-tilting envelope. When using a time-dependent (as opposed to a constant) envelope, though, it must be remembered that the tilt angle is proportional to the area under the pulse, $\int_0^{T_p} B_1(t')dt'$. To a first approximation Eq. (15) must be recalibrated by a factor Λ_{env}, equal to the ratio of the areas under the respective pulses – rectangular and time-dependent:

$$\Lambda_{\text{env}} = \frac{\gamma B_{1,\max} T_p}{\gamma \int_0^{T_p} B_1(t)dt'}, \tag{16}$$

where $B_{1,\max}$ is the maximal amplitude of $B_1(t)$. For a wurst-modulation,

$$\gamma B_1(t) \propto 1 - \left|\sin^{40}\left(\frac{\pi\left(t - \frac{T_p}{2}\right)}{T_p}\right)\right|, \tag{17}$$

$\Lambda_{\text{env}} = 1.1433$. Hence, if a $\frac{\pi}{2}$-chirp envelope is chosen to have such shape, its maximal amplitude, as expressed in Eq. (15), should be multiplied by 1.1433.

2.3. Chirped storage pulses

Chirped pulses can be used not only to excite spins aligned along the $\hat{z}$-axis onto the $\hat{x}\hat{y}$-plane with a spatially-dependent quadratic phase; they can also be used to store the magnetization along the $\hat{z}$-axis with a linear, amplitude-modulated phase. Following the same line of reasoning as before, let $\mathbf{B}_1(t)$ be a linear chirped storage pulse of duration T_s, applied in the presence of a field gradient G_s, with an instantaneous frequency[4] $\omega_c(t) = O_i + Rt$. The spatially dependent off-resonance frequency of the spins is

$$\omega_s(z) = \Omega_1 + \gamma G_s z. \tag{18}$$

Denoting by t_z the time at which the RF's instantaneous frequency matches the off-resonance frequency of the spins at $z, \omega_c(t_z) = \omega_s(z)$, one obtains:

$$t_z = \frac{\gamma G_s z + \Omega_1 - O_i}{R}. \tag{19}$$

As with the excitation chirp, it will be assumed that the chirp's effect on the spins is instantaneous, such that at time t_z only the spins at position z will be affected by the RF, and that the chirp's power has been properly calibrated such that those spins will get rotated precisely by 90° back to the z-axis. This time, however, the RF pulse will only flip that component of the spins in the $\hat{x}\hat{y}$-plane which is

[4] The subscript s indicates storage (note that G_s, T_s, O_i, R may be different from the parameters used in discussing the chirped excitation in Section 2.2.1).

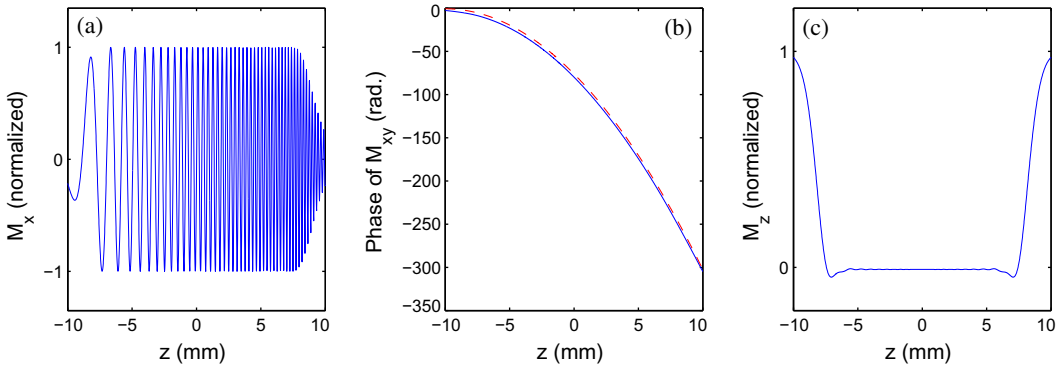

Fig. 6. Calculated response of spins in a 20 mm sample as a function of position to the chirp RF shown in Fig. 4, applied in the presence of a gradient $G_e = 5.6$ Gauss/cm. (a) The x-component of the magnetization following the pulse. (b) The phase of the magnetization (solid), showing excellent agreement with the theory, Eq. (14) (dashed). (c) The z-component of the magnetization.

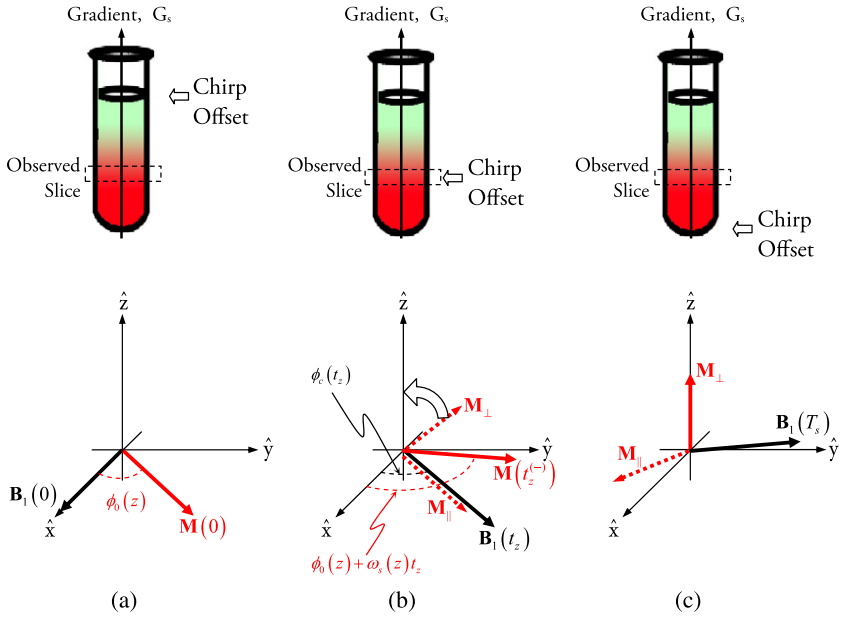

Fig. 7. The effect of a chirped storage pulse on a spin in the Bloch sphere's $\hat{x}\hat{y}$-plane at a particular position z along the sample. (a) At time $t = 0$ the spin has some initial phase, $\phi_0(z)$, while the RF pulse has no phase, $\phi_c(0) = 0$. (b) At time t_z, the spin is acted upon by the RF pulse. The figure shows how $\mathbf{M}(t_z^{(-)})$, the spin's state just prior to the chirp's action, can be decomposed into a part $\mathbf{M}_{||}$ parallel to $\mathbf{B}_1$ at time t_z, and a part $\mathbf{M}_{\perp}$ perpendicular to it, both in the Bloch sphere's $\hat{x}\hat{y}$-plane as well. (c) The chirp instantaneously tilts $\mathbf{M}_{\perp}$ onto the z-axis, while leaving $\mathbf{M}_{||}$ in the $\hat{x}\hat{y}$-plane. The stored component of the magnetization remains stationary for the rest of the pulse, while $\mathbf{M}_{||}$ continues to freely precess.

perpendicular to it. The magnetization components of the spins parallel to the RF pulse will not get stored; they remain in the $\hat{x}\hat{y}$-plane and may be disregarded.

Let $M_+(z) = M_0 e^{\imath\phi_0(z)}$ denote the magnetization in the $\hat{x}\hat{y}$-plane as a function of position at the beginning of one such storage pulse, assumed to be of uniform magnitude (i.e., $\rho(\mathbf{r}) = 1$) but having a spatially-dependent phase $\phi_0(z)$ (as would be the case following a chirped excitation). Consider a spin at a particular position z. That spin precesses in the $\hat{x}\hat{y}$-plane up until time t_z, whence it accumulates a phase $\omega_s(z)t_z$; its magnetization vector at this point is $M_+(z) = M_0 e^{\imath(\phi_0(z)+\omega_s(z)t_z)}$. At time t_z, it is acted upon by the storage RF pulse, $B_1(t)e^{\imath\phi_c(t_z)}$ (Fig. 7). Decomposing the magnetization vector of the spins into a component parallel to the field, $M_{||}$, and a component perpendicular to it, $M_{\perp}$, leads to[5]:

$$M_+(z) = M_{\perp} + M_{||}, \tag{20}$$

$$M_{\perp} = M_0 \sin(\phi_0(z) + \omega_s(z)t_z - \phi_c(t_z))e^{\imath\left(\phi_c(t_z)+\frac{\pi}{2}\right)}, \tag{21}$$

$$M_{||} = M_0 \cos(\phi_0(z) + \omega_s(z)t_z - \phi_c(t_z))e^{\imath\phi_c(t_z)}. \tag{22}$$

Assuming the pulse power has once again been properly calibrated for a 90° tip angle, the perpendicular component gets stored along the $\hat{z}$-axis and the parallel component remains in the $\hat{x}\hat{y}$-plane. Once stored, a spin feels no additional fields, the RF being off-resonance for the remainder of the pulse. Hence its transverse component continues to precess with a frequency $\omega_s(z)$ and dephases further, while its stored longitudinal component remains constant in time. Neglecting relaxation, this last component is equal to:

$$M_z(z) = M_0 \sin(\phi_0(z) + \omega_s(z)t_z - \phi_c(t_z)). \tag{23}$$

This formula describes the z-component of the magnetization as a function of position at the end of the pulse.

The chirp's effect is thus 3-fold: it adds a phase $\omega_s(z)t_z - \phi_c(t_z)$ to the spins; it stores the magnetization along the z-axis; and it *amplitude modulates* it by the new phase. The overall phase accrued

[5] Given an RF field $B = B_1 e^{\imath\phi_{RF}}$ and a magnetization vector $M_+ = M_0 e^{\imath\phi_{mag}}$ in the $\hat{x}\hat{y}$-plane, M can always be decomposed into a part perpendicular to B and a part parallel to it. The perpendicular part – which will get acted upon by the field – will have a phase equal to $\phi_{RF} + \frac{\pi}{2}$, i.e., it will be at a right-angle to the field; hence the $\phi_c(t_z) + \frac{\pi}{2}$ term, appearing in Eq. (21). The parallel part, on the other hand, will have a phase identical to that of the RF field.

can be calculated by substituting ω_s, t_z, and $\phi_c(t)$ (Eqs. (19), (18) and (9)) explicitly:

$$\omega_s(z)t_z - \phi_c(t_z) = \left(\frac{(\gamma G_s)^2}{2R}\right)z^2 + \left(-\frac{\gamma G_s(O_i-\Omega_1)}{R}\right)z + \left(\frac{(O_i-\Omega_1)^2}{2R}\right). \tag{24}$$

The calibration of chirped storage pulses is identical to that of excitation pulses, as discussed in Section 2.2.1.

2.4. Chirped π-pulses

Chirped pulses can be used not only to excite and store spins, but also to invert or flip them in the $\hat{x}\hat{y}$-plane. Such RF sweeps belong to the family of "adiabatic" pulses, known to preserve the relative angle between the spin magnetization and the effective magnetic field in a suitable rotating frame. In particular, *chirped π-pulses* are functionally similar to excitation and storage chirps (Eq. (8) and Fig. 4), but possess higher power levels so as to produce a 180° flip angle.

The mechanism by which such a π flip is produced warrants further discussion. Much like the $\frac{\pi}{2}$ chirp, a swept π chirp flips spins "instantaneously" when its resonant frequency matches the precession frequency of the spins. Unlike the $\frac{\pi}{2}$ chirp, a π chirp conserves the relative angle θ between the spins' magnetization and the effective **B**-field as it changes [25,26,23]. This is best understood in a *frequency-modulated* frame rotating about the $\hat{z}$-axis at the same rate as the RF field. In such a frame, the total magnetic field – which, in the rotating frame is of the form $\gamma\mathbf{B}_{\rm rot}(t) = (\gamma B_1(t)\cos(\phi_c(t)), \gamma B_1(t)\sin(\phi_c(t)), \Omega_1)$ – becomes[6]

$$\gamma\mathbf{B}_{\rm FM}(t) = (\gamma B_1(t), 0, \Omega_1 + O(t)). \tag{25}$$

Note the additional $O(t)$ "fictitious force" term added to the z-component, as a result of the non-uniform rotation of this frame of reference. In this frequency-modulated (FM) frame, the RF field remains in the $\hat{x}$–$\hat{z}$ plane, and its constant $\hat{x}$-component implies that the field vector $\mathbf{B}_{FM}(t)$ sweeps out a triangle. Assuming for simplicity that the chemical shift is significantly smaller than the chirp bandwidth, i.e., $\Omega_1 \ll \Delta O$, implies that, in this frame, $\mathbf{B}_{FM}$ starts out and ends up being almost parallel to the $\hat{z}$-axis, as illustrated in Fig. 8.

The adiabatic theorem [27] states that, when the RF field's direction varies more slowly than the precession frequency of the spins (imposed by $\mathbf{B}_{FM}$), the angle between the field and the spins is conserved.[7] A direct consequence of the adiabatic theorem is that the angle θ between the field and the spins is time-invariant. Of particular relevance for the present discussion is a state where spin packets are initially distributed in the $\hat{x}\hat{y}$-plane, represented by the shaded disc in Fig. 8. This plane rotates *adiabatically* along with the RF field in such a way as to conserve θ. Fig. 9 plots the effect calculated for such a swept π-pulse, applied in the presence of a linear z-gradient, on an ensemble of spins assumed to be initially along the $\hat{z}$ or the $\hat{x}$ axes of the Bloch sphere. In the former case, the typical following of M_z and B_{FM} is easily discernable.

From a standpoint of spatial encoding, it is relevant to compute not only the rotation but also the phase imparted by these chirped π-pulses. This analysis of π-chirps is similar to that of the $\frac{\pi}{2}$-chirps discussed earlier. Assuming a pulse having duration $T^{(\pi)}$ is applied in the presence of a gradient $G^{(\pi)}$, a spin with chemical shift Ω_1 and position z will have its off-resonance frequency given by $\omega^{(\pi)}(z) = \Omega_1 + \gamma G^{(\pi)}z$. An RF endowed with a linear frequency sweep given by Eq. (10) will – once again, to a good approximation – flip the spin only when ω_c matches $\omega^{(\pi)}$ for that z. This will occur at a time t_z such that $\omega_c(t_z) = \omega^{(\pi)}(z)$. Solving explicitly for t_z, Eq. (12) is recovered, with G_e swapped for $G^{(\pi)}$. A spin with an initial phase ϕ_0 positioned at z will, therefore, precess freely until time t_z and acquire a phase $\omega^{(\pi)}t_z$. At this instant, the chirp will effectively flip this spin with respect to an axis colinear with the RF pulse at time t_z. Assuming, as before, that $\phi_c(t) \equiv \int_0^t \omega_c(t')dt'$ will be the phase of this RF at time t into the pulse, then $\phi_c(t_z)$ is also the angle with the $\hat{x}$-axis in the $\hat{x}\hat{y}$-plane, with respect to which the spin at z is π-flipped. As a result of this effect the phase of the spin will become $-\phi_0 + 2\phi_c(t_z) - \omega^{(\pi)}(z)t_z$, where ϕ_0 is the spin phase before applying the chirp. The magnetization vector will then continue precessing with a frequency $\omega^{(\pi)}(z)$ for the remaining duration of the pulse, $T^{(\pi)} - t_z$, and will hence acquire an additional phase $\omega^{(\pi)}(z)(T^{(\pi)} - t_z)$. The total phase of the magnetization vector at the end of the pulse is therefore

$$\phi^{(\pi)}(z) = -\phi_0(z) + 2\phi_c(t_z) - 2\omega^{(\pi)}(z)t_z + \omega^{(\pi)}(z)T^{(\pi)}. \tag{26}$$

This sequence of events is described pictorially in Fig. 10, with a time plots of the $\hat{x}\hat{y}$ magnetization components for spins at different positions along the sample shown in Fig. 11. By substituting the explicit expressions for $\omega^{(\pi)}$ and t_z into Eq. (26), this overall $\phi^{(\pi)}(z)$ phase can be explicitly calculated:

$$\begin{aligned}\phi^{(\pi)}(z) = -\phi_0(z) &- \left(\frac{\left(\gamma G^{(\pi)}\right)^2}{R}\right)z^2 \\ &+ \left(\frac{2\gamma G^{(\pi)}(O_i-\Omega_1)}{R} + \gamma G^{(\pi)}T^{(\pi)}\right)z \\ &+ \left(T^{(\pi)}\Omega_1 - \frac{(O_i-\Omega_1)^2}{R}\right).\end{aligned} \tag{27}$$

An important consideration in all this analysis is whether and when the RF chirp fulfills the adiabaticity condition. This can be exposed explicitly using Eq. (25) to compute the angle α between the field in the frequency-modulated frame, $\mathbf{B}_{FM}$, and the $\hat{x}$-axis. Using straightforward trigonometry :

$$\alpha(t) = \arctan\left[\frac{\Omega_1 - O(t)}{\gamma B_1}\right]. \tag{28}$$

The magnitude of the derivative of this angle then measures the rate of change of the field direction, and is given by:

$$\left|\frac{d\alpha(t)}{dt}\right| = \frac{\gamma B_1 R}{(O(t)+\Omega_1)^2 + (\gamma B_1)^2}. \tag{29}$$

By differentiating and equating the result to zero, $d\alpha/dt$ is found to reach its maximal value at

$$t_{\rm extremum} = \frac{T^{(\pi)}}{2} - \frac{\Omega_1}{R} \approx \frac{T^{(\pi)}}{2}; \tag{30}$$

this value is[8] $|d\alpha/dt|_{max} = R/\gamma B_1$. On the other hand, the spin precession frequency about $\mathbf{B}_{\rm FM}(t)$ is

$$\omega_{\rm eff}(t) = |\gamma\mathbf{B}_{\rm FM}(t)|, \tag{31}$$

and is slowest when $\mathbf{B}_{\rm FM}$ is smallest, that is, at $t = t_{\rm extremum}$, when its $\hat{z}$-component is 0 and $|\gamma\mathbf{B}_{\rm FM}| = \gamma B_1 \equiv \omega_{\rm eff,min}$ (see Fig. 12). The RF field $\mathbf{B}_{FM}$ will remain "adiabatic" as long as its rate of change is

[6] The chirp envelope, $B_1(t)$, will be assumed constant. Slightly smoothed B_1 amplitude envelopes (e.g., Eq. (17)) will modulate the response, but not alter the conclusions derived herein.

[7] This fact is used in the design of adiabatic inversion pulses, in which the RF field and spins start along parallel to the $\hat{z}$ axis, and – by slowly sweeping the field until it points along $-\hat{z}$ – one can ensure that the spin follow it, ending up pointing along the $-\hat{z}$ direction as well.

[8] This is geometrically sound, as the maximum occurs roughly halfway through the pulse, when the field's z-component is 0 and its change is most pronounced (see Fig. 8b).

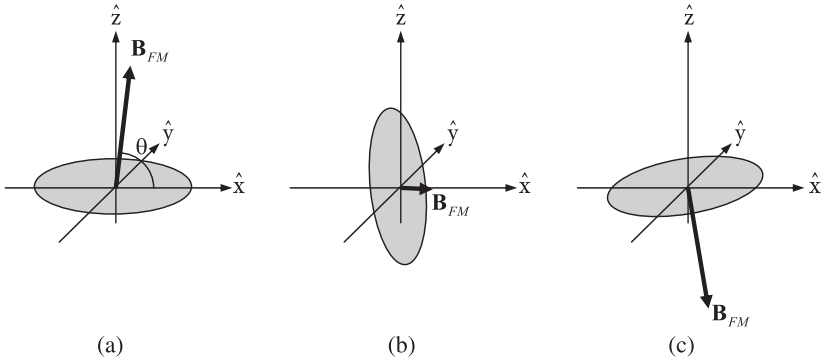

Fig. 8. Adiabatic RF π chirp, viewed in a frequency-modulated (FM) frame at: (a) the beginning of the chirp; (b) midway through the chirp; (c) at its conclusion. The shaded disc represents the spins in the $\hat{x}\hat{y}$-plane at the beginning of the pulse. Due to the pulse's adiabaticity, the angle between the disc and the field is kept constant throughout the pulse, effectively flipping the spins in the $\hat{x}\hat{y}$-plane.

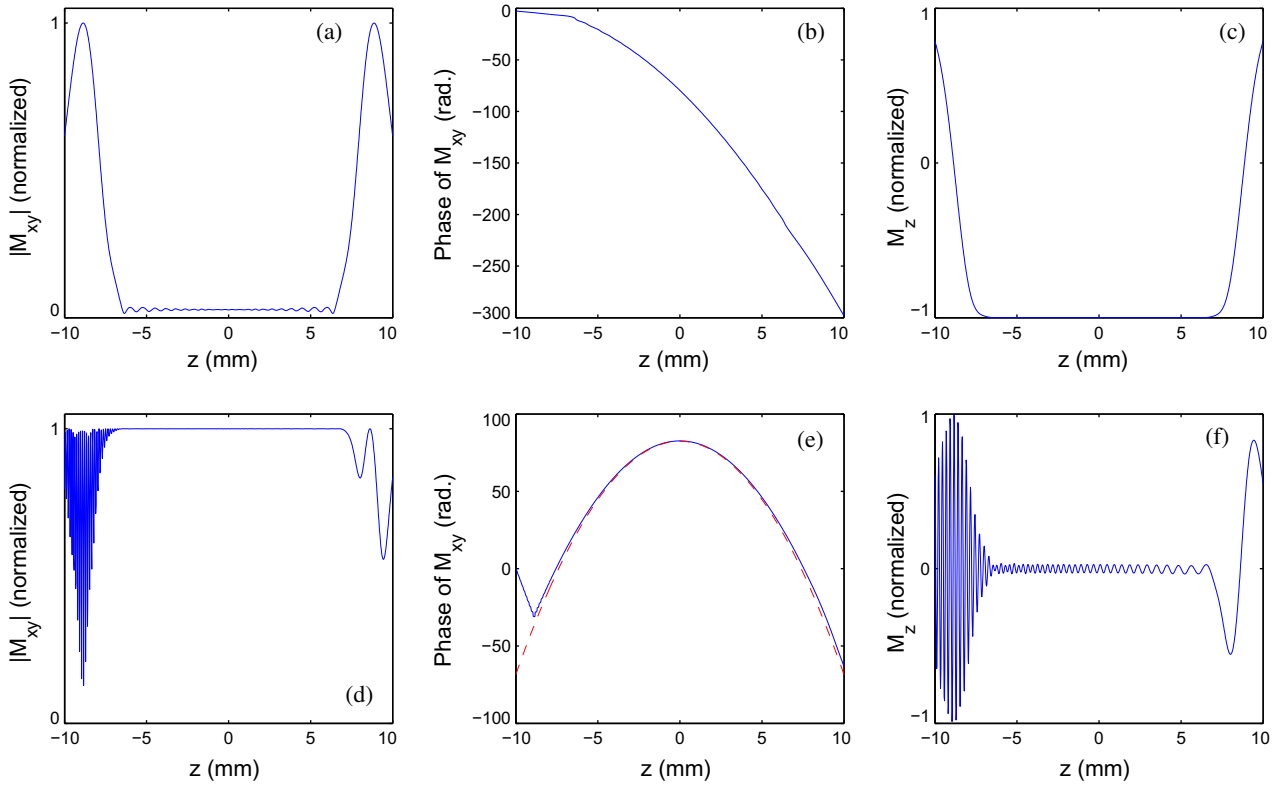

Fig. 9. Calculated response of spins in a 20 mm sample, as a function of position, to a π-chirp, applied in the presence of a gradient $G = 4.7$ Gauss/cm. The spins were assumed to start out either along the $\hat{z}$-axis (top panels, a–c) with an initial magnetization vector $\mathbf{M} = (0, 0, 1)$, or the $\hat{x}$-axis (bottom panels, d–f), with an initial magnetization vector $\mathbf{M} = (1, 0, 0)$. (a and d) The absolute value of the magnetization's projection on the $\hat{x}\hat{y}$-plane. (b and e) The phase induced by the chirp in the transverse plane. Note in (e) the agreement with between the simulated result (solid, blue) and the theoretical quadratic prediction, as given by Eq. (27) (red, dashed). (c and f) The z-component of the magnetization. (For interpretation of the references to color in this figure legend, the reader is referred to the web version of this article.)

slower than the spins' precession about it; this is assured to hold throughout the chirp if $|d\alpha/dt|_{max} \ll \omega_{\text{eff,min}}$, and furnishes the classical condition:

$$\gamma B_1 \gg \sqrt{R}. \tag{32}$$

Further discussions on this can be found in [28].

Due to their adiabatic nature, the calibration of π chirps is somewhat different from that described for their $\frac{\pi}{2}$ counterparts. As shown in Eq. (32), the RF's power in kHz must be larger than $\frac{\sqrt{R}}{2\pi}$. In practice, it is found that setting γB_1 to be at least 2.5 times larger than the power for an equivalent $\frac{\pi}{2}$ chirp (Eq. (15)), achieves an adequate performance. It must also be borne in mind that, in accordance with the analysis presented in Section 2.4, the π chirp approximations break down for chemical shifts comparable to the chirp's bandwidth; this is evident in the tails of the frequency responses plotted in Fig. 9. To ensure a constant response, the chirp's bandwidth must be suitably enlarged.

3. Single-scan ultrafast 2D NMR

3.1. Approaches to spatial encoding

Having introduced the spin evolutions imparted by different chirped RF pulses and the action of gradients, the principles at the heart of single-scan 2D NMR can now be outlined. This is

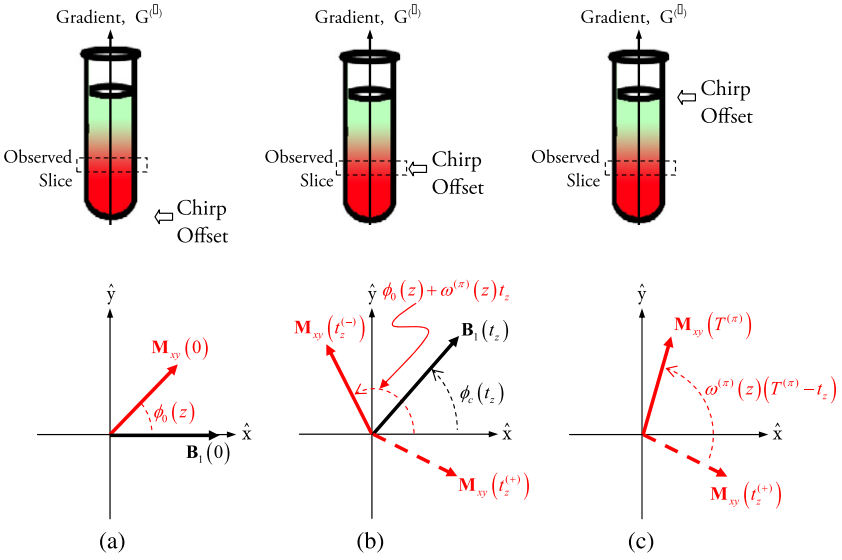

Fig. 10. Time evolution of a spin's magnetization vector, **M**, situated at z during the application of a π-chirp. (a) Initially, at $t = 0$, **M** is assumed already in the $\hat{x}\hat{y}$-plane with some initial phase $\phi_0(z)$. (b) **M** precesses freely and accumulates a phase $\omega^{(\pi)}t_z$ until acted upon by the RF pulse. The figure shows **M** right prior to being flipped, $\mathbf{M}_{xy}(t_z^{(-)})$ (solid) and right after, $\mathbf{M}_{xy}(t_z^{(+)})$ (dashed). Note that the axis around which the spin is flipped is colinear with the RF pulse at time t_z, i.e., an axis in the $\hat{x}\hat{y}$-plane making an angle $\phi_c(t_z)$ with the x-axis. Following the chirp action, the phase of **M** becomes $-\phi_0(z) + 2\phi_c(t_z) - \omega^{(\pi)}(z)t_z$. (c) Following the π-flip, **M** continues precessing freely until the end of the pulse at time $T^{(\pi)}$, accumulating a additional phase $\omega^{(\pi)}(T^{(\pi)} - t_z)$. The total phase of the magnetization vector at the end of the pulse is, therefore, $-\phi_0(z) + 2\phi_c(t_z) - 2\omega^{(\pi)}(z)t_z + \omega^{(\pi)}(z)T^{(\pi)}$.

spatial encoding; i.e., the physical partitioning of a sample into an array of voxels possessing different evolution periods. The objective, we remind again, is the creation of a position-dependent t_1 evolution time of the form $t_1(z) = Cz$. This section focuses on achieving this goal by the three schemes detailed in Fig. 13; additional schemes are discussed in [29–32]. For simplicity, we shall assume in what follows that all chirps have symmetrical bandwidths (namely that the range of frequencies they excite is centered about 0, or, equivalently, that $O_f = -O_i = \frac{\Delta O}{2}$), so that the bandwidth, ΔO, is set equal to $\gamma G_e L$, where L is the sample's physical size[9]

3.1.1. Indirect-domain encoding with phase modulation $\left(\frac{\pi}{2} - \pi\right)$

Consider an ensemble of spins in thermal equilibrium, acted upon by a $\frac{\pi}{2}$ excitation chirp with rate $R^{\left(\frac{\pi}{2}\right)}$, duration $T^{\left(\frac{\pi}{2}\right)}$ and bandwidth $\Delta O^{\left(\frac{\pi}{2}\right)}$, in the presence of a gradient $G^{\left(\frac{\pi}{2}\right)}$. At the end of such a pulse, the spins will have been excited onto the $\hat{x}\hat{y}$-plane, and will have accrued the phase given by Eq. (14). Such a phase contains a part linear in z times the chemical shift, which is desirable; but also an unwanted quadratic phase, proportional to z^2. In order to remove the latter, a π-chirp is applied, with duration $T^{(\pi)}$, rate $R^{(\pi)}$ and initial bandwidth $\Delta O^{(\pi)}$. This second pulse keeps the spins in the $\hat{x}\hat{y}$-plane, but inverts their phase [33] and increments it as detailed in Eq. (27). By choosing $2G^{(\pi)}T^{(\pi)} = G^{\left(\frac{\pi}{2}\right)}T^{\left(\frac{\pi}{2}\right)}$, the phase of the spins following the π chirp will be:

$$\phi^{\frac{\pi}{2}-\pi}(z) = -\left[\frac{\gamma G^{(\pi)}T^{\left(\frac{\pi}{2}\right)}\Delta O^{\left(\frac{\pi}{2}\right)}}{2\Delta O^{(\pi)}}\right]z + \left[\frac{\gamma\left(G^{(\pi)} - G^{\left(\frac{\pi}{2}\right)}\right)T^{\left(\frac{\pi}{2}\right)}}{2\pi\Delta O^{(\pi)}}\right]\Omega_1 z + \left(\frac{\pi}{2} - \frac{T^{\left(\frac{\pi}{2}\right)}\Omega_1}{2} + \frac{T^{\left(\frac{\pi}{2}\right)}\Omega_1^2}{4\pi\Delta O^{\left(\frac{\pi}{2}\right)}} - \frac{T^{(\pi)}\Omega_1^2}{2\pi\Delta O^{(\pi)}}\right). \quad (33)$$

Eq. (33) has precisely the form sought after. It has no quadratic term in z; it has a constant term, which merely phases the peaks and can be dealt with using post-processing; it has a part linear in z and independent of the chemical shift, which – as will be shown in Section 3.2 – moves the spectrum along the indirect domain and can be fixed using a gradient G_p prior to acquisition (cf. Fig. 13a[10]); and it has a term linear in both z and Ω_1, of the form $t_1(z)\Omega_1$ with

$$t_1(z) = -\frac{\gamma\left(G^{\left(\frac{\pi}{2}\right)} - G^{(\pi)}\right)T^{\left(\frac{\pi}{2}\right)}}{\Delta O^{(\pi)}}z = \frac{T^{\left(\frac{\pi}{2}\right)} - 2T^{(\pi)}}{L}z. \quad (34)$$

3.1.2. Indirect-domain encoding with amplitude modulation $\left(\frac{\pi}{2} - \frac{\pi}{2}\right)$

An alternative method to the one presented above uses two successive $\frac{\pi}{2}$-chirps to excite and store the spins [34], as illustrated in Fig. 13b. The purpose of using two chirped pulses in both schemes is the same: the removal of the quadratic phase terms, proportional to z^2. The current approach, however, differs from the previous one by amplitude modulating the magnetization: the initial $\frac{\pi}{2}$ excitation chirp tips the spins onto the $\hat{x}\hat{y}$-plane with a quadratic phase given by Eq. (14). At the end of the second $\frac{\pi}{2}$ storage chirp, part of the magnetization is stored along the z-axis and part remains in the $\hat{x}\hat{y}$-plane and is dephased by a strong gradient G_d, ensuring that transverse components will not contribute to the acquired signal. Assuming both chirps have equal durations $T^{\left(\frac{\pi}{2}\right)}$ and sweep rates $R^{\left(\frac{\pi}{2}\right)}$, and that the gradients used are equal and opposite in sign, $G^{(\text{excite})} = -G^{(\text{store})} \equiv G^{\left(\frac{\pi}{2}\right)}$, then the form of the magnetization stored along the z-axis following the second chirped pulse is (see Eq. (23)):

$$M_z(z) = M_0 \sin\left[-\frac{2\gamma G^{\left(\frac{\pi}{2}\right)}T^{\left(\frac{\pi}{2}\right)}z}{\Delta O^{\left(\frac{\pi}{2}\right)}}\Omega_1 + T^{\left(\frac{\pi}{2}\right)}\Omega_1 - \frac{\pi}{2}\right]. \quad (35)$$

Denoting

$$t_1(z) = -\frac{2\gamma G^{\left(\frac{\pi}{2}\right)}T^{\left(\frac{\pi}{2}\right)}}{\Delta O^{\left(\frac{\pi}{2}\right)}}z = \frac{2T^{\left(\frac{\pi}{2}\right)}z}{L} \equiv \frac{t_1^{max}}{L}z, \quad (36)$$

[9] To avoid the imperfections in the frequency response near the edges of the bandwidth, one can set L slightly larger than the sample's physical size, in effect exciting a wider bandwidth. A factor of 1.2 strikes a good compromise between achieving an even response and avoid irradiating frequencies not present in the sample.

[10] A purge gradient can also be used between the pulses to achieve the same end.

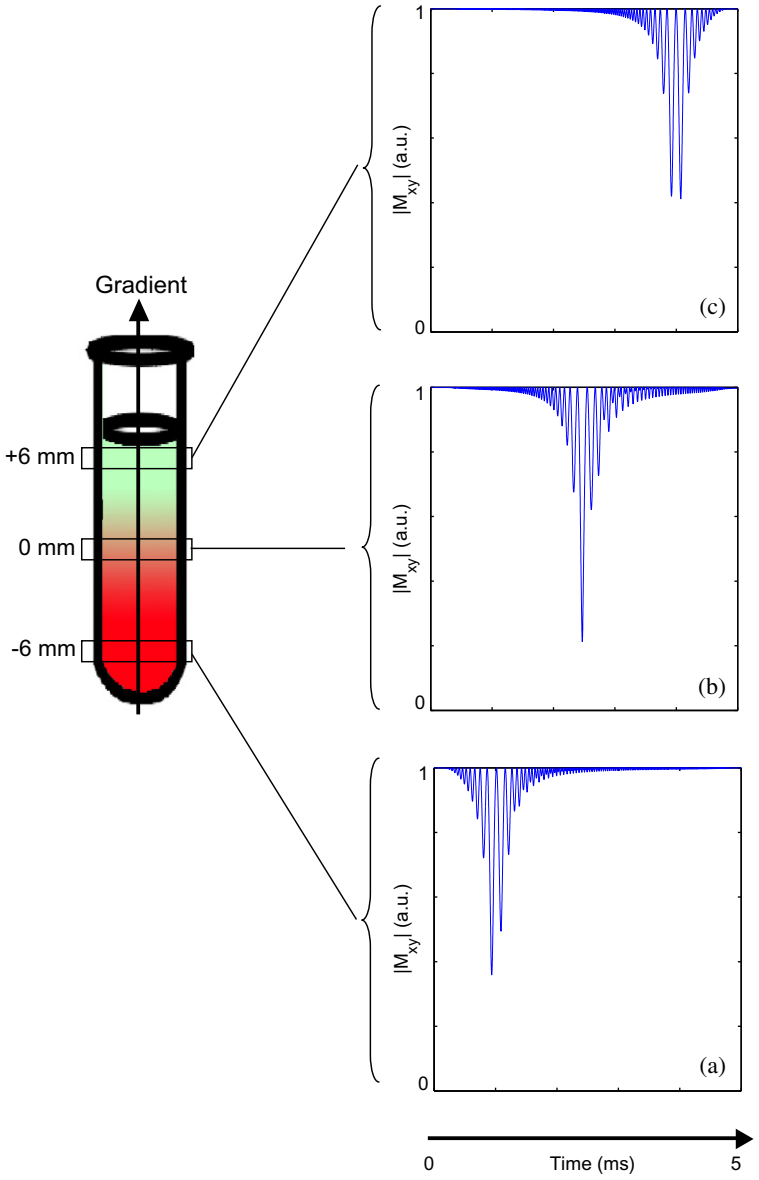

Fig. 11. The simulated evolution of the *xy*-component of the magnetization, for spins at different slices throughout a 20 mm sample, during a chirped π-pulse. The pulse, 5 ms long, was applied in the presence of a gradient $G = 4.7$ Gauss/cm. The spins have all started out along the *x*-axis, with an initial magnetization vector $\mathbf{M} = (1, 0, 0)$. Time evolution is plotted for the slices $z = -6$ mm, $z = 0$ mm and $z = 6$ mm in (a), (b) and (c), respectively.

where $t_1^{max} \equiv 2T^{\left(\frac{\pi}{2}\right)}$ is the total encoding time, one sees that $M_z(z)$ can be written as $M_0 \sin[t_1(z)\Omega_1 + (\text{const. terms})]$.

Following the action of the dephasing gradient G_d, a mixing sequence is applied while the spins are stored, and the ensemble is then tipped back onto the $\hat{x}\hat{y}$-plane using a hard-pulse. The resulting transverse magnetization is then $M_+(z) \propto \sin(t_1(z)\Omega_1 + \psi(z) + \alpha)$, which can be written as the sum of complex exponentials:

$$M_+(z) \propto \frac{1}{2i} e^{\imath\left(t_1(z)\Omega_1 + T^{\left(\frac{\pi}{2}\right)}\Omega_1 - \frac{\pi}{2}\right)} + \frac{1}{2i} e^{-\imath\left(t_1(z)\Omega_1 + T^{\left(\frac{\pi}{2}\right)}\Omega_1 - \frac{\pi}{2}\right)}. \tag{37}$$

The application of a purge gradient G_p for a duration T_p, as shown in Fig. 13b, adds an additional phase $\gamma G_p z T_p$ to both exponentials. As discussed in Section 3.3.2, the effect of such a phase is to shift the indirect-domain spectra. Hence, although both signals in Eq. (37) will contribute to the FID, it is possible to shift one of them outside the spectral width while observing the other. A somewhat similar effect, although with opposite signs for the two terms in Eq. (37), could be introduced by a gradient pulse G_p acting *before* the storage chirped pulse.

3.1.3. Indirect-domain constant-time encoding ($\pi - \pi$)

A third approach to spatial encoding relies on exciting the spins with a hard $\frac{\pi}{2}$ pulse, followed by two chirped π-pulses with identical sweeps but reversed gradients [35] (Fig. 13c). Assuming that the spins have initially been excited onto the *x*-axis, the first π chirp imparts to them a phase $\phi^{(\pi)}(z)$ given by Eq. (27), with $\phi_0(z) = 0$. Following a second π chirp, the phase of the spins at the end of the sequence is:

$$\phi^{(\pi-\pi)}(z) = -\frac{4\gamma G^{(\pi)} T^{(\pi)} \Omega_1 z}{\Delta O}. \tag{38}$$

This once again gives the desired form, with

$$t_1(z) = -\frac{4\gamma G^{(\pi)} T^{(\pi)}}{\Delta O} = \frac{4T^{(\pi)}}{L} z \equiv \frac{2t_1^{max}}{L} z, \tag{39}$$

where $t_1^{max} = 2T^{(\pi)}$ is the total encoding time.

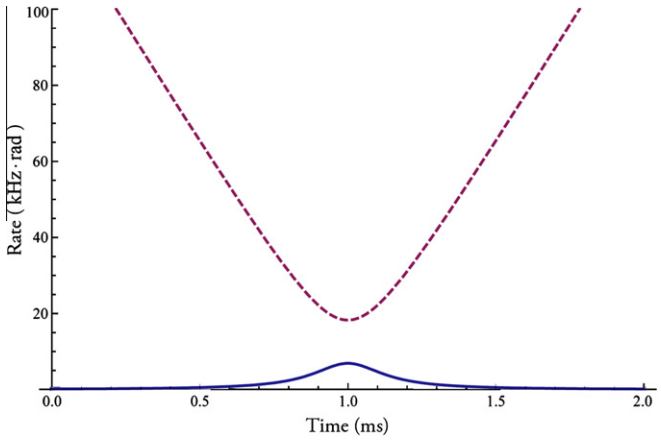

Fig. 12. The precession angular frequency of the spins (dashed, Eq. (31)) and the rate of change of the effective RF field (solid, Eq. (29)) as a function of time for a 2-millisecond π-chirp, as viewed in the frequency-modulated frame. Note that at all times the precession frequency is significantly larger than the rate of change of the field's direction. The two are closest roughly midway throughout the pulse, at a time given by Eq. (30). Additional parameters: a bandwidth of 40 kHz and a power of 2.9 kHz for the chirped pulse, and zero chemical shift for the spins. It can be shown that the effect of non-zero chemical shift is merely to shift the pattern sideways, without affecting the distance between the curves.

3.1.4. Advantages and disadvantages of each method

Although all three methods presented for spatially encoding a sample achieve similar goals – an effective t_1 evolution which increases as a function of position – each has its own advantages and disadvantages.

The frequency response of the amplitude-modulated encoding is better behaved compared to the alternatives, which employ π chirped pulses. $\frac{\pi}{2}$ pulses are also easier to optimize using, say, a Shinnar-Le Roux (SLR) [36] or optimal control [37] algorithms, as excitation/storage pulses operate within the limits of a linear response to a very good degree of accuracy. On the other hand, there are two considerable disadvantages to the excitation-storage approach:

- It is not well suited to mixing sequences which require that spins remain in the $\hat{x}\hat{y}$-plane, such as COSY, or *J*-modulated spectroscopies.
- Signal intensity may be diminished by half due to the amplitude modulation, as only one of the terms in Eq. (37) will be observed. Fig. 14 illustrates this with single-scan UF2DNMR experiments carried out on a *n*-butylchloride/$CDCl_3$ sample [33], demonstrating the differences between amplitude- and phase-modulated encodings. Higher signal intensity is observed in the phase-modulated case when examining the 1D projections of the spectra on the frequency axes.
- The $\frac{\pi}{2}$ chirps are more sensitive to RF inhomogeneities compared to the adiabatic π-chirps used in the other approaches.

The overall encoding time spent by the spins in the $\hat{x}\hat{y}$-plane also varies between methods, as revealed by comparing Eqs. (39), (36) and (34) for the cases of constant-time, amplitude modulation and phase modulation encoding, respectively. For a given z ordinate, the constant-time encoding mode offers the highest efficiency, followed by amplitude modulation and phase modulation. This feature is desirable for the same reason as it is in conventional 2D spectroscopy: it allows for finer resolution along the indirect domain for a given t_1^{max} – even if at the expense of increased relaxation losses. Moreover, the use of long, constant field gradients like those involved in Fig. 13 can introduce unwanted signal decay due to diffusion. Alternating the gradient field can reduce these effects [38], making the original discrete-based experiments (left outside the scope of this review [7,8]) less susceptible to diffusion artifacts than continuously modulated ones.

3.2. Decoding the information: 2D signals in a single acquisition

In spectroscopic experiments signals are collected as a function of time variables, and the desired spectrum is obtained by means of a numerical Fourier transform. In the cases that concern us here, where the sample has been partitioned into spatial elements encoded with different degrees of spin evolution, one will eventually have to acquire spectra from each of the spatial elements and discriminate between them; that is, to obtain spectra as a function of position. This is a form of *spatial-spectral acquisition*; the simplest sequence that can be used to this effect is shown in Fig. 15.

The challenge just outlined is, in fact, analogous to problems often encountered in MRI, dealing with the acquisition of spatially resolved images for sites with different chemical shifts. A single-scan solution to this problem was first proposed by Mansfield with Echo Planar Spectroscopic Imaging (EPSI) [39], in which signals are acquired in the presence of an alternating field gradient. The field gradient uncovers the position-dependent spin distribution; while its alternations refocus the gradients effects, allowing the chemical shift evolution to take place and modulate the signal. Hence, the overall signal resulting from a single-scan has both position and chemical-shift dependent interactions encoded into it.

Section 3.2.1 presents a heuristic overview of this acquisition method as applied to spatially encoded data, with a more rigorous formulation following in Section 3.2.2. In Section 3.3.5, EPSI will be discussed in a more general setting, stressing its role as a tool for recovering other types of spatial-spectral information from a sample.

3.2.1. Spatial-spectral acquisition of spatially-encoded NMR interactions

Consider the state just prior to acquisition of a set of spins having some chemical shift Ω_1 that was encoded spatially using any of the schemes[11] depicted in Fig. 13. Following the spatial encoding, spins will reside within the $\hat{x}\hat{y}$-plane and have a linear position-dependent phase of the form[12] $M_+(z) = M_0 e^{it_1(z)\Omega_1}$, where M_0 is some proportionality constant, $t_1(z) = Cz$, and C depends on the encoding method employed. Regardless of the details of the sequence, at the conclusion of the spatial encoding process the spins can be visualized as subtending a helix along the z-axis, similar to the one shown in Fig. 2. The degree of winding in this helix, however, will not be determined by an external gradient, but rather derive from the $C\Omega_1$ coefficient: the greater the chemical shift, the more tightly wound the helix. As in the case of a gradient-derived spiral, acquiring a signal from this state would yield merely noise: the acquired signal would be equal to the vectorial sum of signals originating from all spins in the sample, $s(t) \propto \int_{\text{sample}} M_+(z)dz$. Because spins in different regions of the sample point in different directions in the $\hat{x}\hat{y}$-plane, their signals would interfere destructively, canceling out when added vectorially.[13] Consider, however, what would happen if a signal were to be acquired while applying a gradient. Given

[11] No assumption will be made about the mixing used, as any phase shifts induced by the mixing will merely get added homogeneously to the phases created by the spatial encoding, and will modulate the peaks as in a conventional 2D NMR experiment.

[12] The actual phase may have additional terms as well, with its most general form given by Eq. (44). Although these terms have physical significance, they do not alter appreciably the conclusions derived in this section and are therefore set to zero.

[13] The signal would remain undetectable even if the spins are left to evolve according to their chemical shifts, $M_+(z) \rightarrow M_+(z)e^{i\Omega_2 t_2}$. Since all spins precess with the same angular frequency, the overall winding is conserved. This can be thought of as letting the helical shape presented in Fig. 16 rotate as a whole.

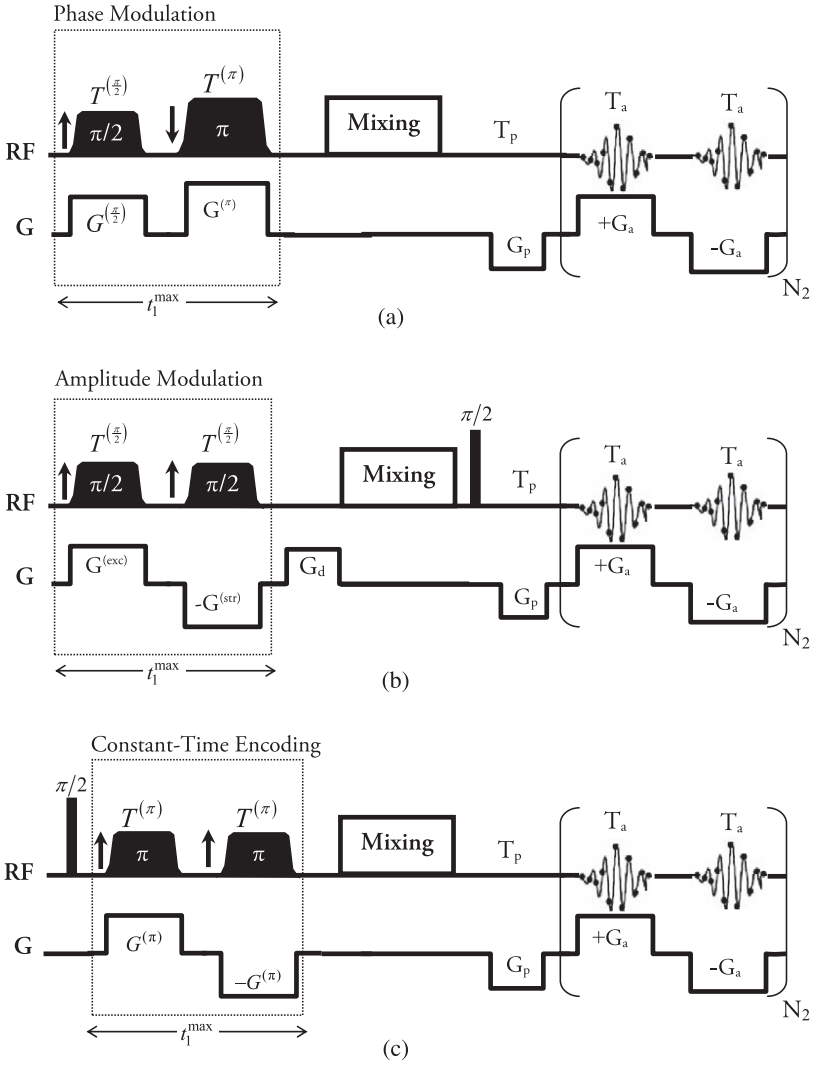

Fig. 13. Different schemes discussed in this article for creating a different effective t_1 evolution time in each slice. (a) Phase-modulated (PM) encoding. (b) Amplitude-modulated (AM) encoding. (c) Constant-time (CT) encoding. The arrows before each chirped pulse indicate the sign of ΔO, the bandwidth, which determines the directionality of the sweep (from negative to positive frequencies or vice-versa).

enough time, this gradient could unwind the spins, and align the spin packets constructively so as to form an echo. Applying the gradient any longer would wind the aligned spins once again, causing the signal to decay back into the noise.

This process is illustrated in Fig. 16 for two chemically inequivalent sites. Mathematically, it can be understood from the fact that during such an acquisition, the phases of the spins will evolve as $\phi_a(t) = C\Omega_1 z + \gamma G_a t z = (C\Omega_1 + \gamma G_a t)z$. It is seen that the spins align when[14] $C\Omega_1 + \gamma G_a t = 0$; that is, when $t_{\text{echo}} = -\frac{C}{\gamma G_a}\Omega_1$. The signal from several chemical shifts is the superposition of signals from the individual chemical shifts, so a sample containing n different chemical shifts, $\Omega_1^{(1)}, \Omega_1^{(2)}, \ldots, \Omega_1^{(n)}$ prior to mixing will form n echoes, at locations $t_{\text{echo}\,j} = -\frac{C}{\gamma G_a}\Omega_1^{(j)}$. Note that, since the position of an echo is proportional to Ω_1, *the acquired echo pattern will in fact be proportional to the spectrum along the indirect domain.*

The gradient's action just described is completely reversible: assuming no displacements, the spins can be rewound by following the positive gradient G_a with a negative one $-G_a$, having identical magnitude and duration. This has the effect of reversing whatever winding was induced during the positive gradient lobe: the phase added by the positive gradient, $\gamma G_a T_a z$, and the phase added by the negative gradient, $-\gamma G_a T_a z$, cancel out. Should a signal be acquired in the presence of this negative gradient, the echoes will form again, only in a reverse order, resulting in a pattern of echoes which is the mirror image of the one acquired in the presence of the positive gradient.

It would seem that – relaxation or diffusion notwithstanding – this process can be repeated indefinitely, leading to an identical train of echoes and their mirror images by alternating the gradient. This, however, would not take into account the fact that, alongside the gradient-induced winding, the spins precess according to their inherent t_2-dependent chemical shifts. Hence, the echoes emanating from each chemical site will get additionally modulated by a term of the form $e^{t\Omega_2 t_2}$, representing its evolution by the action of the direct-domain chemical shift Ω_2 (see Fig. 17a). This is the essence of the acquisition scheme: *by acquiring spatially encoded data in the presence of a gradient, one can observe the indirect-domain spectrum; by oscillating the gradient one can follow the $e^{t\Omega_2 t_2}$ envelope modulating the indirect-domain*

[14] In the event C is a positive quantity, G_a can be set to be negative, ensuring that $t_{\text{echo}} > 0$ – that is, that the echo is indeed observed, provided one acquires for a time greater than t_{echo}. For the purposes of the discussion in this section, it will be assumed that G_a should be positive.

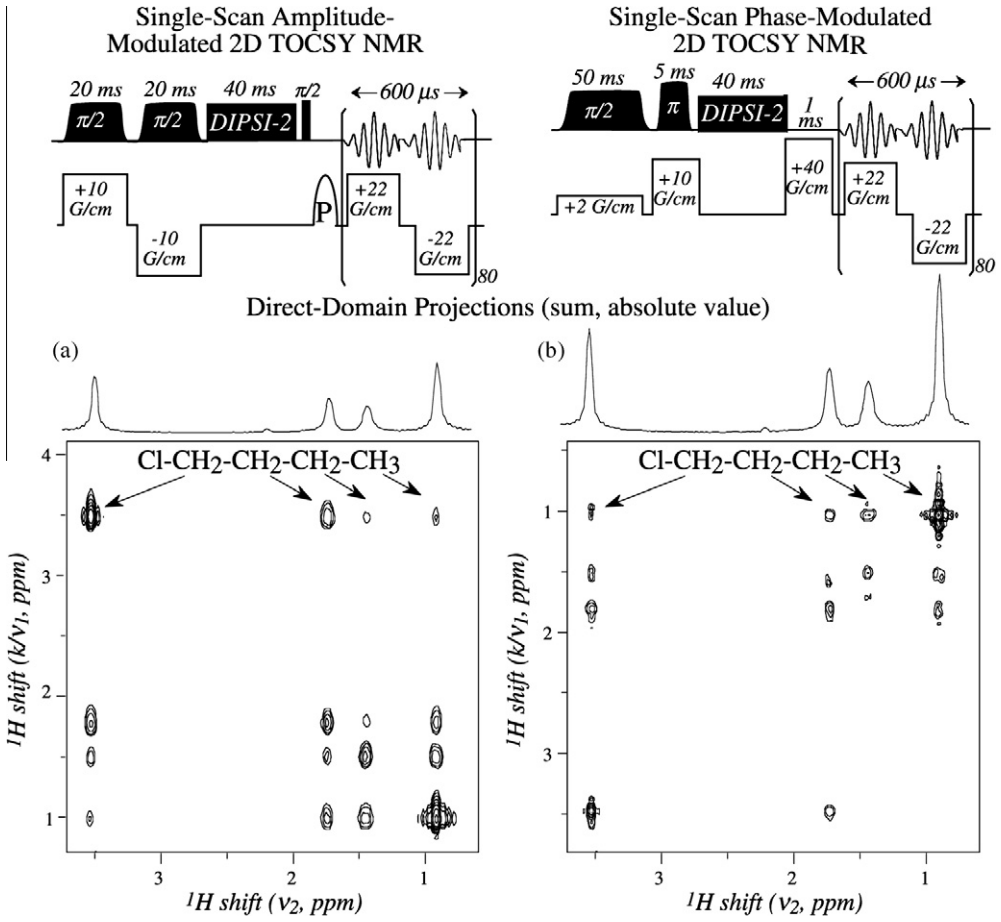

Fig. 14. Comparison between single-scan 2D TOCSY NMR spectra, acquired on a 500 MHz Varian iNova spectrometer, for an *n*-butylchloride/$CDCl_3$ sample, utilizing the amplitude-modulated (a) and the phase-modulated (b) pulse sequences indicated on top. Also shown for the sake of a sensitivity comparison are the projections obtained in each instance upon adding up all points along the indirect dimension (shown in absolute intensity mode). The effective t_1^{max} encoding times are 40 and 45 ms in (A) and (B), respectively. Additional relevant parameters were gradient switching times of 10 μs, an $L = 1.8$ cm sample length, and a 40 ms long DIPSI-2-type sequence applied in the absence of gradients and over a 15 kHz bandwidth for the mixing. Also important to note are the γB_1 settings used for the $\frac{\pi}{2}$ and π RF pulses: 200 and 1200 Hz, respectively.

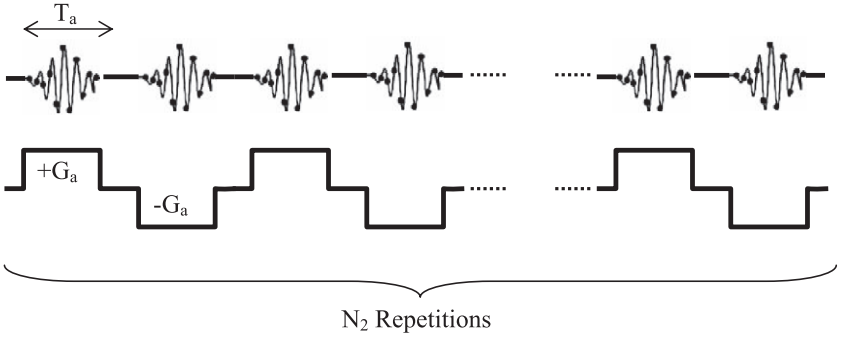

Fig. 15. Echo Planar Spectroscopic Imaging (EPSI) sequence, used to acquire a different FID (or, equivalently, 1D spectrum) per position. In this sequence data are acquired throughout the action of an alternating gradient, shown here explicitly by the black dots.

echoes; that is, the evolution along the direct domain. Thus, the $\Omega_1 - t_2$ plane can be covered, and a 2D spectrum acquired within a single-scan, by Fourier processing of such data versus t_2 (Fig. 17b–e).

3.2.2. Mathematical formulation of the gradient-driven decoding

During the process outlined in Fig. 17a, the acquisition phase of a spin having a particular position z will evolve as a function of the acquisition time t_2, as:

$$\phi_a(z, t_2) = C\Omega_1 z + k(t_2)z + \Omega_2 t_2. \quad (40)$$

Notice the distinction between Ω_1, the indirect-domain chemical shift prior to mixing, and Ω_2, the chemical shift following the mixing.[15] The variable $k(t_2) = \gamma \int_0^{t_2} G_a(t')dt'$, like the one introduced in

[15] This is a distinction worth stressing: the purpose of a mixing sequence is to transfer magnetization between coupled spins. Hence, spins having a chemical shift Ω_1 will transfer their magnetization (and winding) to spins having some other chemical shift Ω_2; for instance, through couplings. Those spins would then precess during acquisition with an off-resonance frequency given by Ω_2. It is quite possible for Ω_1 to transfer its magnetization to several spins; in this case, the overall chemical shift evolution will reflect a linear superposition of the individual evolutions. This discussion will confine itself to a particular chemical shift, Ω_2, along the direct domain.

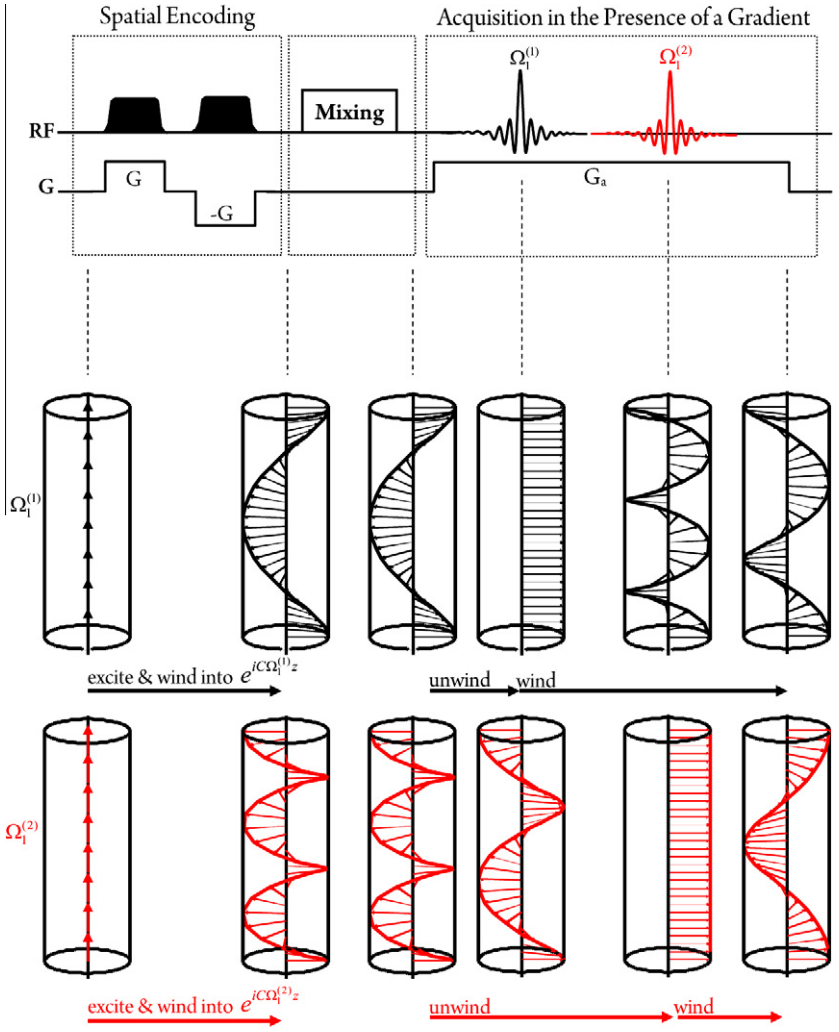

Fig. 16. Acquisition in the presence of a gradient for a sample containing two chemical shifts, $\Omega_1^{(1)}, \Omega_1^{(2)}$. During spatial encoding, the spins are excited onto the $\hat{x}\hat{y}$-plane and wound up along the z-axis, in helices whose pitch is proportional to their respective chemical shifts. Once encoded, mixing is applied. Note that, since the mixing is not spatially selective, their relative spatial phases do not change, and hence the winding is preserved. A gradient is then turned on and a signal is acquired. As the different chemical shifts unwind they form *echoes*. Each chemical shift forms a single echo, at a time $t^{(j)} = \frac{C}{\gamma G_a}\Omega_1^{(j)}$, when the spins associated with it align constructively. The total signal is a superposition of the signals originating from the different chemical shifts. The time axis is hence seen to be proportional to the chemical shift prior to mixing, and the pattern of echoes – to the indirect spectrum. (Note that the process portrayed here has been idealized – precession due to chemical shifts has been neglected, and the encoding process is assumed to be ideal.)

Section 2.1, is used to express the total area under the gradient up to time t_2. The value of $k(t_2)$ therefore increases and decreases periodically, with a period $2T_a$, equal to two gradient lobes.

The signal $s(t_2)$ induced by the spins at a time t_2 into the acquisition is proportional to the vector sum of the projections of the magnetization vectors in the sample on the $\hat{x}\hat{y}$-plane. Written in complex form, this is:

$$s(t_2) \propto \int_{-\frac{L}{2}}^{\frac{L}{2}} M_+(z,t_2)dz, \tag{41}$$

where $M_+(z,t_2) = M_x(z,t_2) + \imath M_y(z,t_2) = M_0 e^{\imath\phi_a(z,t_2)}$, and M_0 is proportional to the sample's concentration, which shall be assumed constant. Given the simple form of $M_+(z,t_2)$, Eq. (41) can be integrated to yield:

$$s(k,t_2) \propto LM_0 e^{\imath\Omega_2 t_2}\mathrm{sinc}\left(\frac{(C\Omega_1 + k(t_2))L}{2}\right). \tag{42}$$

Eq. (42) expresses formally the appearance of echoes illustrated in Fig. 16. Note that, in accordance with Fig. 16:

1. The lineshape of the echo is given by a sinc function. This derives from our assumption of a constant profile effective spatial throughout. In actuality, T_2 or diffusion related losses will modulate this profile leading to different, complex (e.g., dispersive) lineshapes.
2. The location of the echo's peak occurs when $\mathrm{sinc}\left(\frac{(C\Omega_1+k(t_2))L}{2}\right)$ is maximal, that is, when $C\Omega_1 + k = 0$, or $k = -C\Omega_1$. This quantity depends solely on the spatial encoding and is proportional to the chemical shift prior to mixing (see Table 2). The k-axis therefore acts as the indirect-domain frequency axis, scaled by C.
3. The width of the echo, when plotted as a function of k, will be the width of the sinc function and given by $\sim\frac{1}{L}$. When plotted as a function of t_2 it is $\frac{1}{\gamma G_a L}$. And when considered in terms of ν_1, its width is $\Delta\nu_1 = |\Delta k/C| \approx \frac{1}{t_1^{max}}$, where t_1^{max} is the total encoding time (see Fig. 13). The indirect-domain spectral resolution in UF2DNMR is thus given by the inverse of the overall encoding time, as in conventional spectroscopy.

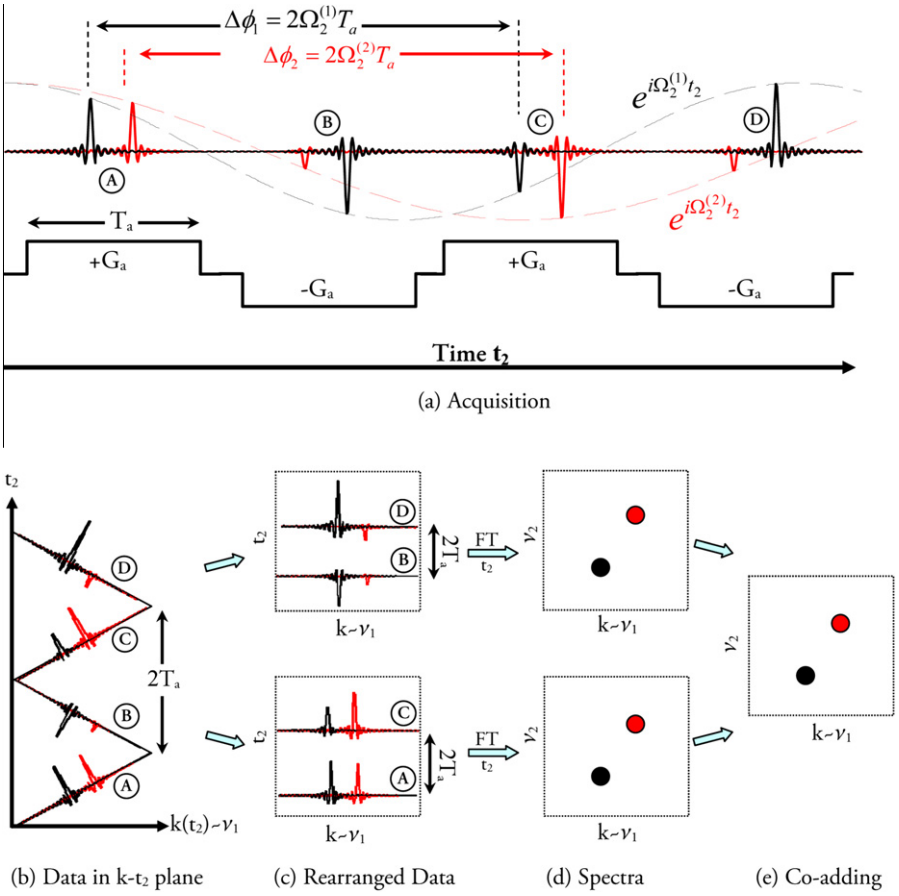

Fig. 17. Ultrafast 2D acquisition protocol and post-processing. (a) The signal in an UF2DNMR experiment is acquired in the presence of an alternating gradient. The echoes originating from the spins having a chemical shift Ω_2 are modulated by $e^{i\Omega_2 t_2}$. (b) The signal viewed in a 2D $k-t_2$ space, where $k = k(t_2) = \gamma \int_0^{t_2} G_a(t')dt'$. Note that $k(t_2)$ represents the total area under the gradient and hence periodically increases and decreases as G_a flips sign. (c) To reach a final spectrum the positive (A and C) and negative (B and D) gradient data sets are separated. (d) Each data set is Fourier transformed over its t_2 coordinate, with the dwell time being $2T_a$. (e) The data sets can then be co-added to enhance the overall sensitivity.

4. The echo is modulated by an envelope $e^{i\Omega_2 t_2}$, implying that $s(k,t_2)$ is in fact an indirect-domain frequency/direct-domain time 2D interferogram. Thus, all it requires is a realignment of its data points and a Fourier transform along t_2 to yield the desired 2D NMR spectrum. Indeed, the periodicity of $k(t)$ discussed earlier implies that $k(t_2 + 2T_a) = k(t_2)$ for all t_2. In particular, computing the phase difference $\Delta\phi_a$ between two peaks separated by $2T_a$ gives:

$$\Delta\phi_a = (C\Omega_1 z + k(t_{\text{echo}} + 2T_a) + \Omega_2(t_{\text{echo}} + 2T_a)) - (C\Omega_1 z + k(t_{\text{echo}}) + \Omega_2 t_{\text{echo}}) = \Omega_2 2T_a. \quad (43)$$

Thus, the echo peaks are modulated solely by the chemical shift evolution during acquisition, independent of the gradient, as illustrated in Fig. 17a.

It is useful, for reasons that will become apparent shortly, to think of k and t_2 as independent variables.[16] Each data point has a particular value of (k,t_2) associated with it, and can therefore be viewed as being acquired in the $k-t_2$ space along a trajectory defined by $k(t_2)$, as shown in Fig. 17b. To implement the remaining Fourier transform along t_2, the data can then be separated and rearranged into two sets (Fig. 17c). These data sets contain points acquired during the positive and negative gradient lobes, respectively, and they are *separable* in the sense that their rows are proportional to the spectrum along the indirect domain, while their columns – all of whose points are a $2T_a$ dwell-time apart – are modulated *solely* by the post-mixing chemical shifts Ω_2 (Eq. (43)). Fourier transforming over the columns (the t_2 axis) at this point yields the direct-domain spectrum, and hence the desired 2D spectrum being sought (Fig. 17d). These two data sets, containing in principle identical 2D spectral content, can be subsequently phased, re-registered (this would account for gradient and sampling non-idealities) and combined for the purpose of enhancing the sensitivity.

[16] Although k depends on t_2 it can be viewed as an independent variable, since it also depends on $G_a(t)$, which can be varied independently of t_2.

3.3. Practical considerations in ultrafast 2D NMR

Any two-dimensional spectrum involves a set of parameters, including the full widths at half height (FWHH) $\Delta\nu_i$ $(i = 1,2)$ of the peaks, the covered spectral widths SW_i $(i = 1,2)$, as well as the signal-to-noise ratio (SNR), that define the overall quality and ability of a method to discern the spectral information. The current section takes a closer look at these quantities in single-scan 2D NMR, and discusses additional issues such as the line shapes and the use of purge gradients to shift the indirect-domain spectrum. In what follows, SW_j will be used for describing the spectral widths, $\Delta\nu_j$ for the peaks' FWHH, $N_i = \frac{\text{SW}_i}{\Delta\nu_i}$, δt_j for the dwell time and t_j^{max} for the maximal acquisition time along the indirect $(j = 1)$ and direct $(j = 2)$ acquisition domains (t_1 and t_2, respectively).

3.3.1. Spectral characteristics

We survey next explicit expressions for the spectral width and resolution, $\text{SW}_j, \Delta\nu_j$, along the indirect $(j = 1)$ and direct $(j = 2)$

axes. In conventional 2D NMR data are sampled in the $t_1 - t_2$ plane, and $SW_j, \Delta\nu_j$ are determined by the sampling rates and time spans, as dictated by Nyquist's theorem [40]: $SW_j = \frac{1}{\delta t_j}, \Delta\nu_j = \frac{1}{t_{j,\max}}$, where δt_j is the dwell time and $t_{j,\max}$ is the maximal sampling time along the t_j-axis. Data in UF2DNMR is not acquired in the $t_1 - t_2$ plane, but rather along $k/\nu_1 - t_2$. As seen in Section 3.2, the data along the t_2 axis is modulated solely by the chemical shift, with a dwell time of $2T_a$ and a maximal acquisition time $2N_2T_a$, where N_2 is the number of gradient repetitions. Hence, the resolution along the t_2 axis after its Fourier transform, is given by $SW_2 = \frac{1}{2T_a}, \Delta\nu_2 = \frac{1}{2N_2T_a}$. The k-axis is proportional to the indirect-domain's frequency axis, ν_1, with a proportionality constant given by C - the spatio-temporal coefficient summarized in Table 2. As discussed in Section 3.2.2, the width of a k-domain echo arising from a sample length L will be given by $\frac{1}{L}$, while the maximal k-value that will be monitored will be given by $k_{\max} = \gamma G_a T_a$. Dividing these quantities by C yields the desired spectral width and resolution obtainable in units of frequency: $SW_1 = |\frac{k_{\max}}{C}|, \Delta\nu_1 = |\frac{1}{CL}|$. These findings are summarized in Table 1 for the various spatial-encoding methods discussed in this review.

3.3.2. Practical aspects of spatial encoding

The discussion in Section 3.2 assumes an ideal spatial encoding; i.e., spins endowed with a phase $C\Omega_1 z$ just prior to acquisition. In practice, additional terms may appear as well. The most general form for the phase resulting from the spatial encoding reads:

$$\phi_e(z, \Omega_1) = C\Omega_1 z + bz + a_1\Omega_1 + a_0, \tag{44}$$

where b, a_1, a_0 are independent of Ω_1 and z. Table 2 summarizes the values of these constants for the three encoding methods discussed in Section 3.1.

The presence of the terms b, a_1, a_0 and their implications warrant further discussion. The constant phase e^{ia_0} affects all peaks in the spectrum identically, and can be compensated for by using conventional zero-order phasing methods. The linear term bz, shared equally by all indirect-domain chemical shifts, will uniformly shift the echo pattern acquired along the k-axis. It represents an additional winding of the spins along the z-axis; hence it behaves spectrally as a uniform indirect-domain offset shift. This can be seen formally by writing down the phase during the acquisition:

$$\begin{aligned}\phi_a(k, t_2) &= \phi_e(z, \Omega_1) + kz + \Omega_2 t_2 \\ &= \phi_e(z, \Omega_1) + (k + b)z + a_1\Omega_1 + a_0 + \Omega_2.\end{aligned} \tag{45}$$

The variable k, and hence ν_1, to which it is proportional, is shifted in Eq. (45) by an amount $-b$. Since the exact dependence of b on the experimental parameters is known, it is possible to do away with it completely by applying a *purge* gradient G_p for a time T_p before beginning the acquisition, such that $\gamma G_p T_p = -b$ [29]. In general, pre-acquisition purge gradients can also be used to shift the echoes – and hence the indirect-domain spectrum – by an amount $\Delta k = \gamma G_p T_p$; this can also be thought of as shifting the origin of the k-axis by an amount $-\Delta k = \gamma G_p T_p$. The need to reposition the offset of the variable k can arise in several situations. The reliance on amplitude modulation of Ω_1 values might result in echoes that appear at negative k-values, and hence would not be observable using the trajectory in $k - t_2$ space appearing in Fig. 17b. By shifting the origin of the k-axis one can ensure the entire pattern fits within the window $k \in [0, k_{\max}] \equiv [0, \gamma G_a T_a]$. The precise calibration of this shifting includes choosing a proper point where to insert G_p in the sequence, and may need to be fine-tuned by performing an arrayed experiment – for instance, incrementing G_p and observing the echo pattern in a reference sample. Also important, pre-acquisition purging is often an essential requirement for eliminating axial artifacts of the experiment, as well as for coherence selection pruposes.

Two additional parameters pertaining to the spatial encoding process and deserving mention are the gradient G_e and the chirp bandwidth ΔO. In the presence of a field gradient G_e, spins having a chemical shift Ω_1 will span a range of frequencies ranging from $\Omega_1 - \frac{\gamma G_e L}{2}$ to $\Omega_1 + \frac{\gamma G_e L}{2}$, where L is the physical size of the sample (see Fig. 18). Since the sample contains many spins with differing chemical shifts, it is impossible to tailor the bandwidths ΔO to excite them all perfectly; there will always be either frequency regions which do not get irradiated (leading to a partial excitation of the spins and to diminished signal intensity), or frequency regions which are irradiated but contain no spins (leading to a site-dependent non-uniform $t_1(z)$). These regions can, however, be minimized, provided $\Delta O = \gamma G_e L \gg SW_1$, where SW_1 is the spectral width of the indirect domain – that is, the spread of chemical shifts prior to mixing. A typical value of SW_1 for protons is 5 kHz, so, for a standard 20 mm sample,

$$G \gg \frac{1}{2}\frac{\text{kHz}}{\text{mm}} \approx 1\frac{\text{Gauss}}{\text{cm}}, \tag{46}$$

suggesting a minimal value of 10 Gauss/cm for G_e. Increasing G_e beyond such values would only serve to introduce losses and distortions due to molecular diffusion [41,42].

3.3.3. Line shape considerations

The two-dimensional spectrum acquired in UF2DNMR has a distinct asymmetry built into it: the indirect $k \sim \nu_1$ spectral axis

Table 2
Coefficients defining the spins' phase following spatial encoding (Eq. (44)).

	C	b	a_1	a_0
Amplitude-mod.[a]	$-\frac{t_1^{max}}{L}$	0	$\frac{t_1^{max}}{2}$	$-\frac{\pi}{2}$
Phase-mod.[b]	$\frac{t_1^{max} - 3T^{(\pi)}}{L}$	$\frac{\gamma G^{(\frac{\pi}{2})} T^{(\frac{\pi}{2})}}{2}$	$-\frac{T^{(\frac{\pi}{2})}}{2}$	$-\frac{\gamma G^{(\frac{\pi}{2})} T^{(\frac{\pi}{2})} L}{4}$
Constant-time[c]	$\frac{-2t_1^{max}}{L}$	0	0	0

[a] The frequency sweep of the chirp is assumed symmetric and set to $\Delta O = \gamma G_e L$.
[b] The variable t_1^{max} has been used to denote to total encoding time. For amplitude modulation, it equals $T^{(\frac{\pi}{2})}$; for constant-time encoding, it equals $T^{(\pi)}$.
[c] For phase encoding, $T^{(\frac{\pi}{2})} G^{(\frac{\pi}{2})} = 2T^{(\pi)} G^{(\pi)}$.

Table 1
Spectral characteristics in UF2DNMR experiments.

	SW_1	N_1	$\Delta\nu_1$	SW_2	N_2	$\Delta\nu_2$
Spatial-encoding[a]	$\frac{k_{\max}}{C}$	$Lk_{\max}$	$\frac{1}{CL}$	$\frac{1}{2T_a}$	Number of gradient repetitions	$\frac{1}{2T_a N_2}$
Constant-time	$\frac{\gamma G_a T_a L}{2T_{e,tot}}$		$\frac{1}{2T_{e,tot}}$			
Amplitude-modulation	$\frac{\gamma G_a T_a L}{T_{e,tot}}$		$\frac{1}{T_{e,tot}}$			
Phase-modulation[b]	SW_1		$\frac{1}{T^{(\frac{\pi}{2})} - T^{(\pi)}}$			
Conventional	$\frac{1}{\delta t_1}$	$\frac{t_{1,\max}}{\delta t_1}$	$\frac{1}{t_{1,\max}}$	$\frac{1}{\text{dwell time}}$	Number of acquired points	$\frac{1}{T_{\text{acquisition}}}$

[a] If the positive and negative gradient data sets are interlaced [76], SW_2 can be doubled, $SW_2 = \frac{1}{T_a}$, without affecting any other experimental parameters.
[b] Assuming $2G^{(\pi)}T^{(\pi)} = G^{(\frac{\pi}{2})}T^{(\frac{\pi}{2})}$.

is monitored via gradients leading to the formation of echoes, while the direct spectral axis is obtained by observation of the chemical shift modulation of those echoes with an effective dwell time of $2T_a$ and total acquisition time of $2N_2T_a$. As a result, the direct domain displays all of the characteristic traits of a conventional Fourier transform NMR spectrum, in terms of the spectral width (SW_2), resolution ($\Delta\nu_2$) and the control of its central carrier offset. Yet the novelty of the spatially-encoded indirect domain deserves a more in-depth analysis.

The form of an echo along the k (indirect) axis is given by Eq. (42). Its width is $\frac{1}{L}$ when viewed as a function of k, or $\frac{1}{\gamma GL}$ when viewed as a function of ν_1. Its magnitude at peak intensity is M_0L, up to a constant depending on the geometry of the coil and the electronic properties of the receiver and console (and therefore shared equally by all experimental schemes). The assumption made in the derivation of Eq. (42) was an excitation phase of the form of Eq. (44), with $a_0 = a_1 = b = 0$. According to the discussion in the previous section, there is no loss of generality in assuming $b = a_0 = 0$, but a_1 must be taken into account, yielding the following general form for the echoes:

$$s(k,t_2) \propto LM_0 e^{\imath\Omega_2 t_2}\left[\mathrm{sinc}\left(\frac{(C\Omega_1 + k(t_2))L}{2}\right)e^{\imath a_1\Omega_1}\right]; \tag{47}$$

a_1 therefore behaves as a first-order phase distortion along the indirect domain. Though *a-priori* known, correcting for this kind of distortion can be challenging. Further challenges arise upon including the effects of T_2 relaxation which have been so far neglected. In actuality we recall that a single 1D spectroscopy experiment yields a signal of the form

$$s(t) = \begin{cases} e^{\imath 2\pi\nu_{cs}t - \frac{t}{T_2}} & \text{if } t \geqslant 0 \\ 0 & \text{otherwise.} \end{cases} \tag{48}$$

When Fourier transformed, this yields the well known Lorentzian spectral line shape:

$$I(\nu) = \frac{T_2}{1+(2\pi T_2(\nu_{cs}-\nu))^2} + \imath\frac{2\pi T_2^2(\nu_{cs}-\nu)}{1+(2\pi T_2(\nu_{cs}-\nu))^2} \equiv A(\nu) + \imath D(\nu), \tag{49}$$

where the real and imaginary parts, $A(\nu)$ and $D(\nu)$, are the absorptive and dispersive parts of the spectrum. The appearance of a dispersive component $D(\nu)$ is due to $s(t)$'s asymmetry about $t = 0$. In 1D NMR this is not an insoluble complication, as $s(t<0)$ and $s(t>0)$ are related, and hence the effects of $D(\nu)$ can be compensated. The presence of a dispersive component is known to be more problematic in 2D spectroscopy [55]. If data are acquired along positive t_1 and t_2 axes, $s(t_1,t_2) = e^{\imath\Omega_1 t_1 - \frac{t_1}{T_2} + \Omega_2 t_2 - \frac{t_2}{T_2}}$ for $t_1, t_2 \geqslant 0$, and the corresponding 2D spectrum becomes the product of the individual lineshapes along both axes. Extending Eq. (49), this means:

$$\begin{aligned} I(\nu_1,\nu_2) &= [A(\nu_1) + \imath D(\nu_1)][A(\nu_2) + \imath D(\nu_2)] \\ &= [A(\nu_1)A(\nu_2) - D(\nu_1)D(\nu_2)] \\ &\quad + \imath[A(\nu_1)D(\nu_2) + D(\nu_1)A(\nu_2)]; \end{aligned} \tag{50}$$

both the real and imaginary parts of the spectrum thus become entangled. The resulting peaks, plotted in the $\nu_1 - \nu_2$ plane, exhibit a phenomenon known as *phase twisting*. One could use the absolute magnitude of $I(\nu_1,\nu_2)$, but this leads to a loss of resolution, as well as to peak cancellation problems (Fig. 19a). A solution of this dilemma stems from the realization that the indirect t_1 variable does not involve physical time, and therefore by suitable manipulations of equivalent negative t_1 values may be sampled as well (e.g., by collecting echo/anti-echo 2D sets). The resulting Fourier transform along the t_1 axis, $I(\nu_1)$, will then involve transforming $e^{\imath 2\pi\nu_{cs}t_1 - \frac{|t_1|}{T_2}}$ over a symmetric domain, $t_1 \in [-t_{1,\max}, t_{1,\max}]$, as opposed to $t_1 \in [0, t_{1,\max}]$. As the Fourier transform of a symmetric function over a symmetric domain is real, the resulting lineshape will have no imaginary part: $D_1(\nu_1) = 0$, and as a result

$$I(\nu_1,\nu_2) = A(\nu_1)A(\nu_2) + \imath A(\nu_1)D(\nu_2). \tag{51}$$

The real part of the spectrum has thus lost the twisted phase. Another option is offered by constant-time acquisitions: indirect domain relaxation effects will then produce a uniform, t_1-independent signal loss. While associated with a SNR penalty, this avoids the $e^{-\frac{t_1}{T_2}}$ modulation and the introduction of dispersive components along ν_1. One can summarize this by saying that twisted peaks appear in conventional 2D NMR as a result of both the indirect and direct domain having progressive relaxation effects; this can be remedied by sampling the t_1 indirect domain symmetrically vis-a-vis T_2 decay, or by having a uniform T_2 decay for all t_1 values. Either of these yields 2D peaks for which $D(\nu_1) = 0$.

The known arguments just stated can be extended to the single-scan case, with the provision of replacing t_1-related concepts with z-related ideas. Indeed, UF2DNMR acquires its 2D data set in the $k - t_2$ plane. The considerations outlined above readily apply to the t_2, direct-domain axis, which is sampled and Fourier transformed in the conventional sense and hence will contain a dispersive $D(\nu_2)$ component. Analogously to the conventional 2D case, the indirect-domain spectrum arises as a result of an analog FT along the z-axis (e.g., the outer integral in Eq. (64)). Its k-axis echo pattern will therefore have a dispersive component as well, so long as the different slices along the sample have not been encoded symmetrically about $z = 0$. The appearance of a progressive z-dependent T_2 decay is illustrated for the case of amplitude-modulated encoding (Section 3.1.2) in Fig. 19b. As different slices are excited and stored at different times, each slice will be affected differently by relaxation while in the xy-plane, forming a spatial relaxation envelope. Formally, one would have, at the end of the encoding, a spatial spin distribution in the Bloch sphere of the form $M_+(z) = M_0 e^{\imath t_1(z)\Omega_1 - \frac{t_1(z)}{T_2}}$, where $t_1(z) = Cz$. This is analogous to the conventional t_1 effect described above, and the shapes of the resulting echoes, given by

$$s(t_2) = \int M_+(z)dz = \int M_0 e^{t_1(z)\Omega_1 - \frac{t_1(z)}{T_2}}dz, \tag{52}$$

will have a dispersive component by virtue of the asymmetry of $M_+(z)$. A possible solution to this problem includes the use of encoding schemes, such as constant-time encoding, in which all

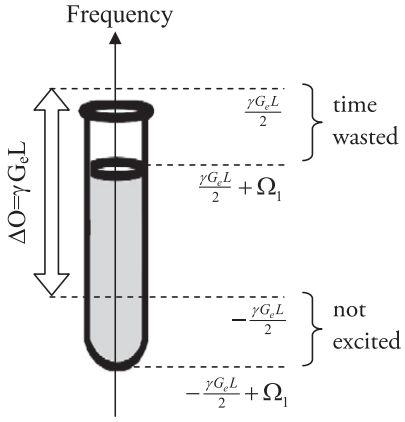

Fig. 18. In practical applications, a chirp's bandwidth is chosen to span the entire sample, $\Delta O = \gamma G_e L$, where L is the sample's physical size. However, spins with different chemical shifts will span slightly different frequency ranges, leading to both wasted time (during which no spin is irradiated) and spins which are never excited in the sample. To minimize these effects, one chooses G_e such that $\Delta O \gg SW_1$, where SW_1 is the spectral width along the indirect domain.

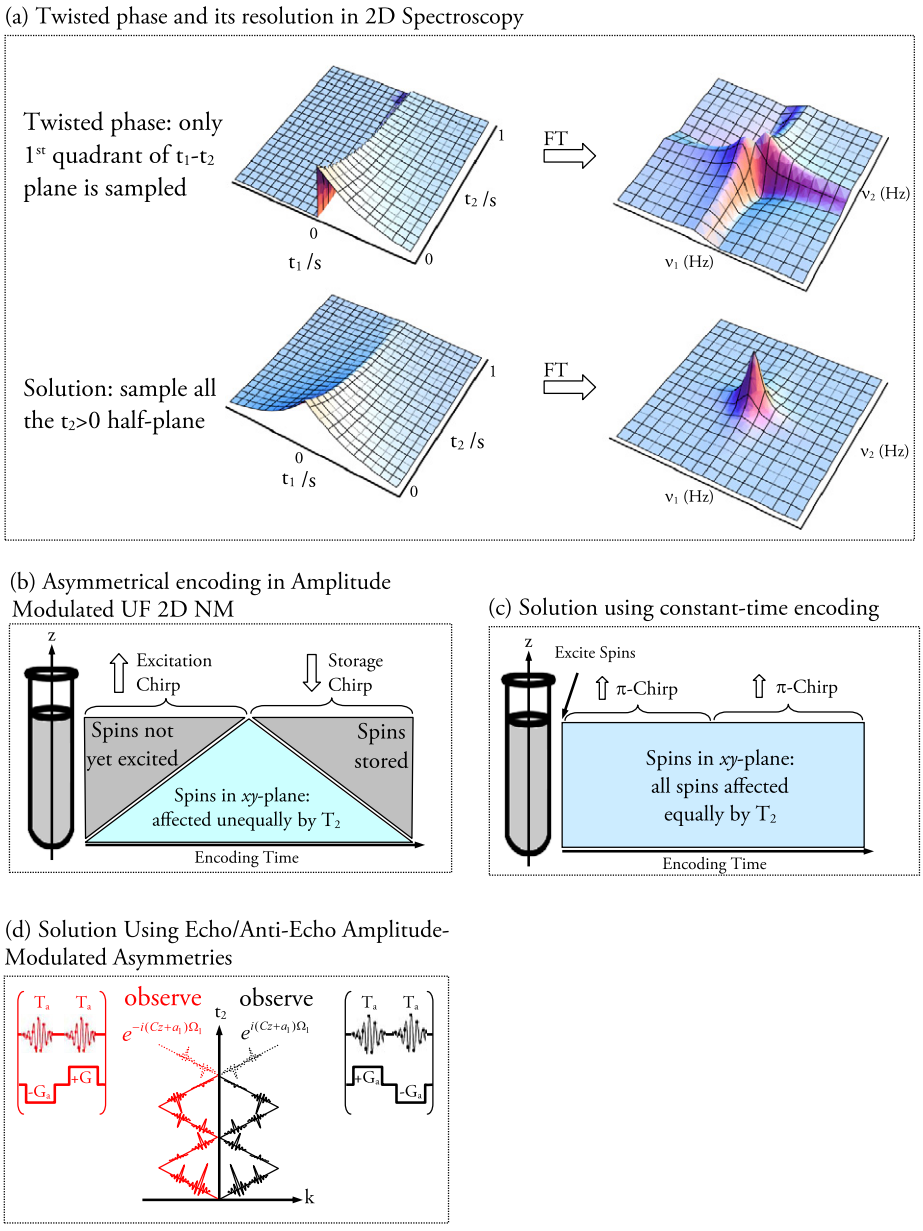

Fig. 19. (a) The absolute magnitude of data sampled in the $t_1 - t_2$ plane. Left: sampling just one quadrant of the $t_1 - t_2$ plane results in dispersive components along both axes and, hence, twisted phase. Right: the resolution is to sample the t_1 axis symmetrically, eliminating the dispersive component along ν_1. (b) In UF2DNMR, amplitude-modulated encoding leads to different slices residing in the xy-plane for different amounts of time, creating an asymmetrical spatial decay envelope, leading to a dispersive component along the acquisition's k-axis. (c) One possible resolution is to use constant-time encoding, in which all slices spend the same amount of time in the xy-plane, and are equally affected by T_2, leading to a symmetric spatial profile. (d) Another solution is to use the two phases arising in an amplitude-modulated encoding, and conduct one or two experiments that observe spatially the two terms in Eq. (37), which result in data sets along the k-axis with inverted dispersive components.

slices remain in the $\hat{x}\hat{y}$-plane for the same amount of time (this is illustrated in Fig. 19c). Another option is shown in Fig. 19d; it relies on the fact that, when the spins are stored, two spatial mirror-images of the spin distribution – akin to the echo/anti-echo modulations mentioned earlier – are retained. These can be distinguished during the acquisition (Eq. (37)). One of the terms can be observed by monitoring the positive k-values, while the other can be observed by monitoring the negative k-values. This can be achieved in two separate experiments with inverted gradient patterns [22], as shown in Fig. 19d; alternatively, they can be monitored in a single scan, at the expense of shifting the whole pattern and doubling the k_{max} range. Regardless of the route, each resulting data set will have dispersive components along the k-axis, equal in magnitude but opposite in sign. Adding them up ensures the indirect-domain echoes are purely absorptive – mimicking the conventional 2D case.

In addition, options that find no direct counterpart in conventional 2D NMR may arise in the spatially-encoded experiments. These include, for example, the use of symmetric encoding schemes, such as those discussed in [30].

In addition to these encoding-related phase distortions and corrections, the presence of the $\Omega_2 t_2$ phase in Eq. (49) is a general feature of the indirect-domain acquisition. As data is acquired along a skewed trajectory which is not parallel to the k-axis (see Fig. 17b), time-delays and first-order phase distortions will be present. But no special considerations related to the lineshapes along ν_2 will arise.

3.3.4. Signal to noise

Signal-to-noise ratio (SNR) is a key practical aspect when considering the implementation of a UF2DNMR experiment. Indeed,

the fact that all the information pertaining to $I(\nu_1, \nu_2)$ can be gathered in a single-scan does not mean that such a speed-up will be possible: only if the SNR is sufficiently good will this be the case. Should the SNR be insufficient, signal averaging would be an option – yet an unappealing one if the number of scans that needs to be averaged approaches the number of N_1 increments in a conventional acquisition. We thus devote this section to a discussion of the SNR in UF2DNMR experiments.

NMR sensitivity is usually defined as the ratio of the height of a spectral peak divided by the root-mean-square (rms) of the surrounding noise. It is convenient to compute this quantity using a discretized version of the signal; this offers no loss of generality, even without taking into account that the signals are indeed digitized and sampled before being stored. Moreover, it is illustrative to first review SNR issues in conventional 1D NMR, as these notions can then be extended and used to compare the SNR of single-scan and conventional 2D NMR spectroscopy.

The digitized signal from a basic pulse-acquire 1D experiment carried out on a sample having a single chemical shift Ω and a magnetization per unit length M_0 is:

$$s_j = s(j\delta t) = \int dz M_0 e^{i\Omega j\delta t - \frac{j\delta t}{T_2}} \quad \text{for } j = 0, 1, 2, 3, \ldots N-1, \tag{53}$$

where δt is the dwell time, the integral sums up the contributions from all the spins in a sample of length L, and N is the number of acquired points, taken to be large enough for the signal to decay below the noise level. For the purpose of calculating the SNR, it can be assumed without loss of generality that $\Omega = 0$ (the signal intensity will not depend on the chemical shift, which merely displaces the peak without altering its form). Fourier transforming s_j, one obtains the discrete spectrum[17]:

$$\hat{s}_k = \frac{1}{\sqrt{N}} \sum_{j=0}^{N-1} s_j e^{\frac{2\pi ijk}{N}} = \frac{LM_0}{\sqrt{N}} \frac{1}{1 - e^{-\frac{\delta t}{T_2}} e^{\frac{2\pi ik}{N}}} \quad \text{for } k = 0, 1, 2, \ldots, \mathrm{N}-1. \tag{54}$$

The maximum of $\hat{s}_k$, corresponding to the peak's maximum intensity, occurs for $k = 0$, at which point $\hat{s}_0 = 1/\left(1 - e^{-\frac{\delta t}{T_2}}\right)$. Expanding in the small quantity $\delta t/T_2$, the intensity of the peak becomes:

$$\hat{s}_{\max} = \frac{LM_0}{\sqrt{N}} \frac{T_2}{\delta t} \approx \sqrt{N} L M_0, \tag{55}$$

where it has been assumed that the total acquisition time, t^{max}, has been set on the order of T_2. As a result, $T_2/\delta t \approx T_a/\delta t = N$. Different decay envelopes may change Eq. (55) by a factor on the order of unity.

To complete the evaluation of the SNR, the noise in the frequency domain must be evaluated. Let $n_0, n_1, n_2, \ldots, n_{N-1}$ denote the noise sampled in the time-domain, and let $n_{\mathrm{rms}} = \sqrt{\frac{1}{N}\sum_{p=0}^{N-1} |n_p|^2}$ be its root-mean-square. It can be shown, using the properties of the discrete Fourier transform, that the rms of the noise in the frequency domain, $\hat{n}_{\mathrm{rms}}$, is equal to its rms in the time-domain:

$$\hat{n}_{\mathrm{rms}} = \sqrt{n_{\mathrm{rms}}}. \tag{56}$$

As a result,

$$\mathrm{SNR}_{1D} = \frac{\sqrt{N} LM_0}{\hat{n}_{\mathrm{rms}}} = \frac{\sqrt{N} LM_0}{n_{\mathrm{rms}}}. \tag{57}$$

Two remarks should be made about this expression. (i) The SNR is proportional to $\sqrt{N}$, the number of acquired points. This can be thought of as a form of built-in signal averaging; (ii) Although the precise form of the noise depends on the electronics of the system (a detailed analysis of which is beyond the scope of this review) it will be noted that n_{rms} will in general depend on the sampling filter's bandwidth (fbw). Indeed, before being digitized, signals are passed through a low pass filter, removing any frequencies above a certain threshold. The value of fbw is often set equal to the spectral width of the sample, so as to ensure that high-frequency noise components do not get folded into the observed spectral range. It is possible to show that n_{rms} scales as $\sqrt{\mathrm{fbw}}$; for example, doubling the observed spectral width, and hence the filter-bandwidth, increases the noise by $\sqrt{2}$.

A conventional 2D experiment consists of an array of N_1 1D experiments. The SNR of each experiment in the array is given by Eq. (57). Assuming N is replaced by N_2, the number of points acquired along the direct domain, a second Fourier transform along the indirect domain will then increase the SNR by an additional factor of $\sqrt{N_1}$ (the noise rms remains unchanged, and physical factors M_0, L only apply to the directly sampled direct domain – i.e., the indirect domain's signal is not $M_0 L e^{i\Omega_1 t_1}$ but rather $e^{i\Omega_1 t_1}$). Thus,

$$\mathrm{SNR}_{2D} = \frac{\sqrt{N_1 N_2} LM_0}{n_{\mathrm{rms}}}. \tag{58}$$

It is seen that the SNR increases as the number of experiments N_1 is incremented – yet another form of signal averaging built-in into the conventional 2D NMR scheme.

In UF2DNMR spectroscopy, one deals with a single transient, and a meaningful comparison would compare the SNR *per scan*, i.e., setting $N_1 = 1$ in Eq. (58). According to Eq. (47), the maximum amplitude of an echo is $M_0 L$. Hence, for the indirect spectrum the signal to noise is:

$$\mathrm{SNR}_{\mathrm{echo}} = \frac{LM_0}{n_{\mathrm{rms}}}. \tag{59}$$

Fourier transforming UF2DNMR data along the t_2-axis increases the SNR by a factor of $\sqrt{N_2}$, where N_2 is the resolution along the direct domain and is equal to the number of gradient repetitions in the EPSI sequence. This is analogous to the Fourier transform taken along the t_2-axis in the conventional 2D case, and the resulting SNR is:

$$\mathrm{SNR}_{\mathrm{UF}} = \frac{\sqrt{N_2} LM_0}{n_{\mathrm{rms}}}. \tag{60}$$

Comparing Eqs. (58) and (60) suggests that, on a *per scan* basis,

$$\frac{\mathrm{SNR}_{2D}}{\mathrm{SNR}_{\mathrm{UF}}} = \frac{n_{\mathrm{rms}}^{\mathrm{UF}}}{n_{\mathrm{rms}}^{2D}}. \tag{61}$$

Still, it is erroneous to conclude that the noise levels are identical in both cases. In the conventional experiment, the highest frequencies of interest are those present in the spectral width along the direct axis, SW_2, to which the filter bandwidth, fbw^{2D}, is set. In contrast, in UF2DNMR one acquires echoes given by Eq. (47) spanning a frequency range of $\sim \gamma G_a L$ (Fig. 21). The corresponding fbw^{UF} must therefore be set to at least $\gamma G_a L$, to ensure the echoes do not distort. From Table 1, we have $\gamma G_a L = \frac{\gamma G_a T_a L}{T_a} = 2N_1 \mathrm{SW}_2$, and thus:

$$\frac{\mathrm{SNR}_{2D}}{\mathrm{SNR}_{\mathrm{UF}}} = \sqrt{\frac{\mathrm{fbw}^{\mathrm{UF}}}{\mathrm{fbw}^{2D}}} = \sqrt{2N_1}. \tag{62}$$

where in essence N_1 is the number of spectral elements in the single-scan experiment along the indirect-domain. Eq. (62) indicates that, *per scan*, UF2DNMR suffers a $\sim \sqrt{N_1}$ penalty in its SNR vis-a-vis conventional NMR. *This is arguably UF2DNMR's main handicap, and emphasizes that these methods will work best when applied to problems where sensitivity is not a defining concern.*

[17] A symmetric definition of the discrete Fourier transform is employed: $\hat{s}_k = \frac{1}{\sqrt{N}} \sum_{j=1}^{N} s_j e^{\frac{2\pi ijk}{N}}$, which implies $s_j = \frac{1}{\sqrt{N}} \sum_{k=1}^{N} \hat{s}_j e^{-\frac{2\pi ijk}{N}}$.

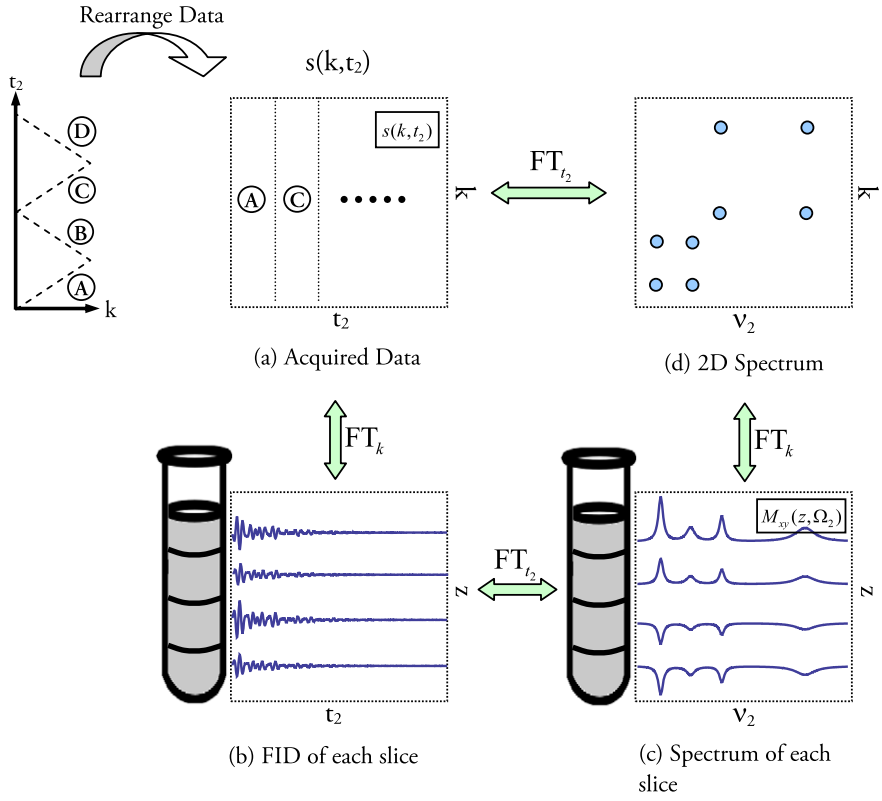

Fig. 20. A schematic view of EPSI (note the axes have been tilted by 90° to facilitate the display of information). Once the acquired data has been arranged in a matrix (a), it can be Fourier transformed about the k-axis to yield the FID from each slice (b). A second Fourier transform recovers the spectrum from each slice (c), and a third – the 2D spectrum. Alternatively, a single Fourier transform over the t_2 axis can be used to obtain the 2D spectrum directly (d).

Table 3
Single-scan spatial-spectral acquisition: parameter relations.

To set …		Set		… to
SW_2	The direct domain's spectral width	T_a	The duration of the acquisition gradient's lobe	$\frac{1}{2SW_2}$
$\Delta\nu_2$	The spectral resolution along the direct domain	N_2	The number of oscillations of the acquisition gradient	$\frac{1}{2T_a\Delta\nu_2}$
SW_1	The indirect domain's spectral width	G_a	The acquisition gradient	$\frac{CSW_1}{\gamma T_a}$
$\Delta\nu_1$	The spectral resolution along the indirect domain	$t^1_{max} = CL$	The effective encoding time (see Eqs. (34), (39), (36))	$\frac{1}{\Delta\nu_1}$

3.3.5. A formal view of EPSI

We have previously emphasized the use of oscillating acquisition gradients to acquire spatial-spectral information independently and simultaneously from different slices in the sample. It is interesting to reformulate this acquisition block at an even more fundamental level than that presented in the previous sections; one which highlights its general applicability, in agreement with the parallelization principle laid out at the beginning of this work.

Spins precessing in the transverse plane with a chemical shift Ω_2 and position z before commencing acquisition will, when subjected to the EPSI module in Fig. 15, give rise to a signal of the form:

$$s(k,t_2) \propto e^{\imath(k(t_2)z+\Omega_2 t_2)}. \tag{63}$$

In order to describe a spatially-encoded sample, a generic distribution in the $\hat{x}\hat{y}$-plane as a function of position and chemical shift, $I(z,\Omega_2)$, must be taken into account. $I(z,\Omega_2)$ is proportional to $M_+(z,\Omega_2)$, and so:

$$\begin{aligned} s_{\text{ensemble}}(k,t_2) &\propto \int dz \int d\Omega_2 M_+(z,\Omega_2) s_{\text{single}}(k,t_2) \\ &= \int dz \int d\Omega_2 M_+(z,\Omega_2) e^{\imath k(t_2)z} e^{\imath\Omega_2 t_2}. \end{aligned} \tag{64}$$

The signal, acquired in $k-t_2$ space, is seen to be the Fourier-conjugate of $M_+(z,\Omega_2)$; that is, Fourier transforming the signal $s(k,t_2)$ along its two variables will yield $M_+(z,\Omega_2)$. In actuality, $s_{\text{ensemble}}(k,t_2)$ is a discrete data set sampled at only specific points in the $k-t_2$ plane, and as such it is subject to all the constraints encountered when sampling a function. Furthermore, to avoid non-regular sampling intervals, one can choose just those points acquired during the positive (or negative) gradient lobes, as was shown in Fig. 17c. It follows from this that $M_+(z_0,\Omega_2)$, for a fixed z_0, represents the spectral distribution of spins in the slice whose position is z_0. Carrying out a Fourier transform over Ω_2 would then naturally deliver the free induction decay for each z_0 slice. This reasoning is illustrated in the bottom panel of Fig. 20.

This general understanding of EPSI can also be used to deduce why a single Fourier transform over the t_2 variable is needed to recover a 2D spectrum in a UF2DNMR experiment. In conventional spectroscopy, one executes several experiments, varying the delay along the indirect t_1 domain between each experiment; data is then acquired along the direct t_2 axis. Consequently, one needs to Fourier transform the resulting 2D data set along both axes, t_1 and t_2, to recover the 2D NMR spectrum. UF2DNMR works by parallelizing this notion, replacing the t_1 domain by the z-axis. One can, by Fourier transforming the EPSI-acquired data over the

k variable, recover the FID of each experiment. This data set, in the $z - t_2$ plane, is analogous to the data set conventionally acquired in the $t_1 - t_2$ plane (Fig. 20b). It remains to Fourier transform this set against its two variables – z and t_2 – to recover the 2D spectrum, as shown in Fig. 20d. This is equivalent to a single Fourier transformation of $s(k, t_2)$ along the original t_2 axis.

It is clear from the above discussion that the $z - \nu_2$ plane is Fourier paired to the $k - t_2$ plane, and as such, the range and resolution viewable along the z, ν_2 axes is determined by the familiar Nyquist sampling relations. Still, as already mentioned, a distinction should be drawn between the direct ν_2 domain, whose resolution depends solely on the acquisition parameters T_a and N_2, and an indirect ν_1 domain, whose resolution depends on the particular form of spatial encoding used during t_1. Indeed, in ultrafast 2D NMR, where spins are assigned a z-dependent t_1 evolution, the particular form of $t_1 = t_1(z) = Cz$ will in turn define the k/ν_1 characteristics for each encoding scheme (Fig. 13). Given C and the sample size L, the EPSI-described Nyquist sampling relations can thus be used to compute the desired spectral characteristics as a function of the experimental parameters. These results are summarized for convenience in Table 3.

3.3.6. Examples

With the theory underlying UF2DNMR outlined, this section summarizes illustrative examples of spectra acquired using it. Fig. 22 demonstrates the viability of UF2DNMR on an ^{15}N ubiquitin sample, comparing the resulting HSQC spectrum to one acquired using conventional 2D spectroscopy. It is seen that all essential features are retained in the single-scan version. As discussed in Section 3.3.3, phasing issues arise in UF2DNMR; for this reason, the absolute magnitude of ultrafast spectra (instead of the real part) is usually used in those biomolecular applications. This leads to impaired resolution along both axes by a factor of $\sqrt{3}$. Still, Fig. 23 demonstrates the ability of UF2DNMR to acquire spectra spaced at under a second, and utilize them to monitor a chemical process in real-time [43].

Fig. 24 shows how, by suitably altering the spatial encoding protocol, various interactions can be suppressed and others allowed to evolve along the indirect domain [33]; specifically, the chemical shift evolution during encoding was refocused, while the J-coupling was allowed to evolve. This was achieved by phase-modulating the spins (see Section 3.1.2), equating the gradients of both chirps while applying the $\frac{\pi}{2}$ pulse for twice as long as the π-chirp. The resulting spatio-temporal coefficient C then becomes null, voiding any chemical shift evolution along that axis, while allowing for the J-coupling – unaffected by the π-pulse – to continue evolving.

Recent advances have also been made in applying UF2DNMR in conjunction with modern hyperpolarization methods [44,45]. The signal from the hyperpolarized nuclei, while large, decays rapidly with a time constant T_1, the magnitude of which is governed by spin-lattice relaxation and is on the order of a second. Since hyperpolarizing a sample may take hours, a full 2D spectrum may take days to complete. The single-scan, sub-second nature of UF2DNMR becomes particularly appealing in making the best use of this enhanced signal. Several results are displayed in Fig. 25.

4. Spatial-spectral single-scan spectroscopy

The parallelization lying at the heart of UF2DNMR is made possible by the use of chirped RF pulses, that excite spins onto the transverse plane and endow them with a phase $\phi(z, \nu) = C\nu z$. Such manipulation can be viewed as part of a larger superset of *spatial-spectral* pulses, which allow one to excite an arbitrary phase pattern in a position-frequency $(z - \nu)$ 2D space [46,47]. This section discusses how, by generalizing these reasonings (Fig. 26), the concept of parallelization can be extended to paradigms other than the single-scan UF2DNMR experiments just described. We begin this discussion on extending the UF2DNMR paradigm by focusing on Hadamard spectroscopy [48–52].

4.1. Conventional Hadamard spectroscopy: a review

In a standard 2D NMR experiment, one applies a mixing sequence which transfers magnetization between sites based on particular interactions that exist between them (Fig. 27a). Since many frequencies are present in the sample prior to mixing, the basic experiment must be repeated for many t_1 values: at least $N_1 = \mathrm{SW}_1/\Delta\nu_1$, to properly resolve all sites over a bandwidth SW_1 with a minimal resolution $\Delta\nu_1$. These experimental results are then arranged in a 2D matrix and Fourier transformed over both axes, yielding a 2D spectrum in the ν_1, ν_2 domain.

As N_1 will be given by local spectral characteristics – e.g., the closest two peaks defining $\Delta\nu_1$ and the farthest SW_1, regardless of where the remaining sites appear – one can envision a simple alternative to this completely general scheme: instead of exciting all chemical sites simultaneously and monitoring their time-domain evolution, one could use a selective soft pulse to excite each particular chemical site, ν_a, as depicted in Fig. 27b. This would entail knowledge of the 1D spectrum prior to the 2D experiment, as

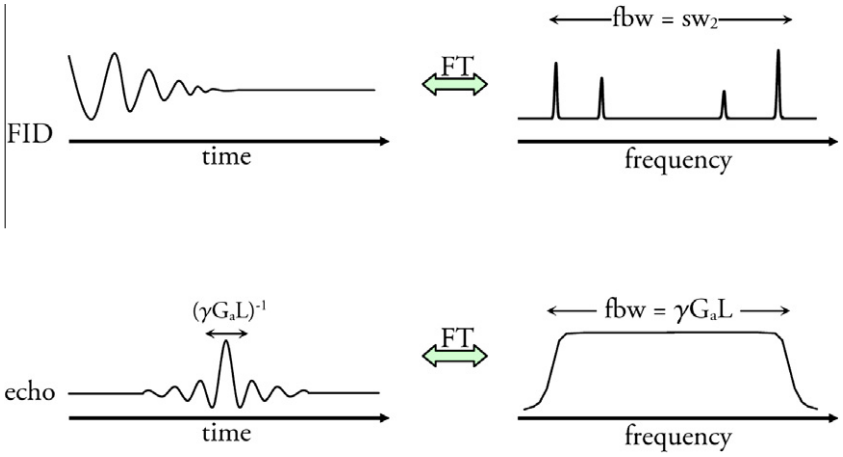

Fig. 21. Filter bandwidth settings in conventional 2D versus single-scan ultrafast spectroscopies.

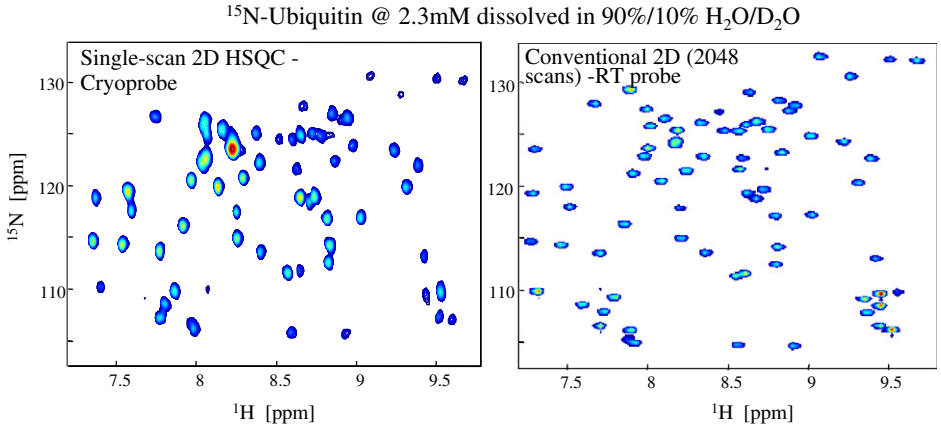

Fig. 22. A comparison between UF2DNMR and conventional 2D HSQC NMR spectra recorded at 18.8 T on a 3.25 mM ^{15}N-enriched ubiquitin sample dissolved in 90/10% H_2O/D_2O (courtesy of Dr. Maayan Gal, Weizmann Institute).

one would have to know which frequency to irradiate. But since this scheme allows one to investigate only those lines of the 2D spectrum that are of interest, one could dramatically reduce the number of experiments required for cases where both large bandwidths *and* high spectral resolutions are needed, thus speeding up the 2D acquisition. Indeed, in these selective-excitation experiments the t_2 domain would include only frequencies originating from ν_a prior to mixing. Fourier transforming this data would yield the $\nu_1 = \nu_a$ line from the full 2D spectrum. Each selective-excitation experiment then yields a particular ν_1 line of the full 2D spectrum. This approach liberates one from the need to discretely sample the t_1 axis with a fine enough resolution: the resolution along the ν_1 axis will be determined only by the width of the soft excitation pulse, which is inversely proportional to its duration.

The above scheme suffers from a signal-to-noise penalty, in the sense that in each iteration only a single peak is excited. Contrast this with conventional 2D spectroscopy, in which all peaks are excited simultaneously. It is possible to find a solution to this drawback [50], by exciting all peaks of interest simultaneously but with different phases. This approach relies on a mathematical construct named Hadamard matrices [53] – hence the method, illustrated in Fig. 27c, is referred to as 2D Hadamard NMR.

A Hadamard matrix H of order N is an $N \times N$ construct that satisfies $HH^T = NI$, where I is the identity matrix. The *Hadamard Conjecture* [54] states that Hadamard matrices of order $4k$ exist for all positive integers k. Hadamard matrices of orders 2 and 4 are:

$$H_2 = \begin{pmatrix} 1 & 1 \\ 1 & -1 \end{pmatrix}, \; H_4 = \begin{pmatrix} 1 & 1 & 1 & 1 \\ 1 & -1 & 1 & -1 \\ 1 & 1 & -1 & -1 \\ 1 & -1 & -1 & 1 \end{pmatrix}, \tag{65}$$

2D Hadamard spectroscopy's approach is best illustrated via an example. Suppose there are four frequencies of interest, $\nu_a, \nu_b, \nu_c, \nu_d$, along the ν_1 axis. Four experiments are then carried out; in the kth experiment, all four peaks are excited, each peak with a phase of either 0 or π, in a pattern that corresponds to the kth row in the Hadamard matrix (Fig. 28a). The resulting four FIDs are then subtracted and added from each other in a pattern that once again follows the rows of the Hadamard matrix (Fig. 28b). The output of this is four 1D data sets, with the kth data set equivalent to the FID collected from an experiment in which a single frequency ν_k has been selectively excited, *but with a* $\sqrt{4}$ *increase in signal to noise*. This increase stems from the four experiments, which were added in such a way that one peak gets constructively boosted, while all other peaks add destructively to zero.[18] As signal averaging four t_1 increments could also give this sensitivity improvement, the multiplex advantage has been reinstated.

4.1.1. Complex Hadamard matrices

Although Hadamard matrices exist only for orders $N = 2$ and $N = 4k$ where k is an integer, it is possible to extend the ideas discussed in this section to any integer N by considering complex Hadamard matrices [56], which are defined by $H^{(c)}_{p,q} = e^{\frac{2\pi\imath(p-1)(q-1)}{N}}$, $p, q = 1, 2, \ldots, N$. Like the real Hadamard matrices in Eq. (65), these satisfy $H^{(c)}(H^{(c)})^\dagger = NI$, which is the essential characteristic needed by Hadamard spectroscopy. The complex Hadamard matrices of orders 2, 3 and 4 are:

$$H^{(c)}_2 = \begin{pmatrix} 1 & 1 \\ 1 & -1 \end{pmatrix}, \; H^{(c)}_3 = \begin{pmatrix} 1 & 1 & 1 \\ 1 & e^{\frac{2\pi\imath}{3}} & e^{-\frac{2\pi\imath}{3}} \\ 1 & e^{-\frac{2\pi\imath}{3}} & e^{\frac{2\pi\imath}{3}} \end{pmatrix}, \; H^{(c)}_4 = \begin{pmatrix} 1 & 1 & 1 & 1 \\ 1 & \imath & -1 & -\imath \\ 1 & -1 & 1 & -1 \\ 1 & -\imath & -1 & \imath \end{pmatrix}. \tag{66}$$

It is seen that, even for $N = 4$, the real and complex Hadamard matrices differ. When translated into NMR terms (for the $N = 4$ case), this means that, while the first experiment would excite all four peaks with zero phase, the second would excite them with phases equal to $0, \frac{\pi}{2}, \pi, \frac{3\pi}{2}$, respectively. Contrast this with an equivalent experiment using real Hadamard matrices, for which the pulse phases for each peak would be set to $0, \pi, 0, \pi$. Despite these differences, the arguments above can be repeated using complex Hadamard matrices, resulting in the same increase in signal to noise. In this case, the spectra must be added using the same phase coefficients used to excite them–effectively, a sort of discrete Fourier transform.

Note that, while real Hadamard matrices require the selective excitation to be real – that is to place the excited spins either along $\hat{x}$ or $-\hat{x}$ in the Bloch sphere – their complex analogs require the spins to be evenly distributed in the $\hat{x}\hat{y}$ plane of the Bloch sphere, a condition which may be more difficult to achieve experimentally and to post-process.

4.2. Single-scan Hadamard spectroscopy

Parallelizing 2D Hadamard spectroscopy requires a sequence which will simultaneously excite all spectral patterns as shown in Fig. 28a, but will also place them in different spatial positions along the sample as shown in Fig. 29. With such a pattern encoded,

[18] Signal-averaging N experiments increases the signal-to-noise ratio by a factor of $\sqrt{N}$ [55].

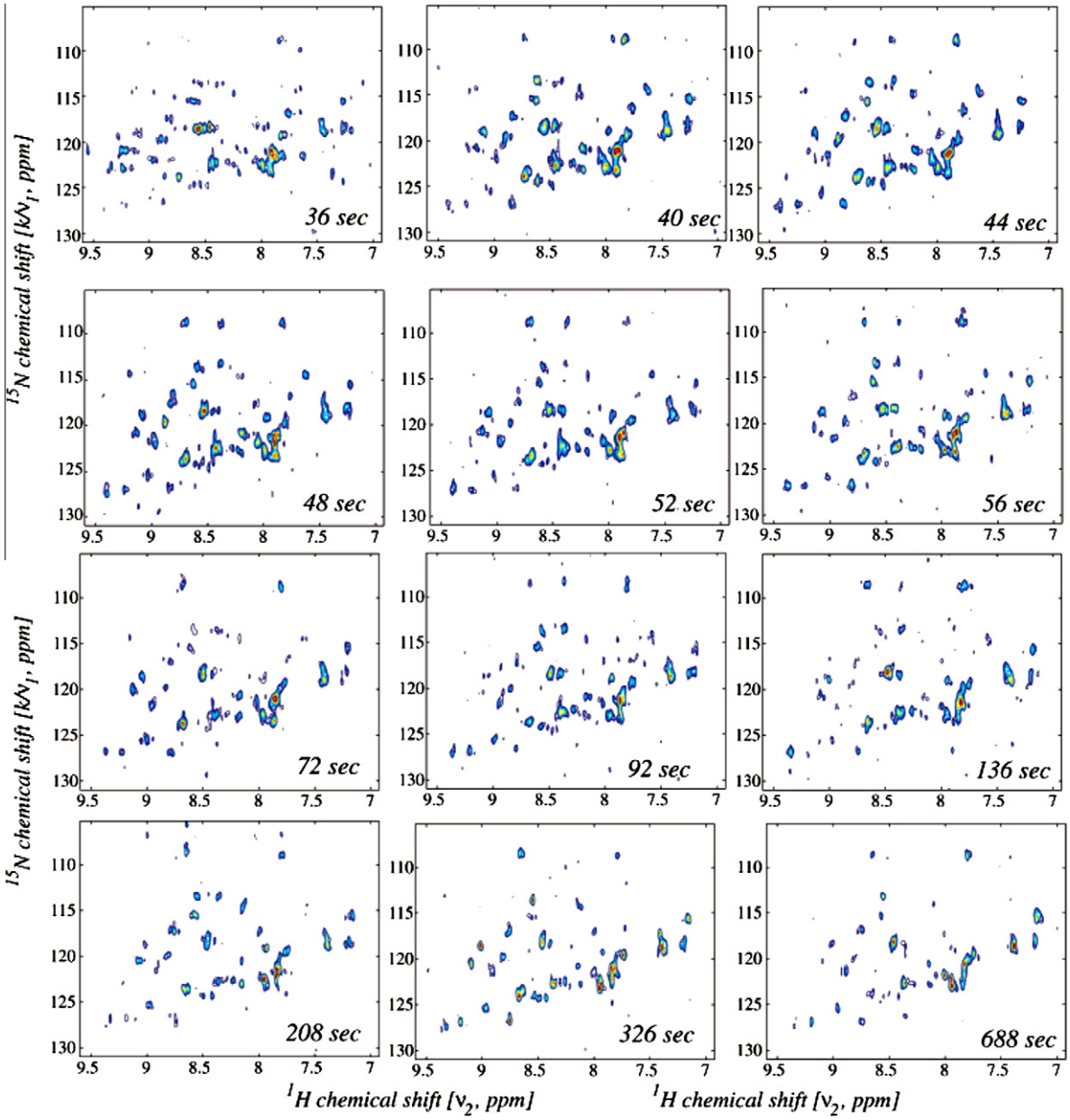

Fig. 23. Representative series of real-time 2D HSQC NMR spectra recorded on a ~3.2 mM ubiquitin solution, following the dissolution of an initially fully protonated lyophilized powder onto a D_2O-based 50 mM phosphate buffer. The times indicated in each frame correspond to the approximate delay elapsed since the powder was initially dissolved (something which happened outside the magnet) and the average time of the data acquisition. In the actual experiment a full series of spectra separated by ca. 4 s were recorded over a 20 min interval; only a subset of these spectra is shown [43].

the mixing sequence – which will affect all sites simultaneously – can be applied. Collecting an FID from each slice and Fourier transforming it using a *spatial-spectral* acquisition sequence, could then provide all the information being sought in a single-scan. The acquisition block demanded by this is, as discussed in Section 3.2, furnished by Echo Planar Spectroscopic Imaging (EPSI). A 2D Fourier transform will have to be applied to the resulting EPSI data set in order to recover the pattern in Fig. 29b. Once this is achieved, one can proceed as with conventional Hadamard spectroscopy, viz, add and subtract the spectra in accordance with a Hadamard matrix, as shown in, e.g., Fig. 28b. The main "trick" in this single-scan 2D Hadamard implementation is the use of *spatial-spectral pulses* capable of encoding the different Hadamard patterns of Fig. 29. Two 2D NMR sequences implemented in such a manner – one for homonuclear spectroscopy and the other for HSQC – are displayed in Figs. 30 and 32, with the corresponding excitation and acquisition blocks highlighted. It is illustrative to outline these Hadamard NMR experiments assuming only two chemical sites of interest (Fig. 31). Notice that, although both excitation and acquisition take place in a position-frequency plane, their frequency axes differ: when the peaks are excited, it is along an indirect, pre-mixing domain; when the signal is acquired, its spectral contents are those present after mixing, and hence the frequency axis corresponds to the direct domain. The precise values of N_1, G_e, N_2, G_a, T_a will depend on the desired spectral characteristics, and in particular, on the spectral widths SW_j and line widths $\Delta\nu_j$ along the direct $(\nu = 1)$ and indirect $(j = 2)$ domains. Care must be taken when discussing the indirect domain: unlike a conventional experiment, Hadamard spectroscopy preselects a small number N_{peaks} of peaks along the indirect domain to be investigated, and thus the regular Nyquist relations do not hold for that axis. Indeed, the resolving power along the indirect ν_1 axis is deter-

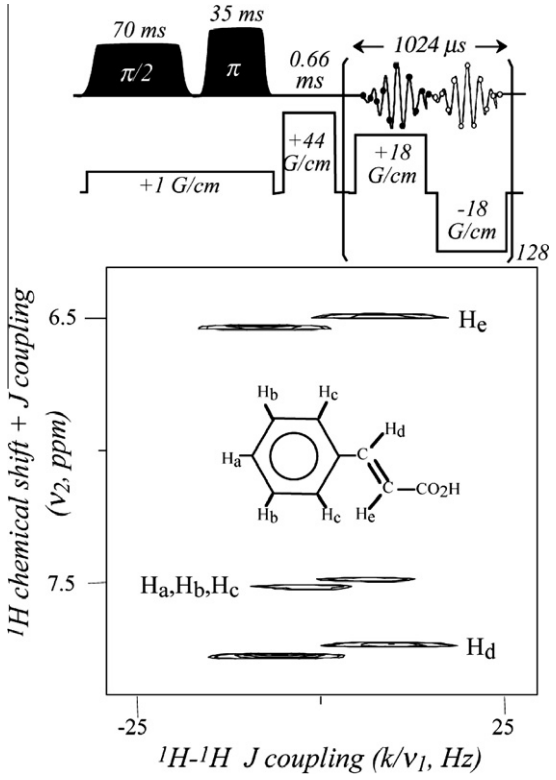

Fig. 24. (Top) Pulse sequence capable of affording a single-scan 2D *J*-resolved NMR spectrum, utilizing a continuous $\frac{\pi}{2}$–π phase encoding of the homonuclear coupling along the indirect domain. (Bottom) Results illustrating the pulse sequences performance on a cinnamic acid/DMSO-d_6 solution, acquired with the various indicated parameters. Other setup and processing parameters of the single-scan data were akin to those in Fig. 14; notice the clearly discernible *J*-patterns for the various chemically inequivalent sites in the molecule. (from [33].)

mined by the selectivity of the excitation pulse – that is, by its ability to excite selectively the desired peaks, the width $\Delta\nu_1$ of which is given by $\frac{1}{2N\Delta t}$. This $\Delta\nu_1$ is assumed here the width of a typical peak, ideally set to the order of magnitude of $\frac{1}{T_2}$, although it may be set to be larger so long as no neighboring peaks are affected.

The spatial-spectral encoding effected during excitation must also be taken into account during acquisition. The same spatial resolution must be used, which constrains the EPSI parameters G_a, T_a to be $(k_{\max}^{(a)})^{-1} = (\gamma G_a T_a)^{-1} = \Delta z$, and $(\delta k^{(a)})^{-1} = (\gamma G_a \delta t)^{-1} = L$, where δt is the physical dwell time of the receiver during acquisition.[19] The spectral axis, whose resolution and spectral width are given by $\frac{1}{2N_2T_a}$ and $\frac{1}{2T_a}$, respectively, can be set arbitrarily to the desired resolution requirements along the direct ν_2 domain. These parameter relations are summarized in Table 4 (see also Appendix A).

4.3. Signal-to-noise considerations

Although single-scan Hadamard NMR condenses a 2D conventional spectroscopic experiment, this offers no speed up compared to UF2DNMR, which is single-scan as well. Instead, this section argues that single-scan Hadamard spectroscopy offers an improvement in signal to noise over single-scan UF2DNMR by a factor of $\sqrt{\frac{N_{\text{peaks}}}{N_1}}$, where N_1 is the number of points along the indirect domain sampled by the ultrafast protocol. Thus, much like in the conventional multi-scan case, single-scan Hadamard spectroscopy's advantage is greatest for sparse spectra, or for spectra for which one is mainly interested in a small number of selected peaks.

The single-scan Hadamard EPSI acquisition protocol retrieves a 1D spectrum from each site/slice of interest. Results have been previously derived for the SNR of a 1D experiment carried out on an entire sample, acquiring N points (Eq. (57)). In the current case, experiments are carried out for each of the N_{peaks} peaks of interest, and hence SNR must be $\sqrt{N_{\text{peaks}}}$ times smaller than in a conventional 1D acquisition. This can be proved without an analytical calculation, by the following argument. Consider the simplest 1D experiment, consisting of a hard-pulse followed by acquisition, and denote the SNR of its spectrum by X. Next, consider the same experiment, this time using EPSI to acquire the signal (assuming the same filter-bandwidth has been set in both cases). After Fourier transforming over the k and t_2 variables, one recovers the FID as a function of position (see Fig. 20c). The SNR of each slice's spectrum is denoted by X' (each being identical to the next, apart from the random, uncorrelated noise) and it is assumed that there are N_{slices} such slices. It is well known [55] that adding the results of N different experiments increases the SNR by a factor of $\sqrt{N}$. The overall SNR must be the same whether a single FID is collected, or whether the FIDs of N_{slices} are collected and then added together. Hence X must equal $\sqrt{N_{\text{slices}}}X'$.

The spectrum from each slice is added and subtracted in the single-scan 2D experiments, according to the corresponding $N_{\text{peaks}} \times N_{\text{peaks}}$ Hadamard matrix (Fig. 31). This enhances each peak by a factor of N_{peaks}. Noise gets added as well, albeit incoherently, and hence its rms increases as $\sqrt{N_{\text{peaks}}}$. The overall improvement in SNR due to the Hadamard post-processing is, therefore, $\frac{N_{\text{peaks}}}{\sqrt{N_{\text{peaks}}}} = \sqrt{N_{\text{peaks}}}$. The resulting SNR, vis-a-vis that of a conventional 1D acquisition, is:

$$\text{SNR}_{\text{HAD}} = \frac{\sqrt{N_{\text{peaks}}} L M_0}{n_{\text{rms}}}. \tag{67}$$

A comparison to the ultrafast case yields:

$$\frac{\text{SNR}_{\text{HAD}}}{\text{SNR}_{\text{UF}}} = \frac{n_{\text{rms}}^{(\text{UF})}}{n_{\text{rms}}^{(\text{HAD})}} = \sqrt{\frac{\text{fbw}^{(\text{UF})}}{\text{fbw}^{(\text{HAD})}}}. \tag{68}$$

It is the filter bandwidths that differ between the two experiments. Whereas UF2DNMR partitions the sample into N_1 slices, Hadamard spectroscopy partitions it into N_{peaks} slices. All other things being equal, the ratio of the corresponding EPSI acquisition gradients is therefore $\frac{N_1}{N_{\text{peaks}}}$, and so:

$$\frac{\text{SNR}_{\text{HAD}}}{\text{SNR}_{\text{UF}}} = \sqrt{\frac{N_1}{N_{\text{peaks}}}}. \tag{69}$$

This increase in the SNR is illustrated experimentally in Fig. 32, which compares single-scan 2D TOCSY ^{1}H NMR experiments on a sample containing *L*-tyrosine, using ultrafast and Hadamard encodings.

4.4. The general case of spatial-spectral single-scan 2D NMR

The UF2DNMR excitation schemes proposed in Section 3 do not assume any prior knowledge of the given distribution of chemical shifts. However, in the event that the 1D spectrum of a sample is known already and one is interested in studying the interactions between spins via 2D NMR, we have just shown that significant SNR gains can be made when dealing with sparse spectra by using single-scan Hadamard spectroscopy. UF2DNMR excitation schemes can be generalized to exploit this prior knowledge by incorporating suitably designed spatial-spectral pulses [57]. This modification will, as explained below, lead to an increase in the

[19] In practice, the actual value of δt is set somewhat smaller to allow for smooth variations in the spin density between slices (due to non-ideal excitation) which might get otherwise smeared. Fortunately, the magnitudes involved are easily achieved on modern hardware.

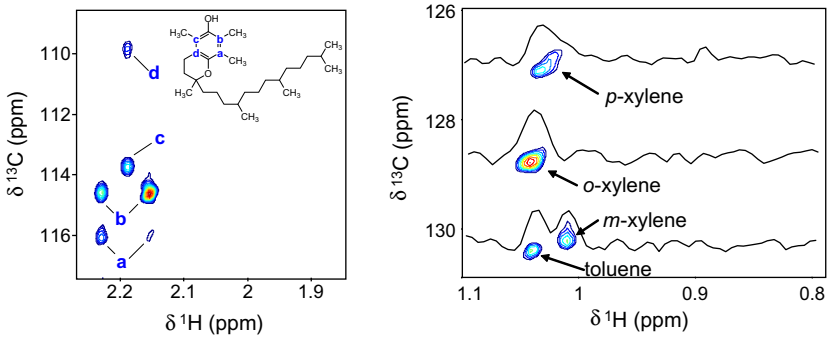

Fig. 25. Left: partial UF2DNMR HMBC spectrum of hyperpolarized vitamin E recorded at 12 mM concentration. Right: UF2DNMR HMBC of a 1:1:1:1 mix of natural abundance toluene/xylenes dissolved in CH_3OH, at 0.1 mM. Hyperpolarization took 90 min (Patrick Giraudeau and Lucio Frydman, unpublished).

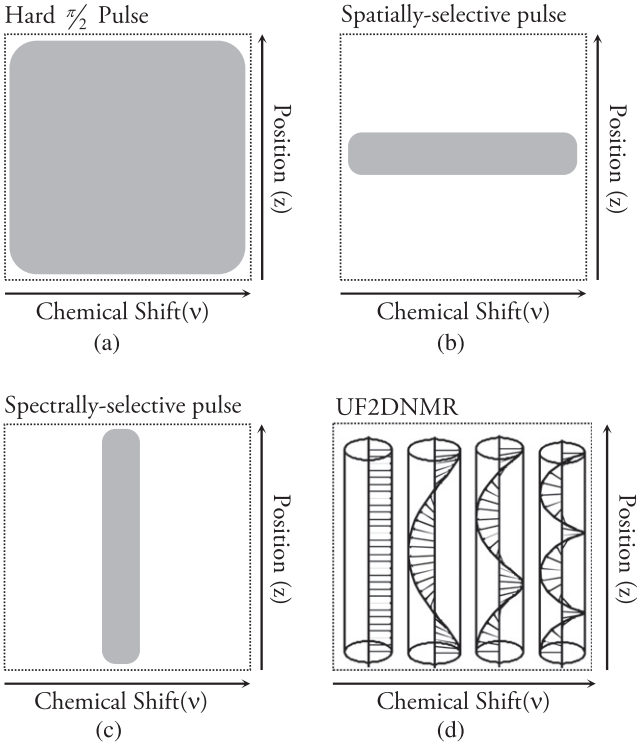

Fig. 26. Different excitation/encoding modes in the spatial-spectral $(z-\nu)$ plane. (a) A hard-pulse, exciting all spins in the sample, irrespective of their positions and chemical shifts. (b) Spatially selective pulses, of the kind often used in imaging to excite spins in a selected spatial region, regardless of their chemical shift. (c) Spectrally selective pulses, used to excite a particular chemical site in the sample, as is often done in NMR (for example, for water suppression). (d) UF2DNMR spatial-encoding approach, relying on chirped RF pulses and oscillating gradients, to impart the sample with a position and chemical-shift dependent phase, $\phi(z,\nu) = Cz\nu$. This is visualized schematically as windings of increasing helicity as ν increases.

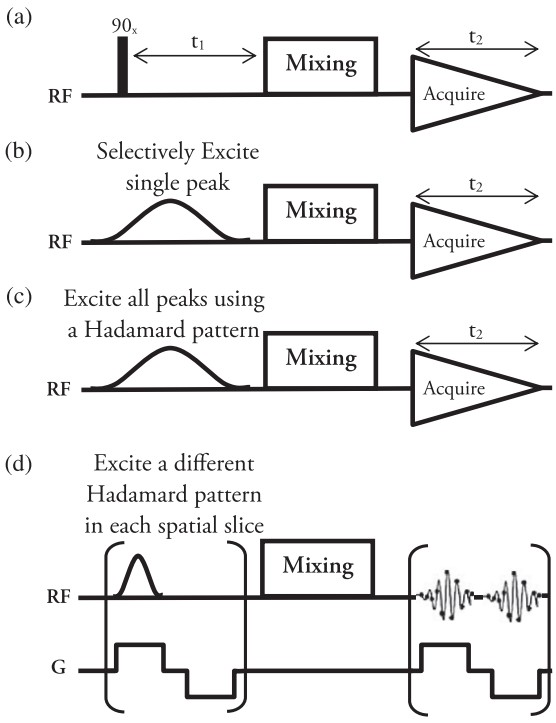

Fig. 27. Train-of-thought leading from conventional 2D NMR to single scan 2D Hadamard spectroscopy. (a) Outline of a standard 2D NMR experiment: all frequencies are excited, and the basic experiment is repeated many times while varying t_1, so as to be able to distinguish between the frequency content of the spectrum prior to mixing. (b) Using a spectrally-selective pulse, a single peak is excited and monitored during acquisition. The basic scheme needs to be repeated for all frequencies of interest along the indirect ν_1 domain. This can save acquisition time, but it entails knowledge of the 1D spectrum prior to commencement, and is devoid of Fellgett's multiplexing advantage, resulting in inferior SNR per unit time compared to conventional 2D NMR. (c) These SNR limitations can be overcome by exciting all frequencies of interest simultaneously with different phases according to a Hadamard matrix, allowing for the reconstruction of the original spectrum (see Fig. 28). (d) By incorporating an alternating excitation gradient, the spectrally-selective pulses of panel (c) can be made spatially-selective as well, making it possible to encode a different Hadamard experiment into each slice of the sample. The results of each experiment can be probed spatial-spectrally using the acquisition schemes discussed in Section 3.2.

signal-to-noise ratio of the resulting 2D spectrum, while retaining the single-scan nature of the acquisition.

The main idea behind this generalization is outlined in Fig. 33. In conventional UF2DNMR, spins are excited and imbued with a helical winding (Fig. 26), the tightness of the winding being proportional to their chemical shift: $\phi(z,\nu) = C\nu z$. As a result of this, gradient echoes can be acquired along the direct domain and, when plotted as a function of $k = \gamma G_a t$, will be spaced in proportion to their spectral distance: $\Delta k = C\Delta\nu$. For a sparse spectrum, this can result in regions with no echoes, the acquisition of which wastes time and leads to sub-optimal SNR while placing stricter demands on the hardware. However, with an *a-priori* knowledge of the chemical shifts $\Omega_1, \Omega_2, \ldots, \Omega_j, \ldots, \Omega_N$ present along ν_1, the chemical shifts being targeted can be instilled with windings proportional not to ν but to the chemical shift's index j (see Fig. 33). For example:

$$\Omega_1 \leftrightarrow \phi(z) = Cz\Delta\nu$$
$$\Omega_2 \leftrightarrow \phi(z) = 2Cz\Delta\nu$$
$$\Omega_3 \leftrightarrow \phi(z) = 3Cz\Delta\nu$$
$$\ldots$$
$$\Omega_N \leftrightarrow \phi(z) = NCz\Delta\nu.$$

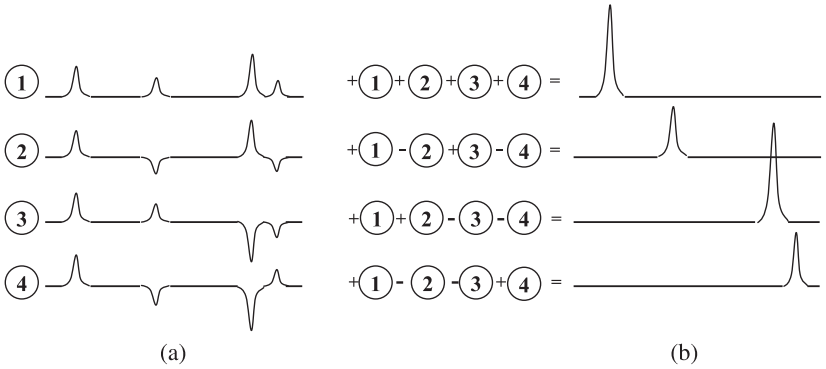

Fig. 28. Conventional Hadamard spectroscopy, illustrated for the case of four peaks of interest. (a) The peaks are excited with different phases, given by a 4×4 Hadamard matrix (see Eq. (65)). The resulting FIDs are then added and subtracted as shown in (b) to single out a specific peak. For example, adding up FIDs #1 and #3 and subtracting from these FIDs #2 and #4 results in an FID identical to that resulting from an experiment in which peak #2 was excited alone, but with a 4-fold increase in signal level.

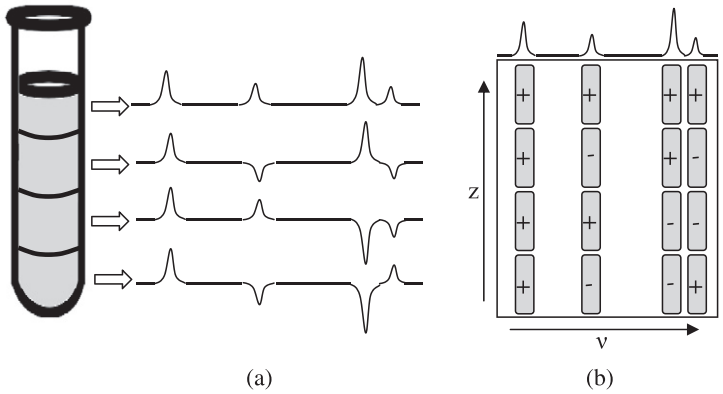

Fig. 29. The single-scan Hadamard paradigm for the case of four peaks of interest. (a) The sample is partitioned into slices, and a different Hadamard pattern is encoded into each slice using a spatial-spectral pulse, as detailed in the text. (b) The same result as (a), viewed in the frequency-position plane. Note that, while the slices are equidistant, the excited frequencies can be arbitrarily chosen.

This will result in an equispaced echo pattern along the indirect-domain's k-axis, at positions $k_j = jC\Delta\nu$. $\Delta\nu$ is once again a user-defined constant, chosen such that the echoes don't overlap; that is, so that $C\Delta\nu = \Delta k_{min} \geqslant \frac{1}{L}$, where $\frac{1}{L}$ is the width of the echo when viewed as a function of k. The effect of such a modified winding pattern is to bring the echoes closer together – in fact, to bring them as close as possible without having them overlap. This, in turn, allows one to either reduce the time needed to collect the echo train, or – equivalently – reduce the magnitude of the acquisition gradient. This, in turn, decreases the filter bandwidth, increasing the SNR of the resulting UF2DNMR spectrum. Much like in single-scan Hadamard spectroscopy, the gain in SNR depends on the sparsity of the echoes (see Section 4.3): if N_1 is the number of points along an indirect domain sampled by conventional UF2DNMR, and N_{peaks} is the number of echoes present, the ratio of gradients employed (assuming identical acquisition times) will be:

$$\frac{G_a^{(\text{Conventional UF2DNMR})}}{G_a^{(\text{Spatial-spectral UF2DNMR})}} = \frac{N_1}{N_{\text{peaks}}}. \tag{70}$$

The ratio of the respective filter bandwidths will be given by the square root of Eq. (70), leading to a gain in SNR that is given by the ratio:

$$\frac{SNR^{(\text{Conventional UF2DNMR})}}{SNR^{(\text{Spatial-spectral UF2DNMR})}} = \sqrt{\frac{N_1}{N_{\text{peaks}}}}. \tag{71}$$

Alternatively, one can choose to utilize spatial-spectral encoding to increase the resolution along the indirect domain. While in conventional UF2DNMR the spacing between the echoes along the k-axis is proportional to their winding, which is in turn proportional to the encoding time t_1^{max}, the spacing in spatial-spectral encoding is fixed by the spatial-spectral excitation scheme. In conventional UF2DNMR, increasing the encoding times to increase the spacing (and hence the resolution along the indirect domain) entails a similar increase in the acquisition gradient, which may be limited by the hardware. On the other hand, using spatial-spectral encoding, the spacing between the peaks is kept constant, allowing one to increase the encoding time while simultaneously decreasing the acquisition gradient. Fig. 34 exemplifies this feature with a homonuclear 2D TOCSY example.

The generation of arbitrary spatial-spectral patterns underlying both this and the Hadamard approaches is further discussed in the Appendices.

5. Single-scan nD spatially-encoded imaging (SPEN MRI)

As mentioned in the introduction, NMR has become an important tool in medicine following the introduction of Magnetic Resonance Imaging (MRI) ([4–6]). While originally used to obtain maps of the spin density $\rho_0(\mathbf{r})$, modern day MRI allows one to spatially map almost every quantity of interest measurable in NMR, including transverse (T_2) and longitudinal (T_1) relaxation times, temperature, diffusivity and pH. All of those provide substantial biochemical and clinical contrast, with high spatial resolution, and with a minimum of invasive procedures compared to other medical imaging tools. The basic objective

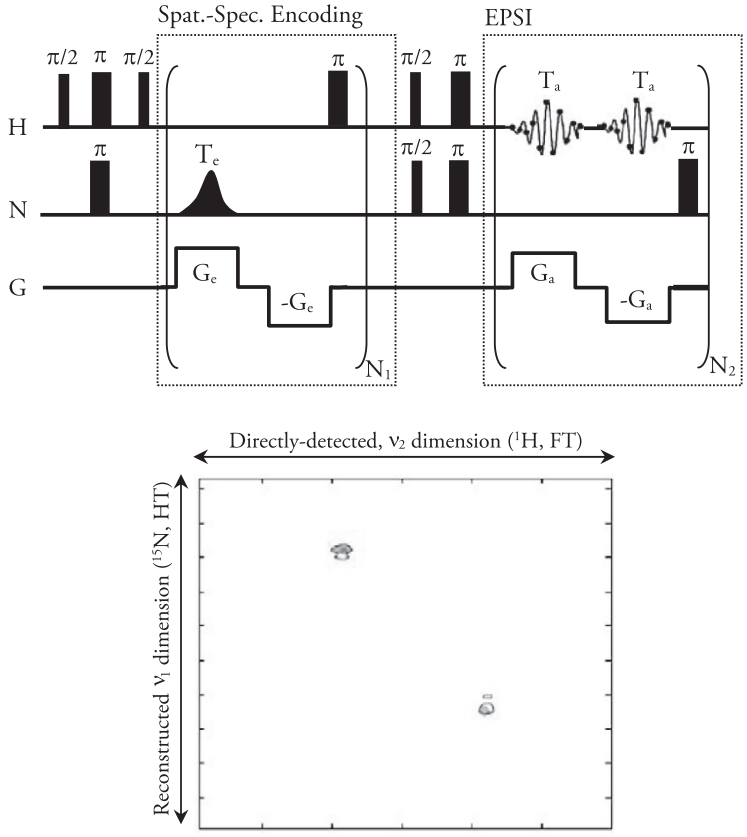

Fig. 30. HSQC single-scan 2D Hadamard spectroscopy. Top: outline of pulse sequence. The π-pulses within the HSQC sequence loops were used for heteronuclear decoupling. Bottom: results for a model LAF tripeptide (only amide groups were detected). Parameters used: $N_1 = 28, N_2 = 30, T_a = 250\ \mu s, T_e = 450\ \mu s, G_e = 4.2$ G/cm, $G_a = 7.5$ G/cm, RF pulse digitization dwell times = 10 μs, 2 kHz effective direct-domain acquisition spectral widths, 20 mm effective field-of-views, and 5 μs acquisition dwell times. The experiment was carried out on a 500 MHz Varian iNova spectrometer with a typical NMR coil length of 19 mm.

of all MRI-based methods is to map the NMR observables as a function of **r**. As the dimension of **r** is usually $\geqslant 2$, the natural formulation for these experiments is that of nD NMR. In this part of the Review, we therefore explore the prospects of obtaining nD NMR images of the spin density $\rho_0(\mathbf{r})$ for a given body, in a single-scan ultrafast fashion. As will be further discussed, the new spatially encoded alternative above presents some similarities to traditional single-scan imaging methods, particularly with Mansfield's EPI. But, like the UF2DNMR methods from which it derives, spatially encoded MRI differs by its use of a fundamentally different way of encoding the spins' interactions. The most evident consequence of the new approach will be the loss of the usual Fourier transforms used in imaging: The signal $s(t)$ will become directly proportional to $\rho_0(\mathbf{r}_0(t))$, where $\mathbf{r}_0(t)$ is some trajectory that can be set by utilizing the acquisition gradients, $\mathbf{G}_a(t)$. Thus, instead of acquiring data in the so-called **k**-space, SPEN MRI acquires the image point-by-point in real, physical *xyz*-space. While endowed with certain disadvantages vis-a-vis EPI, it turns out that these new scheme is well-suited for addressing common spatially dependent artifacts such as B_0 and RF inhomogeneities, or multiple chemical shifts; these features are further described below.

In order to better highlight the new aspects associated with SPEN MRI, we begin this section with a short overview of conventional imaging methods. Spatially encoded MRI is then formulated for a one-dimensional case. These principles are then used to derive expressions for the spatial resolution and intrinsic signal-to-noise ratio (SNR) of the experiment; generalizations to two- and three-dimensional MRI acquisitions then follow. It will also be shown how various EPI features appear corrected in SPEN MRI (Section 5.4), and – using appropriate post-processing techniques – how its SNR can be brought up to par with conventional Fourier imaging. Finally, Section 6 will be concerned with some spectral aspects of these new single-scan imaging modalities it is shown how the same post-processing techniques used to improve the SNR of imaging experiments can be useful in obtaining multiple images of different chemical sites, while preserving the simplicity and single-scan character of the experiment. We conclude by showing how SPEN MRI can also be used to acquire a 2D NMR *spectrum* by the application of a single excitation chirped pulse, adding another spatial-encoding method to the arsenal outlined in Section 3.1.

5.1. nD NMR imaging

We begin by focusing on classical NMR imaging experiments designed to obtain a spin density ($\rho_0(\mathbf{r})$) map, while neglecting all other effects, such as relaxation and diffusion. Therefore, unless otherwise noted (e.g., in Section 6), a single site whose chemical shift is zero will be assumed.

In an imaging experiment [58,59], all spins in the sample are initially assumed to be aligned with the main magnetic field. The magnitude of the magnetization vector varies from point to point, and is proportional to the spin density function, $\mathbf{M}(\mathbf{r}) \propto \rho_0(\mathbf{r})\hat{\mathbf{z}}$. Following a hard $\frac{\pi}{2}$ excitation pulse, all spins are brought into the rotating frame Bloch sphere's $\hat{x}\hat{y}$-plane, so $\mathbf{M}(\mathbf{r}) \propto \rho_0(\mathbf{r})\hat{\mathbf{x}}$. Once tipped, the magnetization is acquired in the presence of a time-dependent gradient, $\mathbf{G}_a(t)$. Letting $\mathbf{k}(t) = \gamma \int_0^t \mathbf{G}_a(t')dt'$, it was noted in Section 2.1 that the signal $s(t)$ can be considered a function of $\mathbf{k}(t), s(t) = s(\mathbf{k}(t))$ (Eq. (7)), and that varying $\mathbf{G}_a(t)$ allows one to

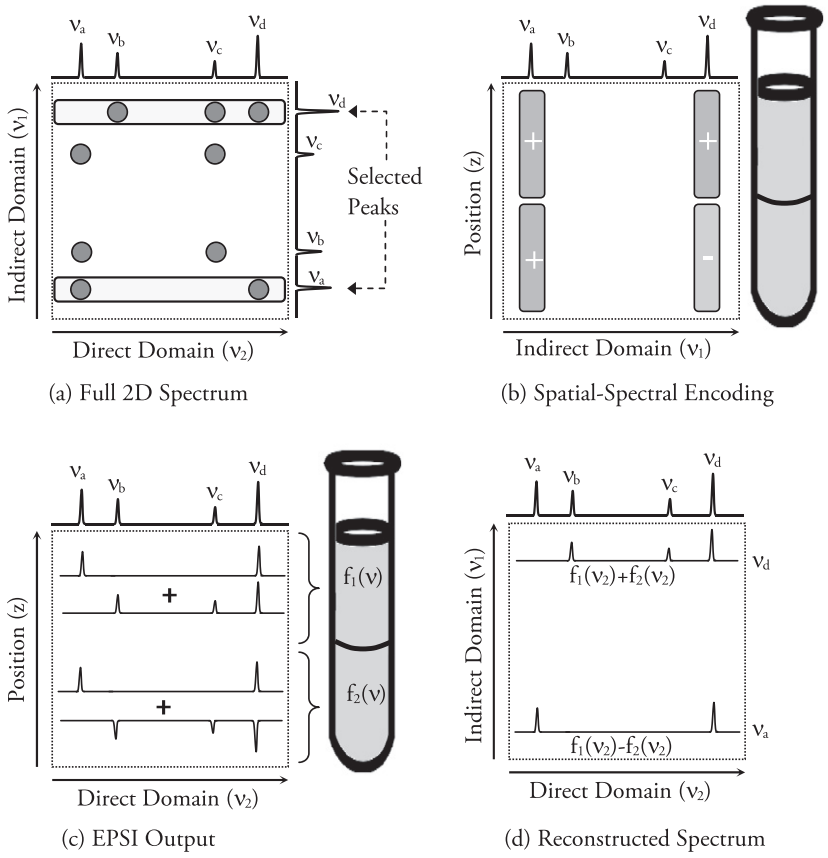

(a) Full 2D Spectrum (b) Spatial-Spectral Encoding

(c) EPSI Output (d) Reconstructed Spectrum

Fig. 31. Single-scan Hadamard experiment outlined for $N_{peaks} = 2$ sites of interest. In (a), these are encoded using a spatial-spectral pattern which follows a 2×2 Hadamard matrix (b). An EPSI sequence is used to retrieve the spatial-spectral pattern following mixing (c). The spectral profile of each slice $f_j(v)$ now contains the sums and differences of the individual spectra, encoded with the appropriate phases. To reconstruct the rows of interest, appropriate sums and differences of $f_j(v)$ values are taken. These resulting N_{peaks} 1D data sets can then be arranged in a 2D plot (d).

Table 4
Single-scan Hadamard experimental parameters.

To set ...		Set		... to
SW_1	The spectral width along the indirect domain	T_e	The duration of the excitation gradient's lobe	$\frac{1}{2SW_1}$
$\Delta\nu_1$	The spectral selectivity along the indirect domain	N_1	The number of iterations of the excitation gradient	$\frac{1}{2T_e\Delta\nu_1}$
N_{peaks}	The number of peaks of interest	G_e	The excitation gradient	$\frac{N_{peaks}}{LT_e}$
SW_2	The spectral width along the direct domain	T_a	The duration of the acquisition gradient's lobe	$\frac{1}{2SW_2}$
$\Delta\nu_2$	The spectral selectivity along the direct domain	N_2	The number of iterations of the acquisition gradient	$\frac{1}{2T_a\Delta\nu_2}$
–	–	$k^{(a)}_{max} = \gamma G_a T_a$	The maximal k-value during acquisition	$k^{(e)}_{max} = \gamma G_e T_e$
–	–	δt	The receiver dwell time	At most $\frac{1}{\gamma G_a L}$

vary $\mathbf{k}(t)$ and hence sample the response of the spins in the so-called **k**-space.

There are many protocols available for acquiring complex data sets in **k**-space, each with its own advantages and disadvantages. Two such protocols, dealing with a two-dimensional **k**-space, are illustrated in Fig. 35. Both approaches begin with a spatially-selective pulse along the z-axis to excite a particular plane of the object to be imaged; following this excitation the initial value of **k** is zero, but if purge gradients are applied one can shift this value prior to acquisition. This is exploited in 2D gradient echo (GRE) imaging (Fig. 35a) to perform several experiments sampling k_x along parallel, constant-k_y lines, but varying the initial value of k_y between experiments so as to eventually scan the full $k_x - k_y$ plane. This approach, in which one scans the $k_x - k_y$ plane line-by-line in independent scans and then Fourier transforms the result to obtain an image, is analogous to classical 2D NMR spectroscopy [14]: there one scans constant t_1 lines in the $t_1 - t_2$ plane and Fourier transforms the result to obtain a 2D spectrum. A main distinction between the imaging and spectroscopy protocols stems from the fact that k_x and k_y, unlike t_1 and t_2, can be given negative or positive values, simply by reversing the currents that generate the gradients. Moreover, the ability to arbitrarily vary $k_x(t)$ and $k_y(t)$ by controlling $G_x(t)$ and $G_y(t)$ allows one considerable freedom in designing the MRI acquisition protocols. In particular, it is possible to extend the scheme of Fig. 35a so as to scan the entire 2D data set within a single experiment. This is the main idea underlying the EPI experiment [60] illustrated in Fig. 35b, which shows how periodic variations of the gradients can trace a trajectory covering an entire region of interest throughout the 2D $k_x - k_y$ plane. Numerous different variations on this basic scheme have been

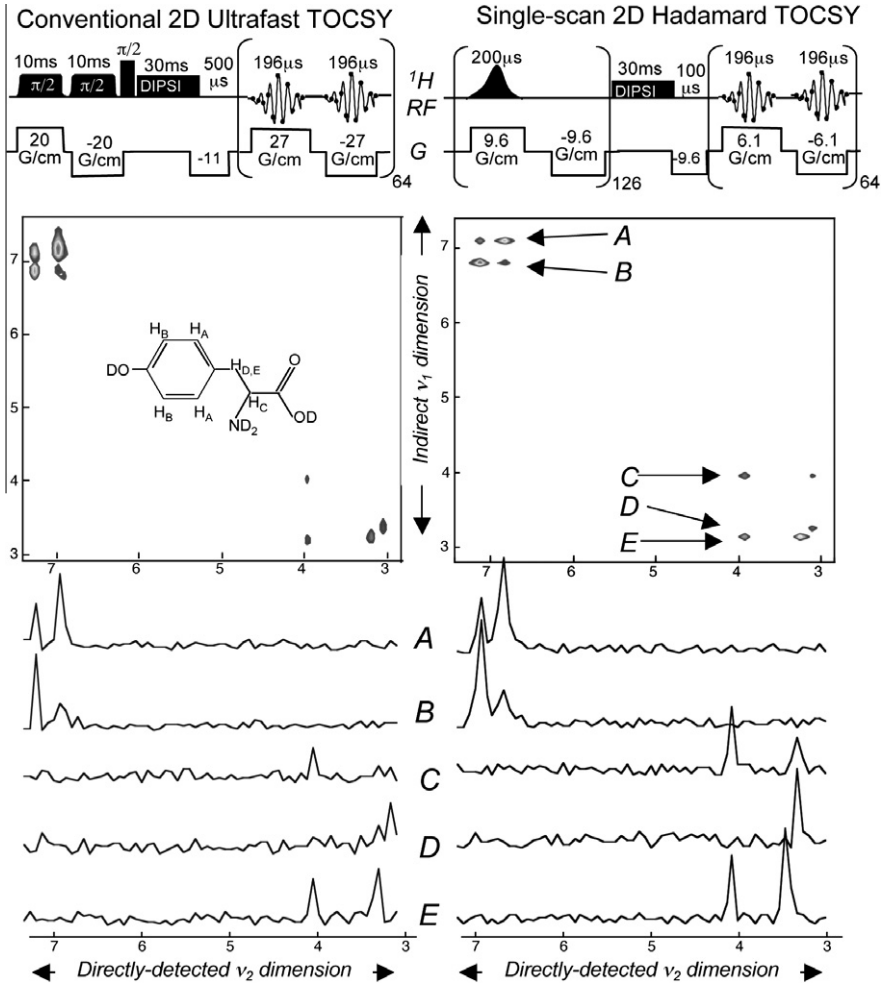

Fig. 32. Experimental comparison of signal-to-noise ratios between 2D Hadamard and ultrafast spectroscopies, by a 2D TOCSY NMR experiment, executed on a 2 mM *L*-tyrosine hydrochloride D_2O solution. (Top) Pulse sequences used in optimized ultrafast (left) and Hadamard-based acquisitions (right); further relevant parameters included filter bandwidths of ±108 and ±25 kHz respectively, and 2.4 kHz widths along both domains. (Center) Magnitude-mode 2D spectra afforded by each sequence, illustrating the chemical origin of each peak. (Bottom) Cross-sections afforded at the indicated arrow positions (plotted at equivalent noise levels) evidencing the sensitivity gains afforded by the Hadamard procedure for different sites.

suggested, including acquisitions along spiral trajectories [61,62], and interleaving multi-scan acquisitions. Many of those proposals are driven by the fact that, although the rectilinear EPI scheme in Fig. 35b allows one to acquire an entire 2D data set in a single-scan, it is very susceptible to field inhomogeneities, multiple chemical shifts and other experimental imperfections [62,63]. These issues will be further discussed below.

5.2. Principles of spatially encoded MRI

Conventional imaging monitors a signal proportional to the Fourier transform of the spin density $\rho_0(\mathbf{r})$. As such, the nature of the experiment is non-local, in the sense that every acquired point contains contributions from all physical points in the sample (Eq. (7)). Formally speaking, this is the result of the sine and cosine basis functions, $e^{i\mathbf{k}\cdot\mathbf{r}}$, having *non-local support*. Spatially-encoded imaging takes a different route by using *localized* basis functions having finite support; that is the signal, at every instant in time, originates (to a good approximation) from a particular localized physical point in the sample, and is proportional to the spin density $\rho_0(\mathbf{r})$ at that point. By applying gradients, this point can be shifted about the sample in a controlled manner. Acquiring while doing so yields a time-varying signal whose magnitude is equal to $\rho_0(\mathbf{r})$ along a particular trajectory in the sample.

The chirped RF pulses (Section 2) used within the context of spatial encoding will readily generate such a set of localized basis functions. Indeed, by exciting the spins onto the transverse plane, for instance by using a hard-pulse followed by a chirped π-pulse, will instill them with a quadratic phase given by[20]:

$$\phi_e(z) = -\frac{\gamma G_e T_e}{L} z^2 - \frac{\gamma G_e L T_e}{4}. \tag{72}$$

If a signal were to be acquired after exciting the spins, it would equal

$$\begin{aligned} s &\propto \int \rho_0(z) e^{\imath\phi_e(z)} dz \\ &= \int \rho_0(z) \cos(\phi_e(z)) dz + \imath \int \rho_0(z) \sin(\phi_e(z)) dz. \end{aligned} \tag{73}$$

Consider now the real part of this quantity: the rapidly varying quadratic nature of $\phi_e(z)$ will cause $\cos(\phi_e(z))$ – and, hence, $\rho_0(z)\cos(\phi_e(z))$ as well – to oscillate rapidly at nearly all points. When integrated over z, these oscillating regions will not contribute to the integral: on average, each positive region would be cancelled out by the negative region that immediately follows it. However, by

[20] Assuming $\Omega_1 = 0$, and a symmetric sweep with $\Delta O = \gamma G_e L$.

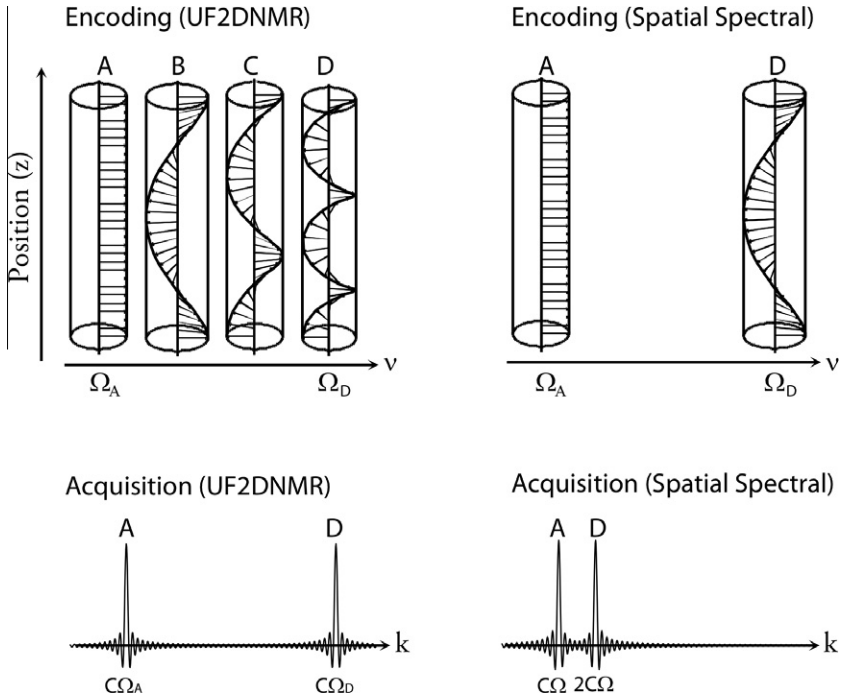

Fig. 33. "Conventional" (left) versus spatial-spectral (right) UF2DNMR, assuming a homogeneous sample composed of two distinct chemical sites, Ω_A and Ω_D. Their resulting echoes in UF2DNMR are spaced far apart. Prior knowledge of the chemical shifts, alongside the ability to excite arbitrary spatial-spectral profiles, allow one to design a spatial-spectral pulse which instills Ω_D with a lesser winding, moving the two echoes closer together. As a result, the acquisition time can be shortened, or, alternatively, the gradient diminished, resulting in a narrower filter bandwidth and increased signal-to-noise ratio.

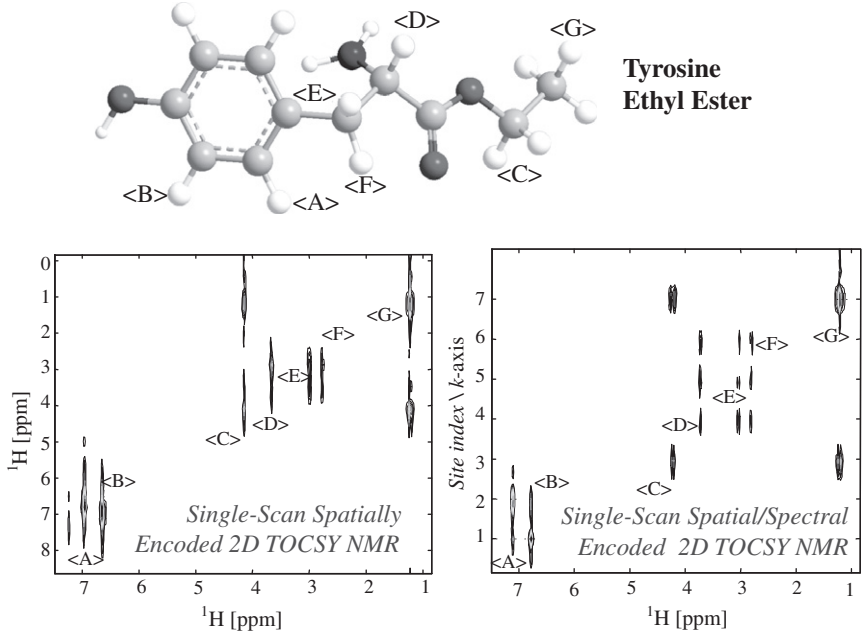

Fig. 34. Conventional (left) versus spatial-spectral (right) UF2DNMR TOCSY experiment on a sample containing tyrosine ethyl ester. Longer encoding times per unit acquisition gradient, made possible by the spatial-spectral encoding, have been used to increase the resolution along the indirect domain. (Taken from [57].)

virtue of $\phi_e(z)$ having a minimum at $z = 0, \cos(\phi_e(z))$ is relatively *stationary* and equal to unity near the extremal point $z = 0$, at which $\frac{d\phi_e}{dz} = 0$. The absence of fast oscillations at this stationary point implies that $\int \rho_0(z)\cos(\phi_e(z))dz \approx \rho_0(z=0)\Delta z$, where Δz is the width of the region over which $\cos(\phi_e(z))$ is approximately constant. This is illustrated in Fig. 36, for a particular $\rho_0(z)$.

The use of fast oscillating basis functions to localize the signal is a key element of SPEN MRI. The above reasoning shows that the use of such functions "suppresses" the signals coming from all points in the sample, except for a point at which the basis function is relatively stationary. This approximation is termed the *stationary phase approximation* [64], and is examined next in more detail.

5.2.1. SPEN MRI and the stationary phase approximation

The stationary phase approximation is best introduced by way of an example. Let $f(x) = e^{-\beta x^2}$, and consider the integral:

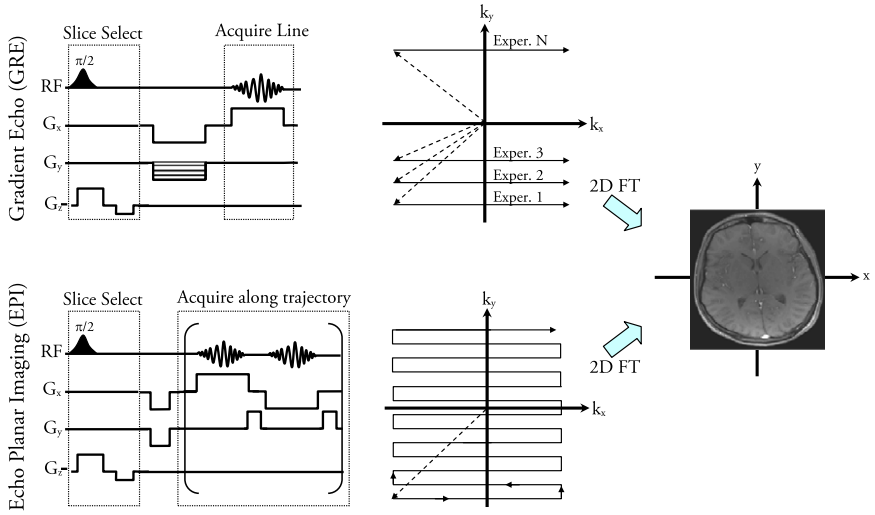

Fig. 35. Top: gradient-Echo (GRE) imaging. Bottom: Echo-Planar Imaging EPI. Both methods seek to sample the so-called **k**-space; the first does so with several experiments, varying the value of G_y between each experiment and scanning a different horizontal line in **k**-space; the second acquires the entire space in a single experiment. Both experiments use a selective pulse along the z-axis to initially select a particular slice of the sample; both apply a 2D Fourier transform to the acquired data in order to recover the image (which is proportional to $\rho_0(x,y)$).

$$I = \int_{-\infty}^{\infty} f(x) e^{\imath\phi(x)} dx. \tag{74}$$

$f(x)$ and $\phi(x) = \alpha x^2$ are plotted in Fig. 37a. The real part of $f(x)e^{\imath\phi(x)}$ functions is shown in Fig. 37b. For simple $f(x), \phi(x)$ functions, an exact evaluation of I is possible. It is also possible to obtain a general approximate expression for I, under the assumption that $\phi(x)$ varies rapidly compared to the function $f(x)$ (in the example discussed above this would entail the width of the parabola, $\phi(x) = \alpha x^2$, being much narrower than any variation in $f(x)$). The phase $\phi(x)$ will cause the function $f(x)e^{\imath\phi(x)}$ to oscillate rapidly at all points, except at points x_0 for which $\frac{d\phi}{dx} = 0$. At these points, the phase does not vary at all, and its change, to first-order, is zero: it is *stationary*. Those points x_0 for which the phase is stationary are called *stationary points*. When evaluating Eq. (74) one can, to first-order, neglect the fast oscillating parts of the integrand: a positive region of $f(x)e^{\imath\phi(x)}$ will soon be followed by a negative region of similar value and their sum will cancel out. The only contributions to I will arise from the function at the stationary points. For the case of a single stationary point x_0, one then has

$$I \approx (\text{width of stationary point region}) \times (\text{value of } f(x) \text{ at } x_0). \tag{75}$$

The width of the region of interest, schematically noted in Fig. 37b, can be found by expanding the phase about the stationary point in a Taylor series, $\phi(x) \approx \phi(x_0) + \frac{1}{2}\phi''(x_0)(x - x_0)^2$, and noting that the width of the bottom of the resulting parabola is approximately[21] $\sqrt{\frac{1}{\phi''(x_0)}}$. Formalizing these notions for the case of a single stationary point x_0, namely when $\frac{d\phi}{dx} = 0$ has a single solution, requires expanding $f(x), \phi(x)$ about x_0:

$$f(x) \approx f(x_0), \tag{76}$$

$$\phi(x) \approx \phi(x_0) + \frac{1}{2}\left(\frac{d^2\phi}{dx^2}\right)_{x=x_0} (x - x_0)^2. \tag{77}$$

Introducing these expressions back into Eq. (74) yields:

$$I \approx f(x_0) e^{\imath\phi(x_0)} \int_{-\infty}^{\infty} e^{\imath\frac{1}{2}\left(\frac{d^2\phi}{dx^2}\right)_{x=x_0}(x-x_0)^2} dx. \tag{78}$$

[21] The width of a parabola αx^2 about $x = 0$ is of the order $\sim \sqrt{\frac{1}{\alpha}}$.

The infinite integration can be evaluated analytically, with the final result being:

$$I \approx \frac{\sqrt{2\pi\imath} f(x_0) e^{\imath\phi(x_0)}}{\sqrt{\left(\frac{d^2\phi}{dx^2}\right)_{x=x_0}}}. \tag{79}$$

This derivation is general; it relies only on the phase $\phi(x)$ varying more rapidly than the function $f(x)$, and it is true for any $f(x)$ and $\phi(x)$. It is interesting to compare Eq. (79) for the special case $f(x) = e^{-\beta x^2}, \phi = \alpha x^2$. An exact analytic solution can then be found, and yields:

$$I_{\text{exact}} = \sqrt{\frac{\pi}{-\imath\alpha + \beta}}, \tag{80}$$

versus:

$$I_{\text{approx.}} = \frac{\sqrt{\pi\imath}}{\sqrt{\alpha}}. \tag{81}$$

The two results agree when $\alpha \gg \beta$, that is, when the phase varies much more rapidly than the function $f(x)$, in accordance with the assumptions made.

The stationary phase approximation can be extended to higher dimensions, by replacing the one-dimensional operators with their nD analogs. Let $f(\mathbf{x})$ be a function of n variables, $x_1, x_2, \ldots, x_n$, and let $\mathbf{x}_0$ be a stationary point of f, that is, $(\nabla f)_{\mathbf{x}=\mathbf{x}_0} = 0$; then:

$$\int_{\text{all space}} f(\mathbf{x}) e^{\imath\phi(\mathbf{x})} d\mathbf{x} \approx \frac{(2\pi\imath)^{\frac{n}{2}} f(\mathbf{x}_0) e^{\imath\phi(\mathbf{x}_0)}}{\sqrt{\det(H)_{\mathbf{x}=\mathbf{x}_0}}}, \tag{82}$$

where H is the *Hessian* of $\phi(\mathbf{x})$. For two dimensions ($n = 2$), for example, one has:

$$H(\mathbf{x}) = \begin{pmatrix} \partial_{xx}\phi(\mathbf{x}) & \partial_{xy}\phi(\mathbf{x}) \\ \partial_{yx}\phi(\mathbf{x}) & \partial_{yy}\phi(\mathbf{x}), \end{pmatrix} \tag{83}$$

(where ∂_{xy} stands for $\frac{\partial^2\phi}{\partial x \partial y}$, etcetera). The Hessian generalizes the notion of curvature – embodied in one dimension by the 2nd derivative – to an arbitrary number of dimensions.

5.2.2. Stationary points and SPEN MRI

With all these elements as background, the approach taken by spatially encoded UFMRI can be summarized as follows. First, the

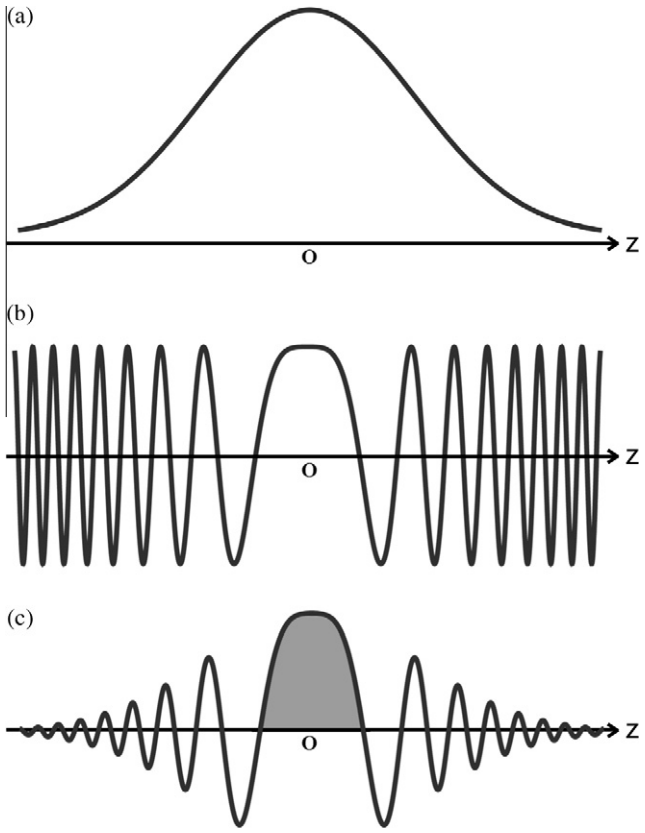

Fig. 36. The use of localized basis functions in spatially-encoded imaging. (a) Assumed spin density $\rho_0(z)$, as a function of position. (b) The cosine of the phase following a hard excitation pulse and a chirped π-pulse: $\cos(\phi_e(z))$. (c) The product $\rho_0(z)\cos(\phi_e(z))$, equal also to the (real part of the) integrand in Eq. (73). Due to the oscillatory nature of the function, integrating over it will average out to zero, except for the shaded region. The width of the shaded region is determined by the basis function shown in (b), while the area is proportional to ρ_0 at $z = 0$.

spins' transverse magnetizations are given a quadratic phase profile, $\phi(\mathbf{r})$, having a minimum at some physical point in the sample, $\mathbf{r}_0$; that is, $(\nabla\phi)_{\mathbf{r}=\mathbf{r}_0}$. This can be carried out by applying a gradient and exciting the spins with a chirped $\frac{\pi}{2}$ pulse; alternatively, one could apply a homogeneous, hard $\frac{\pi}{2}$ pulse, followed by an adiabatic π-sweep executed under the action of a gradient. Then, by applying acquisition gradients (which add phase terms that are linear in position), the minimum $\mathbf{r}_0$ can be moved about some trajectory, the precise shape of which depends on the precise time-dependence of the gradients. Due to the rapidly varying quadratic phase, the signal from all spins in the sample will interfere destructively except at $\mathbf{r}_0$, where the phase is stationary. Hence, if at time t_0 the minimum is at $\mathbf{r}_0(t_0)$, then $s(t) \propto \rho_0(\mathbf{r}_0(t_0))$. Since the signal is proportional to $\rho_0(\mathbf{r})$ along the trajectory, no Fourier transform is needed to extract the image – merely monitoring the data and arranging the collected FID on an nD-grid suffices.

5.2.3. Example #1: 1D spatially-encoded imaging

In order to get a feel for the magnitudes involved and their dependence on the various parameters, the simple 1D case shown in Fig. 38 will be examined. The $\frac{\pi}{2}$ chirped pulse tips the spins onto the $\hat{x}\hat{y}$-plane and creates a quadratic phase dependence given by Eq. (14). Assuming a symmetric bandwidth ΔO, the excitation phase can be precisely recast in the form $\phi_e(z) = \frac{1}{2}\alpha_z(z - z_0)^2$ with:

$$\alpha_z = \frac{T_e(\gamma G_e)^2}{\Delta O}, \tag{84}$$

$$z_0 = \frac{\Delta O}{2\gamma G_e}. \tag{85}$$

By adjusting ΔO accordingly, one can set the initial acquisition point, z_0, arbitrarily. Denoting $\Delta O = (O_f - O_i) = \gamma G_e z_{f,e} - \gamma G_e z_{i,e}$, where $z_{i,e}, z_{f,e}$ are the initial and final points excited by the chirped pulse, respectively, one has:

$$\alpha_z = \frac{\gamma G_e T_e}{L_e}, \tag{86}$$

$$z_0 = z_{f,e}. \tag{87}$$

The symmetric excitation sweep means that $z_{f,e} = -z_{i,e}$, and $L_e \equiv z_{f,e} - z_{i,e} = 2z_{f,e} = -2z_{i,e}$. Note that if one were to begin acquisition at this point in time, the first data point at $t = 0$ would be proportional to $\rho_0(z_{f,e})$, the spin density at the last point excited by the chirp. When a signal is next acquired in the presence of a gradient, the spins' phase becomes time-dependent,

$$k(t) = \gamma\int_0^t G_a dt' = \gamma G_a t, \tag{88}$$

$$\phi(z,t) = \Phi_e(z) + k(t)z = \frac{1}{2}\alpha_z(z - z_0(t))^2, \tag{89}$$

$$z_0(t) = z_0 - \frac{k(t)}{\alpha_z} = z_{f,e} - \left[\frac{\gamma G_a L_e^2}{T_e^2}\right]t, \tag{90}$$

and the signal itself, as picked up by the receiver, will be:

$$s(t) \propto \int_{\text{the sample}} M_+(z,t)dz \approx \rho_0(z_0(t))e^{i\phi(z_0(t),t)}\delta z, \tag{91}$$

where δz is denoted by

$$\delta z \equiv \sqrt{\frac{2\pi}{\alpha_z}} = \sqrt{\frac{2\pi L_e}{\gamma G_e T_e}}. \tag{92}$$

The absolute magnitude of the signal will therefore be proportional to:

$$|s(t)| \propto |\rho_0(z_0(t))\Delta z|, \tag{93}$$

with $z_0(t)$ given by Eq. (90). Setting $k_{\max}^{(a)} \equiv \gamma G_a T_a = -\gamma G_e T_e \equiv -k_{\max}^{(e)}$, ensures that $z_0(T_a) = z_0\left(-\frac{G_e T_e}{G_a}\right) = z_{i,e}$, thus probing in a linear manner the region from $z_{f,e}$ to $z_{i,e}$, as shown in Fig. 39. The order in which the image is unraveled is, therefore, opposite to the order in which the spins are excited.

Fig. 40 presents the results of several computer simulations of the pulse sequence in Fig. 38. In each figure, the dashed line is the initial spin density $\rho_0(z)$ while the solid line is the absolute value $|s(t)|$ of the acquired FID. Fig. 40a shows the response to a square input profile. The sharp discontinuity at the edges of the profile causes the image to deviate from a rectangular shape; this is due to a breakdown of the stationary phase approximation, which requires the phase to vary more rapidly than the profile being imaged. On the other hand, in Fig. 40b the acquired image coincides with $\rho_0(z)$ perfectly, demonstrating the effectiveness of the method. Fig. 40c serves to highlight another point of interest, that of spatial resolution. As in Fig. 40a, the stationary phase approximation breaks down, since the quadratic phase changes more slowly than the spin density $\rho_0(z)$ being imaged. Put another way, the quadratic phase $\frac{1}{2}\alpha_z(z - z_0)^2$ defines a point spread function whose width, given by $\sqrt{\frac{2\pi}{|\alpha_z|}} = \delta z$, is wider than $\rho_0(z)$.

Fig. 41 presents an experimental comparison in one dimension of spatially encoded and of conventional, Fourier transform, GRE-based imaging, with the images shown alongside the respective pulse sequences used to obtain them.

5.2.4. Example #2: 2D SPEN MRI

A possible way to extend the above scheme to the single-shot scanning of two spatial dimensions is shown in Fig. 42a. The spins,

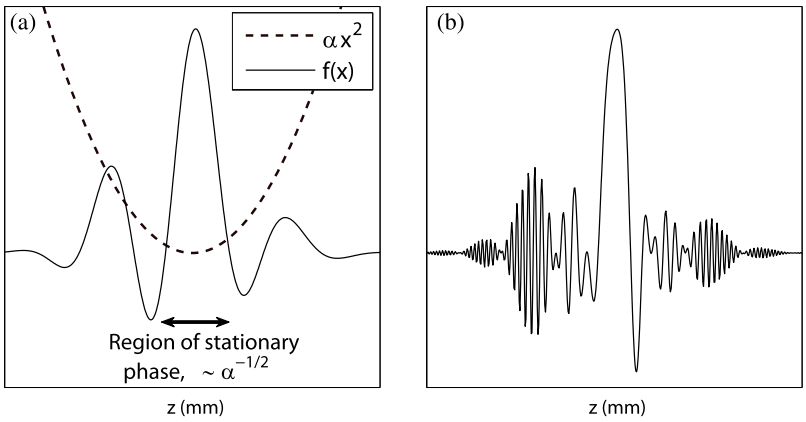

Fig. 37. The stationary phase approximation, illustrated. (a) Solid line: an arbitrary function $f(x)$. Dashed line: $\phi(x) = \alpha x^2$. (b) The real part of $f(x)e^{\imath\phi(x)}$, equal to $f(x)\cos(\phi(x))$, clearly showing the function oscillates rapidly except at the region about the stationary point, the width of which is determined by the phase $\phi(x)$.

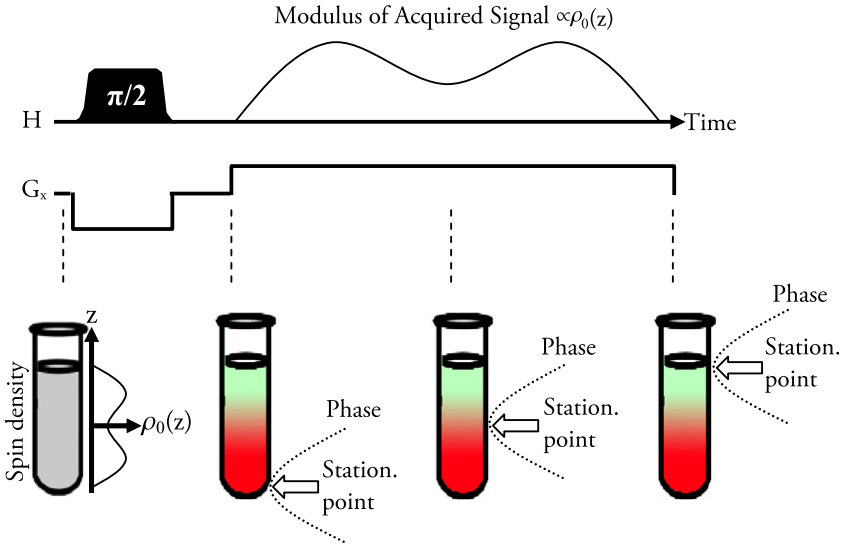

Fig. 38. 1D spatially-encoded imaging (SPEN MRI). An initial $\frac{\pi}{2}$ chirped pulse excites the spins sequentially onto the $\hat{x}\hat{y}$-plane, creating a quadratic phase having an extremal point at one end of the sample. Acquiring in the presence of a gradient with an opposite sign shifts the extremal point continuously throughout the sample, generating a signal whose modulus is proportional to the spin density, $\rho_0(z)$.

initially in thermal equilibrium, are along the Bloch sphere's z-axis, $\mathbf{M}(\mathbf{r}) \propto \rho_0(\mathbf{r})\hat{\mathbf{z}}$. Following a chirped $\frac{\pi}{2}$ pulse along the $\hat{x}$-axis, applied in the presence of a gradient G_e^x, the spins are excited onto the Bloch sphere's $\hat{x}\hat{y}$-plane with a quadratic phase given by Eq. (14). Hence, the magnetization can be written as $M_+(\mathbf{r}) \propto \rho_0(\mathbf{r})e^{-\imath\frac{1}{2}\alpha_x(x-x_0)^2-\imath C_x}$, where

$$\alpha_x = \frac{(\gamma G_e^x)^2 T_e}{\Delta O}, \tag{94}$$

$$x_0 = -\frac{\Delta O}{2\gamma G_e^x}, \tag{95}$$

$$C_x = \frac{\pi}{2} + \frac{T_e \Delta O}{4}, \tag{96}$$

under the assumption that $\Omega_1 = 0$ and that ΔO is symmetric about zero. C_x is a constant independent of x, and can be omitted as it will not affect the conclusions or derivation.

Following the $\frac{\pi}{2}$ excitation chirp, a π-chirp is applied in the presence of a gradient G_e^y along the y-axis. This adds a quadratic y-dependent phase to the spins as indicated by Eq. (27), such that, following the pulse, $M_+(\mathbf{r}) \propto \rho_0(\mathbf{r})e^{\imath\frac{1}{2}\alpha_x(x-x_0)^2+\imath\frac{1}{2}\alpha_y(y-y_0)^2+\imath C_y}$ with

$$\alpha_y = \frac{2(\gamma G_e^y)^2 T^{(\pi)}}{\Delta O^{(\pi)}}, \tag{97}$$

$$y_0 = 0, \tag{98}$$

$$C_y = -\frac{T^{(\pi)}\Delta O^{(\pi)}}{4}. \tag{99}$$

As before, C_y will be omitted. Purge gradients are then applied along both axes. They serve to add a constant phase of the form $\beta_x x + \beta_y y$, which, in effect, allows one to calibrate x_0, y_0 precisely. For example, one can choose (x_0, y_0) to be the coordinates of the point A shown in Fig. 42b.

Consider next the acquisition portion of the sequence. By varying the gradients, x_0 and y_0 can be made time-dependent. Owing to the stationary phase approximation, the signal at every instant throughout the acquisition will, to a very good approximation, originate solely from the point (x_0, y_0) and be proportional to $\rho_0(x_0, y_0)$. By varying the acquisition gradients throughout acquisition one can change the position of (x_0, y_0), and record $\rho_0(x_0(t), y_0(t))$ along some path determined by the user – e.g., the path shown in Fig. 42b (with the corresponding gradients illustrated in Fig. 42a). The only post-processing needed to retrieve the 2D image in this case would be to rearrange the acquired data

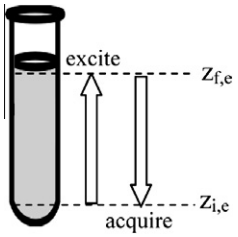

Fig. 39. The $\frac{\pi}{2}$-chirp, which serves to excite the spins sequentially onto the $\hat{x}\hat{y}$-plane by sweeping its frequency from $O_i = \gamma G_e z_{i,e}$ to $O_f = \gamma G_e z_{f,e}$, creates a quadratic phase having an extremal point at $z_{f,e}$. Acquiring in the presence of a gradient with an opposite sign ensures the extremal point moves from $z_{f,e}$ back to $z_{i,e}$.

along the predetermined trajectory; no Fourier transformation of the data is needed.

To see how this comes about in more detail, we denote, as before, $\mathbf{k}(t) = \gamma \int_0^t \mathbf{G}_a(t')dt'$, where $t = 0$ signifies the beginning of acquisition. Using this notation, the transverse magnetization during acquisition can be written as:

$$M_+(\mathbf{r},t) \propto \rho_0(\mathbf{r}) e^{\imath\left(\frac{1}{2}\alpha_x(x-x_0)^2 + \frac{1}{2}\alpha_y(y-y_0)^2 + k_x(t)x + k_y(t)y\right)} \equiv \rho_0(\mathbf{r}) e^{\imath\phi(\mathbf{r},t)}. \quad (100)$$

The time-dependent minimum of the phase $\phi(\mathbf{r},t)$ can be found by solving $(\nabla\phi(\mathbf{r},t))_{\mathbf{r}=\mathbf{r}_0} = 0$, which yields:

$$x_0(t) = x_0 - \frac{k_x(t)}{\alpha_x}, \quad (101)$$

$$y_0(t) = y_0 - \frac{k_y(t)}{\alpha_y}. \quad (102)$$

Eqs. (101) and (102) illustrate an important feature: the trajectory $\mathbf{r}_0(t) = (x_0(t), y_0(t))$ is linear in $\mathbf{k}$. Thus, to increase x_0 we apply a positive x-gradient, and to decrease x_0 apply a negative x-gradient.

Using the stationary phase approximation and the above expressions for $M_+(\mathbf{r},t)$, the signal $s(t) \propto \int M_+(\mathbf{r},t)d\mathbf{r}$ can be approximated using Eq. (82) (up to constant factors depending on coil geometry, etc.) as:

$$s(t) \approx \frac{2\pi\imath\rho_0(x_0(t), y_0(t)) e^{\imath\phi(x_0(t),y_0(t),t)}}{\sqrt{\alpha_x\alpha_y}}, \quad (103)$$

since the Hessian of $\phi(\mathbf{r},t)$ is

$$H(\mathbf{r},t) = \begin{pmatrix} \alpha_x & 0 \\ 0 & \alpha_y \end{pmatrix}, \quad (104)$$

and its corresponding (time-independent) determinant is $\det H = \alpha_x\alpha_y$.

5.2.5. Resolution considerations

It is instructive to compare the resolution offered by SPEN MRI against that offered by conventional Fourier imaging methods, by examining the one-dimensional case. Eq. (92) expresses the voxel size δz for the spatially encoded case. Assuming that the excited region L_e equals the desired field of view (FOV), and that the sample is excited as shown in Fig. 39, with $\gamma G_a T_a = -\gamma G_e T_e$, then

$$\delta z^{(\text{SPEN MRI})} = \sqrt{\frac{\text{FOV}}{|\gamma G_a T_a|}}. \quad (105)$$

In Fourier imaging, on the other hand, the voxel size is determined by the inverse of the scan's dimensions in k-space, $\delta z^{(\text{FT})} = \frac{1}{k_{\max}^{(a)}} = \frac{1}{\gamma G_a T_a}$. Therefore, assuming the same parameters (G_a, T_a, FOV) for both pulse sequences, one obtains:

$$\frac{\delta z^{(\text{SPEN MRI})}}{\delta z^{(\text{FT})}} = \sqrt{\gamma G_a T_a \text{FOV}} = \sqrt{N^{(\text{FT})}}, \quad (106)$$

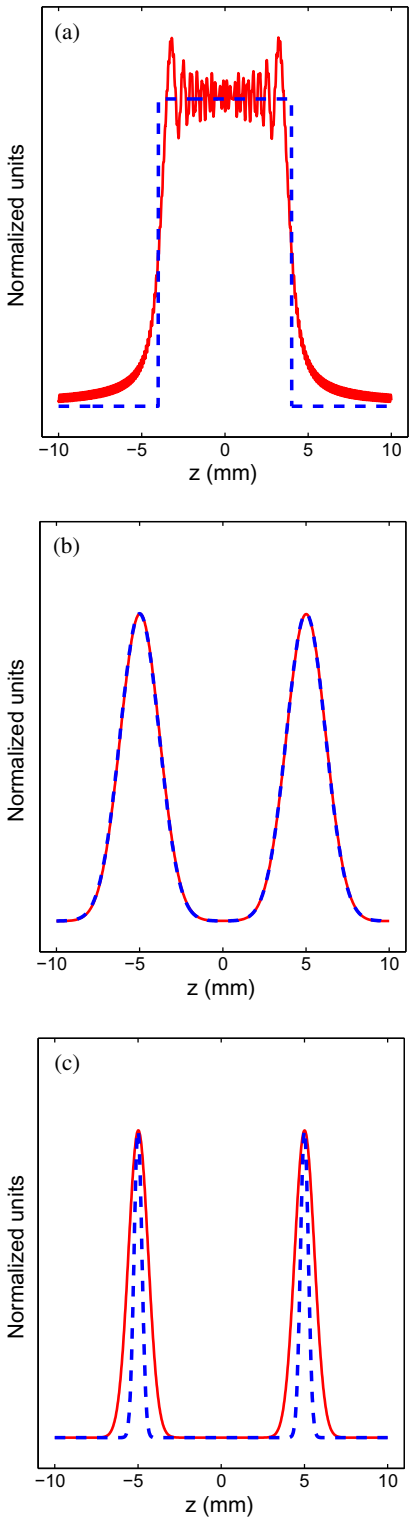

Fig. 40. Simulation results: spin densities $\rho_0(z)$ (dashed line) versus acquired image (solid line) using 1D SPEN MRI, following the pulse sequence shown in Fig. 39a with $T_e = 5$ ms, $\gamma G_e = 5$ kHz/mm, sample size $L = 20$ mm, $\Delta O = \gamma G_e L = 100$ kHz, $G_a = -G_e$ and $T_a = -T_e$. (a) Square profile, showing the breakdown of the stationary phase approximation due to a discontinuous, abruptly-changing profile $\rho_0(z)$. (b) Two Gaussians, $\rho_0(z) = \exp\left(-\left(\frac{z-L/4}{\sigma}\right)^2\right) + \exp\left(-\left(\frac{z+L/4}{\sigma}\right)^2\right)$ with $\sigma = 1.66$ mm – the agreement between the simulated and actual profiles illustrates the effectiveness of the method. (c) Same as in (b), with $\sigma = 0.33$ mm. Here, the profile $\rho_0(z)$'s spatial variations occur on a smaller scale than the width of the parabolic phase – that is, they are finer than the method's intrinsic resolving power – resulting in a smeared, wider point-spread function.

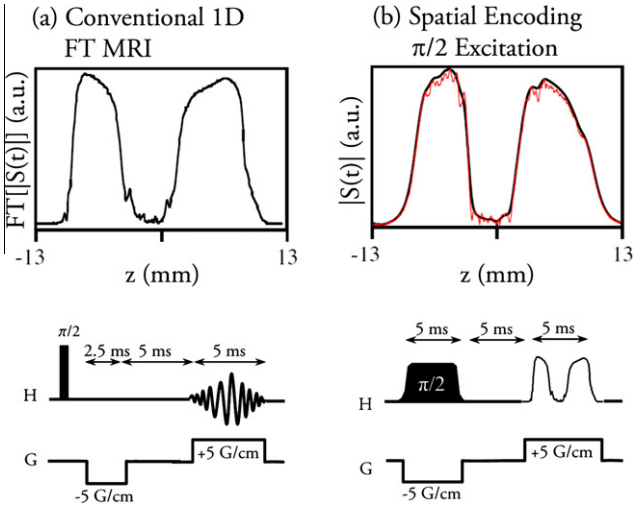

Fig. 41. Experimental comparison of conventional (a) and spatially-encoded (b) one-dimensional images, presented alongside the respective pulse sequences used to obtain them. The experiments were carried out on a uniform water-based polyacrylamide gel filling a 5 mm NMR tube, doped at its center with a $CoCl_2$ solution. The observation coil was nearly 18.5 mm in length, and the paramagnetic doping led to a low signal-intensity region ca. 3 mm long. Like all remaining experiments detailed in this review, these measurements were carried out at 500 MHz using a Varian iNova NMR console. Note the 5 ms delay times used to ensure full decay of the spins in the middle of the sample.

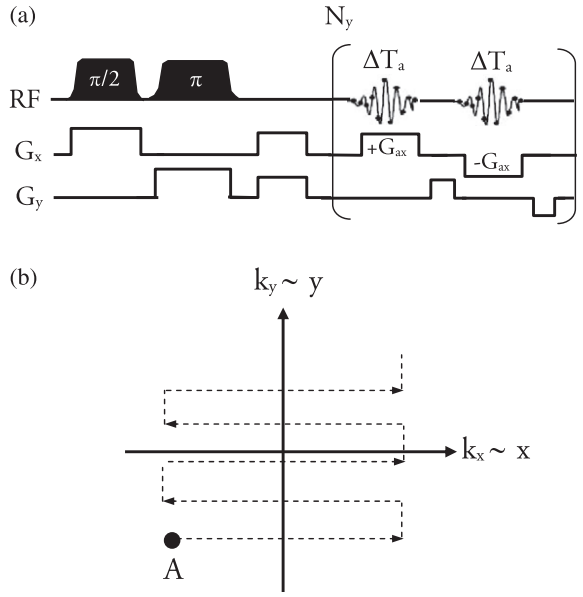

Fig. 42. (a) 2D SPEN MRI-based pulse sequence. The spins are first excited onto the $\hat{x}\hat{y}$-plane with the aid of a $\frac{\pi}{2}$ pulse, creating a quadratic phase $\phi(x,y)=\frac{1}{2}\alpha_x(x-x_0)^2$. A π-chirped pulse in the presence of G_y adds a quadratic phase along the y-axis, $\phi(x,y)=\frac{1}{2}\alpha_x(x-x_0)^2+\frac{1}{2}\alpha_y(y-y_0)^2$. Simultaneous purge gradients add linear components and ensure that $\phi(x,y)$ has an extremal point at A, shown in (b). The extremal point is shifted during acquisition – once again, using gradients – to sweep the path shown in (b). Note that although formally one might say $\mathbf{k}(t)=\int_0^t \mathbf{G}_a(t')dt'$ varies, the acquisition path is traced in real (as opposed to Fourier) space.

where $N^{(\mathrm{FT})}$ is the number of voxels acquired in the conventional imaging experiment, $N^{(\mathrm{FT})}=\frac{k_{\max}^{(a)}}{\delta k}=\frac{\gamma G_a T_a}{\mathrm{FOV}^{-1}}$. Eq. (106) entails a significant penalty, whose resolution is further discussed below.

5.2.6. Super-resolution

Eq. (106) highlights the main drawback of the spatial encoding protocol discussed in Section 5.2, compared to conventional Fourier-based MRI: its resolution per unit gradient is lower. Equivalently stated, the point-spread function offered by the spatially encoded methods relying on a simple magnitude signal calculation will, for a given set of imaging parameters (G_a, T_a and FOV), be $\sqrt{N}$ larger than the Fourier voxel size (given by $\frac{1}{k_{max}}=\frac{1}{\gamma G_a T_a}$).

An implicit assumption leading to this conclusion is that the number of voxels along the spatially-encoded direction equals $N_{\mathrm{UF}}\equiv\frac{FOV}{\delta z}$, where δz is given by Eq. (105). While it is true that the intrinsic width of the point-spread-function in SPEN MRI is given by δz, it is, in fact, possible to oversample the image, by shifting the quadratic phase in spatial increments smaller than δz while constantly acquiring data. The resulting signal (given, for example, by Eq. (91) in 1D), would still remain proportional to the spin density being sought, but it would now contain *redundancy*; that is, it may substantially exceed the number of voxels N_{UF}. This redundancy can be exploited to increase the image's resolution well beyond that given by δz in Eq. (105). Exploiting such redundancy is an example of "super-resolution" processing, whose details are outlined in this section for the 1D case.

The signal at times $t_k=k\delta t, k=1,2,\ldots,M$, given in 1D by Eq. (91), can be approximated by replacing the spatial integration over the sample by a discrete sum of the form

$$s(t_k)\approx\sum_{p=1}^{N_{SR}}M_+(z_p,t_k)\Delta z=\sum_{p=1}^{N_{SR}}\rho_0(z_p)e^{\imath\phi(z_p,t_k)}\Delta z, \tag{107}$$

where N_{SR} is the number of discrete elements used to approximate the integral, $\Delta z=\frac{FOV}{N_{SR}}$, $\rho_0(z)$ is the sought-after spin density, and $\phi(z,t)\equiv\phi_e(z)+\phi_a(z,t)$ is the acquisition phase of the signal, given by the sum of the quadratic phase $\phi_e(z)$ induced by the excitation chirp and the gradient-induced acquisition phase $\phi_a(z,t)=k(t)z$. Eq. (107) is equivalent to a matrix equation of the form

$$\begin{pmatrix}s(t_1)\\ s(t_2)\\ \ldots\\ s(t_M)\end{pmatrix}=\begin{pmatrix}M\times N_{SR}\\ \text{matrix}\end{pmatrix}\begin{pmatrix}\rho(z_1)\\ \rho(z_2)\\ \ldots\\ \rho(z_{N_{SR}})\end{pmatrix}. \tag{108}$$

That is, $\mathbf{s}=\mathbf{P}\boldsymbol{\rho}$, with $\mathbf{s}$ and $\boldsymbol{\rho}$ being column vectors and $\mathbf{P}$ an $M\times N_{SR}$ matrix which depends solely on the *a-priori* known acquisition parameters. Recovering the column vector $\boldsymbol{\rho}$ is a matter of inverting Eq. (108), using, for example, iterative gradient-descent methods to minimize the error of the solution [65]. This approach is one example of the use of oversampling to achieve "super-resolution". Still, since the time signal $s(t_k)$ is also accompanied by noise, care must be taken with regard to the stability and accuracy of the numerical operations. In the present instance, the inversion of Eq. (108) is particularly well-conditioned, owing to the parabolic phase characterizing the matrix $\mathbf{P}$.

The number of individual equations in Eq. (108) is given by M, the number of time points, while the number of voxels sought after in the super-resolved image is given by N_{SR}, a free parameter. For $N_{SR}>M$ – that is, if forcing a search for more spatial points than there are temporal ones – unstable solutions result. In practice, the limit $N_{SR}=M$ is found to be often achievable. Thus, using oversampling, the number of voxels can be made equal to the number of acquired points, making it dependent on the acquisition parameters as in conventional Fourier imaging. This can easily offset the handicap encompassed by Eq. (106), as illustrated by the simple synthetic patterns shown in Fig. 44.

5.3. Hybrid imaging techniques

Fourier and spatially-encoded imaging have different strengths. Eq. (106) shows that Fourier imaging offers superior resolution per unit gradient during acquisition. As discussed below, however,

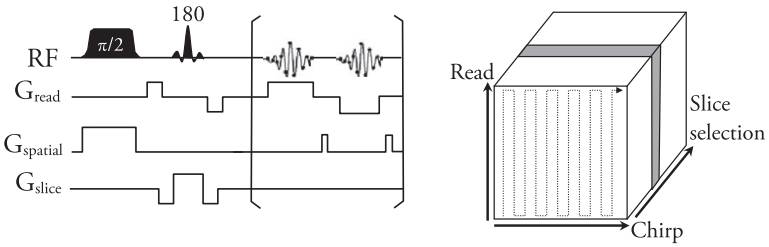

Fig. 43. Left: hybrid imaging pulse sequence. After exciting the spins and spatially encoding one axis, a slice-selective 180 is applied, with crusher gradients to dephase the out-of-slice spins. Then, a 2D image is scanned, using frequency encoding along the read direction and spatial encoding along the blipped axis; the resulting 2D data set then is Fourier transformed only along the read direction to yield the final image. Right: an illustration of the slice selection, as well as the trajectory traversed along the spatially- and frequency-encoded axes.

SPEN MRI is particularly well-suited for coping with field inhomogeneities (Section 5.4) and multiple chemical shifts (Section 6.1). Sometimes it is possible to combine the advantages of both approaches by applying different encodings to orthogonal axes. One might, for example, exploit the immunity to inhomogeneity along a low-bandwidth, blipped[22] dimension by spatially encoding it, while enjoying the superior resolution and sensitivity offered by the Fourier method by using a conventional k-encoding along the orthogonal axis [66,67]. Since the spatially-encoded axis in the resulting hybrid imaging approach is in essence one-dimensional, it is meaningful to spend some time studying the properties of 1D SPEN MRI in depth; it will be noted, wherever appropriate, how the results obtained can be incorporated into hybrid imaging. In particular, using super resolution, as described in Section 5.2.6, yields an image comparable in resolution to EPI, while enjoying the aforementioned benefits offered by spatial encoding. This is illustrated in Fig. 45.

Two additional benefits are worth highlighting in connection to these hybrid imaging approaches. One relates to the possibility of using a large acquisition gradient along the blipped, spatially-encoded direction, to unravel the low-bandwidth image. Indeed, as detailed in Section 5.2.3, the acquisition gradient G_a along the spatially-encoded axis satisfies $G_aT_a = G_eT_e$, where T_a is the total time during which G_a is applied along the blipped axis, and T_e and G_e are the duration of the chirped excitation pulse and the excitation gradient, respectively. In principle, spatial encoding does not place an intrinsic limit on the magnitude of G_e, which is therefore limited only by hardware and safety considerations. By increasing G_e, G_a can be increased as well. This is in contrast to echo-planar imaging, in which the strength of the blipped acquisition gradient is limited. The enlarged acquisition gradient diminishes susceptibility artifacts and the effects of B_0 imperfections. The second benefit relates to the possibilities of generating a full T_2^* refocusing for every spatially encoded voxel and throughout the acquisition of the 2D data [67]. This enables a substantial cancellation of dephasing and inhomogeneity effects.

5.4. Spatial inhomogeneity correction with ultrafast MRI

As SPEN MRI unravels the image point-by-point, it provides a good starting point for compensating for the effects of spatial inhomogeneities in the main B_0 (or the B_1) field. The basic concepts will be first presented in a single dimension and their generalization to 2D/3D cases will be discussed subsequently. Note that, since hybrid imaging techniques (Fig. 43) enable one to spatially encode a single axis and use conventional k-space imaging on other axes, one-dimensional inhomogeneity corrections may not be merely academic curiosities but valid and useful imaging tools.

[22] A "blipped" gradient is one which is turned on sparsely and for short periods of time. In 2D EPI, for example, the phase encoded axis is often advanced by means of a "blipped" gradient.

5.4.1. B_0 inhomogeneity correction in one dimension

Consider a sample placed in an inhomogeneous main field, taken to be parallel to the Bloch sphere's z-axis: $\mathbf{B}_{\text{main}} = (B_0 + \Delta B_0(z))\hat{\mathbf{z}}$, inducing a spatially dependent off-resonance frequency, $\omega_L(z) = \gamma B_0 + \gamma \Delta B_0(z) \equiv \omega_{cs} + \Delta\omega(z)$. As before, assume that the transmitter offset is calibrated such that the inherent chemical shift of the site is 0. If one were to excite the spins with a chirped pulse and acquire an image as shown in Fig. 39, the profile obtained would be distorted: the initial chirp would not create a quadratic phase of the form $a + bz + cz^2$, but rather some intricate phase $\phi_e(z)$, since the non-linearity of $\Delta\omega(z)$ would break the ideal, linear relation between time and position excited in the sample. Furthermore, during acquisition, an additional phase $\Delta\omega(z)t$ would accumulate in addition to the effect of the gradient, $k(t)z$. The total phase of the spins during acquisition will hence be $\phi_a(z,t) = \phi_e(z) + k(t)z + \Delta\omega(z)t$. Invoking the stationary phase approximation (which is still valid) and assuming for simplicity that, even though distorted, the phase of the spins still has a single extremal point, yields:

$$s(t) \propto \int_{-L/2}^{L/2} \rho_0(z) e^{\imath\phi_a(z,t)} dz \approx \frac{\sqrt{2\pi\imath}\rho_0(z_0(t)) e^{\imath\phi_a(z_0(t),t)}}{\sqrt{\left(\frac{d^2\phi_a(z,t)}{dz^2}\right)_{z=z_0(t)}}}. \tag{109}$$

This expression differs for the homogeneous case, Eq. (91), in two fundamental ways:

- The manner in which the image is unraveled is no longer linear, since $z_0(t)$ – the position of the extremal point as a function of time – is no longer a linear function of t, but rather the solution to the complex non-linear equation $\left(\frac{d\phi_a(z,t)}{dz}\right)_{z=z_0(t)} = 0$.
- The voxel size,

$$\delta z = \frac{1}{\sqrt{\left(\frac{d^2\phi_a(z,t)}{dz^2}\right)_{z=z_0(t)}}}, \tag{110}$$

  is no longer constant (even if Eq. (110) reduces to Eq. (92) in the absence of inhomogeneity). This has the effect of distorting (augmenting or diminishing) the signal emanating from each voxel.

Of the two drawbacks outlined above, the first can be fixed by post-processing, using an area-preserving image transformation. But the second can corrupt the image, particularly in those regions in which the signal dephases until disappearing below the noise level, rendering futile any attempt at reconstructing the image by post-processing. In the remainder of this section it will be shown how, given an *a-priori* map of the inhomogeneity $\Delta\omega(z)$, both problems can be resolved without any additional processing, simply via shaping the excitation pulse and the acquisition gradient.

To acquire an undistorted image under the inhomogeneity $\Delta\omega(z)$, two conditions need to be met: the voxel size δz must be

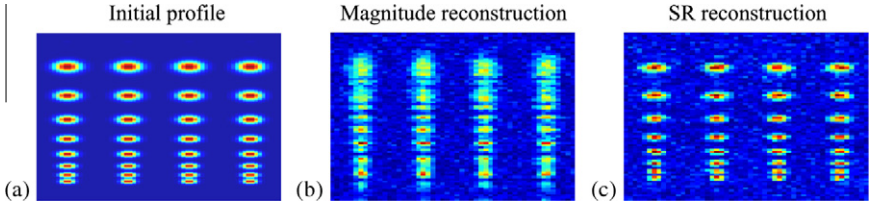

Fig. 44. The ability of the super-resolution algorithm to restore high-definition 2D MR images in the presence of noise. (a) Initial synthetic profile containing the target to be resolved. (b) Image arising from simulating the effects of the sequence illustrated in Fig. 43, to which random noise was added to bring the effective SNR to about 5. Data processing consisted of a 1D FT along the read-out axis, and an | S(t) | modulus calculation of the resulting signal. (c) 2D profile arising upon applying the SR algorithm to the data in (b). Images reproduced from [77].

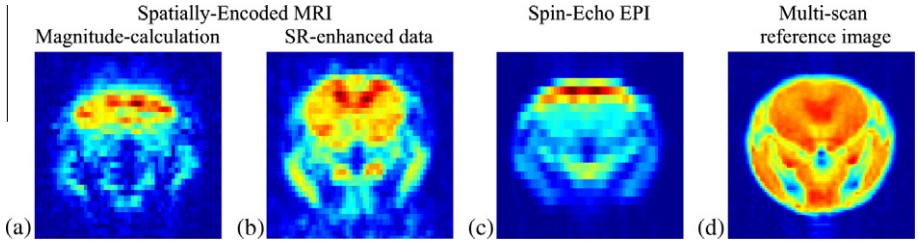

Fig. 45. *In-vivo* scans of a mouse brain (FOV = 15 mm × 15 mm, compared for several pulse sequences. (a) Single-scan hybrid imaging. The sequence is shown in Fig. 43. A 3 ms chirp was used with a 37 kHz/ms sweep rate. The slice selection pulse took 4 ms, with a slice thickness of 0.5 mm. Total acquisition time was 15 ms, resulting in voxel sizes of 0.5 mm along both the spatially and frequency encoded axes. (b) Same as in (A), after employing super-resolved reconstruction along the spatially-encoded axis. (c) Single-scan spin echo EPI (1 mm slice, with voxel sizes of 0.5 mm × 0.65 mm, and a total sequence duration of 24 ms). (d) A reference multi-scan Gradient-Echo image (acquisition time = 30 s). Images reproduced from [77].

time-independent, and the acquisition path $z_0(t)$ must be, as in the homogeneous case, linear with time:

$$z_0(t) = z_{f,e} - \left(\frac{z_{f,e} - z_{i,e}}{T_a}\right)t. \tag{111}$$

Since

$$\frac{d\phi_a(z,t)}{dz} = \frac{d\phi_e(z)}{dz} + k(t) + \frac{d\Delta\omega(z)}{dz}t, \tag{112}$$

$$\frac{d^2\phi_a(z,t)}{dz^2} = \frac{d^2\phi_e(z)}{dz^2} + \frac{d^2\Delta\omega(z)}{dz^2}t, \tag{113}$$

the demand $\delta z = \text{const.}$ can be recast, using Eqs. (113) and (110), as:

$$\left(\frac{d^2\phi_e(z)}{dz^2} + \frac{d^2\Delta\omega(z)}{dz^2}t\right)_{z=z_0(t)} = \frac{1}{\delta z^2} = \text{const.} \tag{114}$$

This furnishes a differential equation for $\phi_e(z)$. Furthermore, demanding that $z_0(t)$ be linear is equivalent to demanding that Eq. (111) be the solution of $\frac{d\phi_a(z,t)}{dz} = 0$. By Eq. (112), that demand can be satisfied by choosing $k(t)$, and hence the acquisition gradient $\gamma G_a(t) = \frac{dk}{dt}$, to be:

$$k(t) = -\left(\frac{d\phi_e(z)}{dz} + \frac{d\Delta\omega(z)}{dz}t\right)_{z=z_0(t)}. \tag{115}$$

This dictates the form of $G_a(t)$. To sum up, one can recover the undistorted image by suitably exciting the sample with the appropriate $\phi_e(z)$ and by shaping the acquisition gradient $G_a(t)$ according to Eqs. (115) and (114). The explicit form of these two quantities will be derived next.

Throughout the acquisition process there is a one-to-one correspondence between the position of a voxel and the time at which it is unraveled: t can thus be considered as a function of z, and Eq. (111) can consequently be inverted to give $t(z) = \frac{T_a}{L_e}(z - z_{f,e})$. Hence:

$$\frac{d}{dt} = \frac{dz}{dt}\frac{d}{dz} = -\frac{L_e}{T_a}\frac{d}{dz}. \tag{116}$$

Based on this, it is possible to recover $\phi_e(z)$ by integrating Eq. (114) twice. Of the two integration constants this demands, one is an overall constant phase and is physically irrelevant; the other can be obtained by recalling that, at the beginning of the acquisition, the phase $\phi_a(z, t = 0)$ – comprised solely of $\phi_e(z)$ at that point in time – will have an extremum at $z = z_{f,e}$:

$$\left(\frac{d\phi_e(z)}{dz}\right)_{z=z_{f,e}} = 0. \tag{117}$$

Using this as a boundary condition, and integrating twice:

$$\phi_e(z) = -\Delta\omega(z)t(z) - \frac{2T_a}{L_e}\int \Delta\omega(z)dz + \frac{(z - z_{f,e})^2}{2\delta z^2} + \frac{T_a\Delta\omega(z_{f,e})}{L_e}z. \tag{118}$$

Treating then $\delta z, T_a, L_e, z_{f,e}$ as given parameters and assuming that the inhomogeneity $\Delta\omega(z)$ has been mapped and is known, Eq. (118) completely determines the desired form of the excitation phase.[23]

To obtain an expression for the acquisition gradient $G_a(t)$, we differentiate Eq. (115) and use Eq. (116):

$$\gamma G_a(t) = \frac{dk(t)}{dt} = -\frac{L_e}{T_a}\left[\frac{d^2\phi_e(z)}{dz^2} + \frac{d^2\Delta\omega(z)}{dz^2}t\right] + \frac{d\Delta\omega(z)}{dz}. \tag{119}$$

Comparing this with Eq. (114), note that the term in the square bracket is constant and equal to $\frac{1}{\delta z^2}$, and hence:

$$\gamma G_a(t) = -\frac{L_e}{T_a\delta z^2} + \frac{d\Delta\omega(z)}{dz}, \tag{120}$$

which yields a closed form solution for $G_a(t)$.

While $G_a(t)$ can be easily shaped using modern hardware according to Eq. (120), it still remains to be shown how one can

[23] It is $\frac{d\phi_e}{dz}$, and not $\phi_e(z)$, which ultimately is physically meaningful (see Eq. (124)), as an additional constant phase has no effect on the relative phasing and dephasing of the spins.

excite a sample with the appropriate phase, given by Eq. (118). To this end a non-linear swept pulse has to be employed which, like a chirped pulse, excites the spins sequentially but no longer in a $z \propto t$ linear fashion. The analysis of such pulses closely follows and generalizes that of Section 2.2.1. Indeed, a chirped pulse is characterized by an instantaneous angular frequency, $\omega_c(t)$, which is related to its phase by $\phi_c(t) = \int_0^t \omega_c(t)dt$. Consider a sample with a spatially dependent off-resonance frequency $\omega_L(z)$, the result of an excitation gradient G_e and some spatial inhomogeneity: $\omega_L(z) = \gamma G_e z + \Delta\omega(z)$. A properly calibrated chirped pulse will excite the spins onto the $\hat{x}\hat{y}$-plane with a phase $\phi_e(z)$. To compute this phase, one can use Eq. (13), which is valid even in the non-linear case; the non-linearity is then implicitly contained in $\omega_L(z)$ and in t_z, the time at which the chirped pulse excites the spin positioned at z.

To infer the desired form of $\omega_c(t)$ and t_z in this inhomogeneous case, we demand that Eq. (13) be equal to the desired phase profile $\phi_e(z)$ given by Eq. (118). Differentiating these equations on both sides yields:

$$\frac{d\phi_c(t_z)}{dz} + \frac{d\omega_L(z)}{dz}(T_e - t_z) - \omega_L(z)\frac{dt_z}{dz} = \frac{d\phi_e(z)}{dz}. \tag{121}$$

where, by the rules of differentiation

$$\frac{d\phi_c(t_z)}{dz} = \frac{d}{dz}\int_0^{t_z} \omega_c(t')dt' = \frac{dt_z}{dz}.\omega_c(t_z). \tag{122}$$

Note that $\omega_c(t_z)$ is the frequency of the chirp at the point in time in which it excites the spin at z, the off-resonance frequency of which is $\omega_L(z)$. Since the chirp excites those spins that match its instantaneous frequency, one must have $\omega_c(t_z) = \omega_L(z)$. Substituting this into Eq. (121) and simplifying, one gets:

$$\frac{d\omega_L(z)}{dz}(T_e - t_z) = \frac{d\phi_e(z)}{dz}. \tag{123}$$

Solving for t_z yields:

$$t_z = T_e - \frac{\frac{d\phi_e(z)}{dz}}{\frac{d\omega_L(z)}{dz}}. \tag{124}$$

This yields the desired form of t_z. Such relation can be inverted, in most cases numerically, to yield z_t, the position in the sample excited at a given time t. This can then be used to determine $\omega_c(t)$, since:

$$\omega_c(t) = \omega_L(z_t). \tag{125}$$

Eq. (125) merely expresses the requirement on the chirp to excite the spins at z_t at time t. All that remains to be done is to properly calibrate the chirped pulse such that all spins will get precisely tipped onto the $\hat{x}\hat{y}$-plane. Using a constant irradiation amplitude as shown in Fig. 4a will not suffice, as the non-linear sweep of the pulse means different regions in the sample will be affected for different amounts of time. Eq. (15), though, remains valid, provided the constant rate R is generalized to $\frac{d\omega_c}{dt}$, the *instantaneous rate*.[24] Fig. 46 presesnts an experimental example of how those considerations can restore the integrity of a NMR image.

5.4.2. Generalization to higher dimensions

The techniques outlined in Section 5.4.1 can be generalized to higher dimensions, with a few caveats. Assuming the spins have been excited onto the $\hat{x}\hat{y}$-plane with a phase $\phi_e(\mathbf{r})$, they will accumulate a phase $\phi_a(\mathbf{r},t) = \phi_e(\mathbf{r}) + \mathbf{k}(t)\cdot\mathbf{r} + \Delta\omega(\mathbf{r})t$ throughout acquisition. In two dimensions the acquired signal will be:

$$s(t) = \int \rho_0(\mathbf{r})e^{\imath\phi_a(\mathbf{r},t)}d\mathbf{r} \approx \frac{2\pi\imath\rho_0(\mathbf{r}_0(t))e^{\imath\phi_a(\mathbf{r}_0(t),t)}}{\sqrt{\det(H)_{\mathbf{r}=\mathbf{r}_0(t)}}}, \tag{126}$$

where $\mathbf{r}_0(t)$ is the trajectory of the stationary point, given implicitly by $(\nabla\phi_a(\mathbf{r},t))_{\mathbf{r}=\mathbf{r}_0(t)} = 0$. H is the Hessian of $\phi_a(\mathbf{r},t)$, as evaluated along $\mathbf{r}_0(t)$:

$$H(\mathbf{r}) = \begin{pmatrix} \partial_{xx} & \partial_{xy} \\ \partial_{yx} & \partial_{yy} \end{pmatrix}\phi_a(\mathbf{r},t) = \begin{pmatrix} \partial_{xx} & \partial_{xy} \\ \partial_{yx} & \partial_{yy} \end{pmatrix}(\phi_e(\mathbf{r}) + \Delta\omega(\mathbf{r})t). \tag{127}$$

As with the one-dimensional case, artifacts will be introduced into the image via two routes: The acquisition trajectory $\mathbf{r}_0(t)$ might deviate from the ideal, and the pixel size

$$\delta V \equiv \frac{2\pi}{\sqrt{\det(H)_{\mathbf{r}=\mathbf{r}_0(t)}}}, \tag{128}$$

might be time-dependent. Fortunately, the approaches for correcting them outlined for the one-dimensional experiment (Section 5.4.1) are applicable here as well: to force a particular trajectory $\mathbf{r}_0(t)$, the acquisition gradients $\mathbf{G}_a(t)$ must be shaped, and to ensure δV is time independent, the excitation phase $\phi_e(x,y)$ must be tailored accordingly.

Assuming $\phi_e(\mathbf{r})$ has been computed, the first requirement is straightforward to implement, by demanding $\mathbf{r}_0(t)$ is the stationary point of $\phi_a(\mathbf{r},t)$ for all t:

$$(\nabla\phi_a(\mathbf{r},t))_{\mathbf{r}=\mathbf{r}_0(t)} = 0. \tag{129}$$

$\mathbf{k}(t)$ can be solved for explicitly by substituting $\phi_a(\mathbf{r},t) = \phi_e(\mathbf{r},t) + \mathbf{k}(t)\cdot\mathbf{r} + \Delta\omega(\mathbf{r})t$, giving

$$\mathbf{k}(t) = -[\nabla\phi_e(\mathbf{r} + \nabla\Delta\omega(\mathbf{r})t]_{\mathbf{r}=\mathbf{r}_0(t)}. \tag{130}$$

As all quantities on the RHS are known, $\mathbf{k}(t)$ can be determined in closed form via straightforward differentiation. Furthermore, $\phi_e(\mathbf{r})$ can be found by demanding that δV (Eq. (128)), which depends on $\phi_e(\mathbf{r})$ implicitly, be constant. Unlike the one-dimensional case, in which there exists a 1–1 relation between time and position (Eq. (116)), iterative numerical schemes must be employed in the general case to find $\phi_e(\mathbf{r})$. An analytical solution is, however, possible for some cases [11]. Fig. 47 shows an experimental example of such an instance.

5.5. Signal-to-noise and noise filtering in SPEN MRI

An important feature to compare is the signal to noise ratio of conventional Fourier imaging against SPEN MRI. This will be discussed using the case of 1D image acquisition as a framework. As with the spectroscopic case (Section 3.3.4), we shall assume some statistically random and additive noise $n(t)$ to be present in addition to the signal $s(t)$ originating from the spins. The SNR is defined as

$$\mathrm{SNR} \equiv \frac{s_{\mathrm{rms}}}{n_{\mathrm{rms}}}. \tag{131}$$

The subscript rms stands for root-mean-square, and for a signal $f(t)$ of duration T is defined as $f_{\mathrm{rms}} \equiv \sqrt{\frac{1}{T}\int_0^T |f(t)|^2 dt}$. Comparing the SNRs of both SPEN MRI and FT imaging involves the computation of the quantity:

$$\frac{\mathrm{SNR}^{(\mathrm{SPEN\ MRI})}}{\mathrm{SNR}^{(\mathrm{FT})}} = \frac{s_{\mathrm{rms}}^{(\mathrm{SPEN\ MRI})}}{s_{\mathrm{rms}}^{(\mathrm{FT})}} \times \frac{n_{\mathrm{rms}}^{(\mathrm{FT})}}{n_{\mathrm{rms}}^{(\mathrm{SPEN\ MRI})}}. \tag{132}$$

It is often the case in imaging that one is interested in the signal to noise per voxel. For a meaningful comparison the field-of-view (FOV) and the voxel size (δz) will be taken to be the same in both experiments: $\delta z^{(\mathrm{SPEN\ MRI})} = \delta z^{(\mathrm{FT})} \equiv \delta z, \mathrm{FOV}^{(\mathrm{SPEN\ MRI})} = \mathrm{FOV}^{(\mathrm{FT})} \equiv L$.

[24] This reduces to R in the case of a linear chirp.

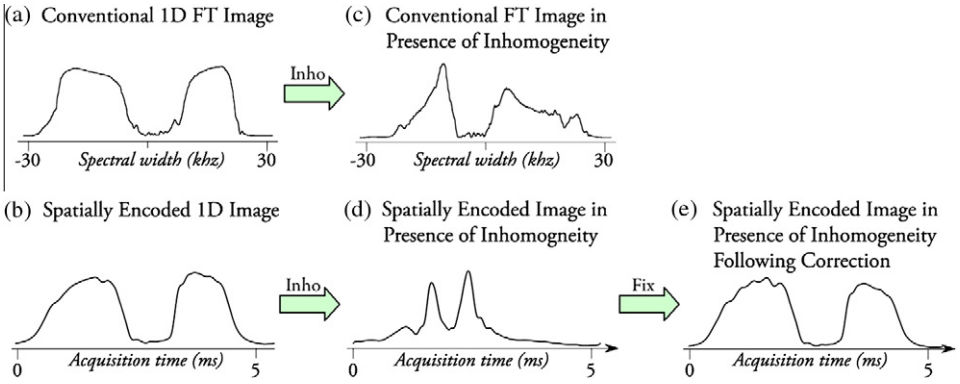

Fig. 46. 1D spatially-encoded imaging in inhomogeneous fields: experimental results. All experiments were carried out on a 500 MHz iNova NMR spectrometer. The sample is described in Fig. 41. (a and b) FT and spatially-encoded profiles collected from the phantom under conditions similar to those detailed in that figure: 5 G/cm excitation and acquisition gradients, 10 ms average free-evolution times, 18.5 mm long samples, etc. (c and d) As in (a and b), but upon subjecting on the sample to an artificial $\Omega_{\text{inh}} = 1.31z + 0.193z^2$ kHz (with z the displacement away from the sample's center in mm). This inhomogeneity was introduced by distorting the z, z^2 magnet shims, and was characterized by mapping the water resonance using a simple gradient-echo sequence. (e) Idem as in (d) but after inserting the mapped inhomogeneity profile into the algorithm described in the text, recalculating from it the correcting RF sweep and acquisition gradient patterns, and applying these for the acquisition of the data. The most remarkable feature of this compensation procedure (and therefore a basic test of its correct functioning) is that it enabled the signal to endure in the time-domain, long after either the conventional k-space or its analogous spatially-encoded signal have both decayed into the background noise. This, in spite of Ω_{inh} spanning over 25 kHz and of the experiment still requiring $G_e = 5$ G/cm, and an average $G_a = +4.13$ G/cm over the acquisition. Notice that although still not ideal, the wiggles exhibited by this experimental Ω_{inh}-compensated profile are akin to those of its homogeneous counterpart in (b). Simulations indicate that these reflect in both cases limitations of the chirped excitation pulse in delivering the desired profile, rather than in an actual failure of the compensation procedure.

Letting $k_{\max}^{(\text{SPEN MRI})} \equiv \gamma G_a^{(\text{SPEN MRI})} T_a^{(\text{SPEN MRI})}$, $k_{\max}^{(\text{FT})} \equiv \gamma G_a^{(\text{FT})} T_a^{(\text{FT})}$ and equating voxel sizes, one obtains $\sqrt{\frac{L}{k_{\max}^{(\text{SPEN MRI})}}} = (k_{\max}^{(\text{FT})})^{-1}$, or simply:

$$k_{\max}^{(\text{SPEN MRI})} = N k_{\max}^{(\text{FT})}, \tag{133}$$

where $L \times k_{\max}^{(\text{FT})} = N$ is the number of voxels – the same in both experiments. The experimental acquisition time T_a will be taken to be equal in both cases, so as to equalize the effects of relaxation; hence, Eq. (133) becomes

$$G_a^{(\text{SPEN MRI})} = N G_a^{(\text{FT})}. \tag{134}$$

Since $G_a^{(\text{SPENMRI})} > G_a^{(\text{FT})}$, one must use a larger filter bandwidth during SPEN MRI; and since the noise level increases as the square root of the filter bandwidth:

$$\frac{n_{\text{rms}}^{(\text{FT})}}{n_{\text{rms}}^{(\text{SPEN MRI})}} = \sqrt{\frac{G_a^{(\text{FT})}}{G_a^{(\text{SPEN MRI})}}} = \frac{1}{\sqrt{N}}. \tag{135}$$

Signal levels can be similarly compared. From Eq. (91), the rms signal in a single voxel is $|s_{\text{rms}}^{(\text{SPEN MRI})}| \propto M_0(z_0(t))\delta z^{(\text{SPEN MRI})}$ up to some proportionality constant which depends on the receiver geometry and electronics (and is hence shared by both experiments). It can be similarly shown [68] that for a single voxel $|s_{\text{rms}}^{(\text{FT})}| \propto M_0(z)\delta z^{(\text{FT})}$. Since voxel sizes have been chosen to be equal, $s_{\text{rms}}^{(\text{FT})} = s_{\text{rms}}^{(\text{SPEN MRI})}$, and as a result

$$\frac{\text{SNR}^{(\text{SPEN MRI})}}{\text{SNR}^{(\text{FT})}} = \sqrt{\frac{1}{N}}. \tag{136}$$

That is, spatial encoding suffers a $\sqrt{N}$ reduction in its SNR compared to Fourier imaging, where N is the number of voxels. This, however, can be remedied and brought up-to-par by suitable post-processing. In what follows, we shall assume that the magnitude $|s(t)|$ of the acquired SPEN MRI signal, which is proportional to the image, will be used; any phase information will be considered superfluous. It will also be convenient to employ the time-axis instead of the spatial z-axis to describe the procedure. For the sake of simplicity, the treatment will remain confined to the one-dimensional case.

In the beginning of an experiment, the filter bandwidth of the NMR receiver needs to be properly set. If set too high, and excessive noise will be introduced into the signal, whereas if set too low, relevant frequencies will be filtered out. For SPEN MRI, the range of essential frequencies is determined by the difference in frequencies between the first and last voxels, situated at $\pm\frac{L}{2}$. The spatially dependent off-resonance frequency, $\omega_L(z) = \gamma G_a z$, dictates this difference to be $\omega_L(+\frac{L}{2}) - \omega_L(-\frac{L}{2}) = \gamma G_a L$; thus one must set $\text{fbw} = \gamma G_a L$, which then sets the acquisition dwell time to $\frac{1}{\text{fbw}}$.

The main insight into reducing noise levels is shown in Fig. 48: while $\text{fbw} = \gamma G_a L$, the actual signal emanates from a small region of width δz, equal to the voxel size; all other spins are dephased by the rapidly changing quadratic phase. Since noise levels in the sample are proportional to $\sqrt{\text{fbw}}$, it would be desirable to reduce fbw from $\gamma G_a L$ by a factor of N to $\gamma G_a \delta z$. In principle, this is not possible, since the instantaneous frequencies of the voxels will span the entire range $\gamma G_a L$ throughout the acquisition. There is, however, no imaging information encoded in this frequency spread. By suitable post-processing it is thus possible to localize the voxels in frequency space into a narrow band of frequencies of width $\gamma G_a \delta z$, while filtering out the extraneous noise outside it.

The filtering process shown schematically in Fig. 49, and the ensuing SNR gains, can be understood as follows: the SPEN MRI image is the sum of noise and of the coherent signal of the image. Spectrally, the noise is white and spans a range of frequencies given by the fbw. However, the signal being sought, whose characteristic scale of change of which is set by the voxel size δz, spans a much smaller range of frequencies. Denoting by δt the smallest time-scale associated with the image (see Fig. 49a), it follows that the FT of the coherent signal of the image then occupies a region not any larger than $\frac{1}{\delta t}$. Since the z and t axes are linearly related in 1D SPEN MRI, δt is proportional to the voxel size. In fact,

$$\frac{T_a}{\delta t} = \frac{L}{\delta z} = N, \tag{137}$$

where N is the number of voxels, and so, using Eq. (105):

$$\frac{1}{\delta t} = \frac{\gamma G_a L}{N} = \frac{\text{fbw}}{N}. \tag{138}$$

With this insight, a filtering procedure to optimize the SPEN SNR becomes straightforward: Any noise outside of a spectral width $\frac{1}{\delta t}$ should be removed via a windowing-function (Fig. 49c) and the resulting filtered spectrum should be Fourier transformed back to the time-domain (Fig. 49d) to retrieve the desired, filtered image.

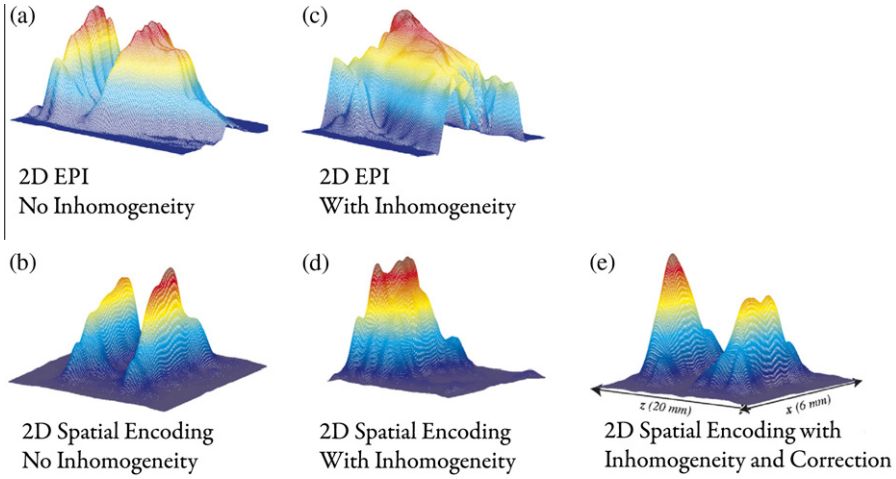

Fig. 47. 2D spatially-encoded imaging in inhomogeneous fields: experimental results. The images were obtained on the same phantom sample used in Figs. 46 and 41. (a) Single-scan 2D FT EPI image recorded using a blipped read-out of 32 echoes spread over 32 ms; acquisition gradients were $G_y = \pm 15$ G/cm, $G_x = 0.85$ G/cm (see Fig. 35) (pulsed over 50 μs every 950 μs). (b) Single-scan 2D spatially-encoded image collected using a zigzagging scheme as in Fig. 42 with $G_y = \pm 15$ G/cm, $G_x = 0.85$ G/cm, $N_y = 16$ and an excitation gradient of 4 G/cm. (c and d) Idem as in (a and b) but upon subjecting the sample to the artificial inhomogeneity $\Omega_{\text{inh}}(z) = 0.023z^2 + 0.025z$. (e) Idem as in (d), after applying the correction algorithm described in the text.

As the spectral components of the coherent time-domain signal of the image are not disturbed, the image quality is preserved, while the noise's bandwidth is decreased by a factor of N. The gain in SNR afforded by the filtering procedure is due to the reduction in the noise level: The filter bandwidth has been effectively truncated by a factor of N. Since the noise scales as $\sqrt{\text{fbw}}$, this implies a gain of $\sqrt{N}$ in the SNR. Note that, by Eq. (136), this renders the SNR of SPEN MRI comparable to that of Fourier-based imaging methods.

6. Spectroscopic aspects of ultrafast MRI and spatial aspects of ultrafast 2D NMR

Spatially encoded 2D NMR and MRI share a common reliance on frequency-swept pulses, applied in the presence of field gradients so as to encode the spin interactions. It turns out that, as a result of this, spatially-encoded images carry within them spectroscopic information, and spatially-encoded spectra also carry the image of the spins in the sample. In both cases, the complementary spectral/spatial information arises at no extra cost in the experimental complexity: it simply resides in the signal, whether we are interested in it or not. The extraction of this additional information is the topic of the current section. First, in Section 6.1 it will be examined how one can extract different images from differing chemical sites, a problem known as *chemical shift imaging* (CSI). In Section 6.1.1 it will be shown that hybrid imaging (see Section 5.3) can be used to carry out a CSI experiment in n-dimensions. The extension of those ideas to cases involving inhomogeneous B_0 fields will be briefly touched upon in Section 6.1.2. Following the discussion of CSI, in Section 6.2 the inverse problem will then be studied, namely, the extraction of a two-dimensional spectrum of a sample by imaging that sample. This leads to a UF2DNMR spectroscopy method based on a *single-sweep* of the spins.

6.1. Chemical shift imaging

This section builds upon the concepts introduced in Section 5.5, and shows how the phase of a SPEN MRI $s(t)$ signal can be utilized to spectrally separate images stemming from media with different chemical shifts, such as fat and water in tissues. This could allow for the *chemical shift imaging* (CSI) [69,39,70] of all sources in the sample, using post-processing to reconstruct the multidimensional images arising from every chemical site, simultaneously and within a single-scan. SPEN MRI is particularly well suited to accomplish this, as it does not require a modification of the original pulse sequence – it only requires using the hitherto disregarded phase of the signal. This is unlike EPSI-type techniques used in Fourier-based spectroscopic imaging, which require introducing an additional alternation of the gradient (and hence an additional dimension [39]), in order to spectrally resolve each peak of interest. In this section, the chemical shift ω_{cs} will no longer be assumed zero. Starting for simplicity with the one-dimensional case, generalizations to more dimensions will be presented later.

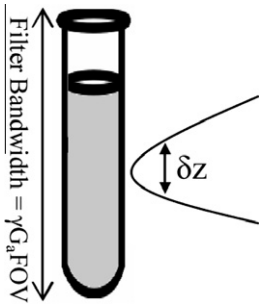

Fig. 48. In SPEN MRI, the filter bandwidth must be set to cover the entire sample, $\gamma G_a L$, since the instantaneous frequency of each voxel varies throughout acquisition, from $-\frac{\gamma G_a L}{2}$ to $\frac{\gamma G_a L}{2}$. However, at each instant, only a small range of frequencies – those originating from within the current voxel δz – comprise the signal.

The phase of the spins following a $\frac{\pi}{2}$-chirped pulse is given by Eq. (14). If one were to acquire now the signal while applying a gradient G_a, the stationary point $z_0(t)$ would follow a trajectory defined by: $\frac{d}{dz}[\phi_e(z) + \gamma G_a t z + \omega_{cs} t]_{z=z_0(t)} = 0$. Setting $R \equiv \frac{\text{ExcitedFrequencyRrange}}{2\pi T_e} = \frac{\gamma G_e L}{2\pi T_e}$, $G_a T_a = -G_e T_e$, and then solving for $z_0(t)$, one obtains:

$$z_0(t) = \frac{L}{2}\left(1 - \frac{2t}{T_a}\right) - \frac{\omega_{cs}}{\gamma G_e}. \tag{139}$$

We see that the effect of the chemical shift is to slightly shift the acquired region by an amount $\Delta z = \frac{\omega_{cs}}{\gamma G_e}$ (compare Eq. (139) and (90)); for typical numbers, such as $G_e = 1$ G/cm and a 100 Hz chemical shift, this would imply a shift of approximately 0.2 mm for protons.

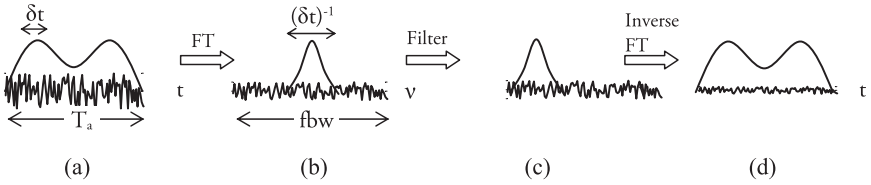

Fig. 49. Noise filtering in SPEN MRI. (a) The original signal with noise. δt signifies the voxel size along the time axis, which is proportional to the spatial z-axis. (b) The Fourier transform of the signal in (a). The noise occupies a much larger band of frequencies (given by fbw) when compared to the band occupied by the signal, δt^{-1}. (c) By filtering out the noise, the effective filter bandwidth is truncated from $\gamma G_a L$ to δt^{-1}. (d) Fourier transforming backwards, the image remains unharmed while the noise levels drop by a factor of $\sqrt{\frac{\gamma G_a L}{\delta t^{-1}}} = \sqrt{N}$, where N is the number of voxels.

On the other hand, using Eq. (139) to evaluate $\phi_a(z_0(t),t)$, the phase of the collected signal, one obtains:

$$\phi_a(z_0(t),t) = \left[\left(\frac{\gamma G_e T_e L}{2T_a^2}\right)t^2 - \left(\frac{\gamma G_e T_e L}{2T_a}\right)t\right] + \left(1+\frac{T_e}{T_a}\right)\omega_{cs}t. \quad (140)$$

This $\phi_a(z_0(t),t)$ separates naturally into two components: One that is independent of the chemical shift and one that depends linearly on it. The chemical-shift independent phase is shared by all spins, regardless of their chemical shift, and can be removed by multiplying the total signal by the negative of the phase, $e^{-\imath(\cdots)}$. The remaining term, $\left(1+\frac{T_e}{T_a}\right)\omega_{cs}t \equiv \Delta\nu t$, modulates the signal by an effective offset $\Delta\nu$.

Consider next the acquisition of such a signal, assuming it originates from a sample containing q different chemical sites, $\omega_{cs}^{(1)}, \omega_{cs}^{(2)}, \ldots, \omega_{cs}^{(q)}$, each characterized by a different spin density $\rho_0^{(1)}(z), \rho_0^{(2)}(z), \ldots, \rho_0^{(q)}(z)$. Neglecting the small dependence of on the chemical shift of $z_0(t)$ noted in Eq. (139), the acquired signal can be expressed as $s(t) \propto \sum_{p=1}^{q} \rho_0^{(p)}(z_0(t)) e^{\imath\phi_a(z_0(t),t)}$. Phase correcting this signal can remove the above-mentioned phase terms common to all sites, yielding:

$$s(t) \propto \sum_{p=1}^{q} \rho_0^{(p)}(z_0(t)) e^{\imath\Delta\nu_p t}, \quad (141)$$

where $\Delta\nu_p \equiv \left(1+\frac{T_e}{T_a}\right)\omega_{cs}^{(p)}$. The result of such a global "phase correction" is akin to the frequency demodulation introduced in Section 5.5. Recall, from that discussion, that the spectral width of the Fourier transform of the image (given by $|s(t)|$), is given by the inverse of the dwell time, chosen to be the filter-bandwidth, $\mathrm{fbw} = \gamma G_a L$; hence, the image's frequency components occupy a region of size $\gamma G_a \delta z \equiv \frac{1}{\delta t}$ in frequency space (Eq. (138), Fig. 49). The Fourier transform of Eq. (141) merely results in the same spectral content for each site p, shifted by an offset $\Delta\nu_p$. The filtering procedure assumes that this shift is larger than $\frac{1}{\delta t}$, so the spectral contents originating from different chemical sites do not overlap. Under this assumption, the spectral contents of each site $s^{(p)}(t)$ are distinct, and can be singled out via a Fourier transform of the spatially encoded FID. Then, by applying a windowing-function to the resulting spectrum and eliminating all spectral components originating from $s^{(k)}(t), k\neq p$, one can isolate the response from each chemically-shifted site. Fourier transforming back to the time-domain retrieves only that part of the image originating from the pth spectral peak: $\rho_0^{(p)}(z)$. The procedure is outlined in Fig. 50 for the case of two chemical sites, $\omega_{cs}^{(1)}, \omega_{cs}^{(2)}$, and its net effect is the delivery of a set of chemical shift resolved images.

The maximum resolving power of this spectroscopic imaging method – that is, the closest two chemical shifts it can successfully separate – can be estimated by demanding that the shift $\Delta\nu$ be larger than the width of the spectral region occupied by each image, $\frac{1}{\delta t}$. This leads to:

$$\Delta\omega_{cs} \geqslant \frac{\mathrm{fbw} T_a}{N(T_a+T_e)}. \quad (142)$$

Taking, as an example, $T_e = 20$ ms, $T_a = 0.2$ s, $G_e = 0.2$ Gauss/cm, $L = 5$ cm, one finds $\delta z = 5$ mm and $\Delta\omega_{cs} \geqslant 0.5$ kHz.

6.1.1. Hybrid chemical shift imaging

The notions just presented can be generalized to nD imaging by employing either full nD spatial encoding, or hybrid imaging approaches [12]. We cover here the latter case (illustrated in Fig. 43). Fig. 51a illustrates for completeness the 2D data set resulting from such an experiment: its rows are Fourier-encoded, while its columns are spatially encoded. By treating the columns as one-dimensional imaging experiments it is possible to apply the same post-acquisition processing described for a 1D case; the remainder of this section formalizes this notion for the 2D case.

The acquisition phase of the spins as a function of position can be written, for a 2D hybrid SPEN MRI experiment, as:

$$\phi_a(x,y,t) = \underbrace{\left[\phi_e^{(x)}(x) + k_x(t)x\right]}_{\phi_a^{(x)}(x,k_x)} + \underbrace{\left[\phi_e^{(y)}(y) + k_y(t)y\right]}_{\phi_a^{(y)}(y,k_y)} + \omega_{cs}t, \quad (143)$$

where $\phi_e^{(x)}, \phi_e^{(y)}$ are the phases encoded along the x- and y-axes prior to acquisition. As the x-axis is Fourier-encoded, $\phi_e^{(x)}(x) = -\frac{\gamma G_a \Delta T_{a,x} x}{2}$ is the linear phase created by the gradient just prior to acquisition; $\phi_e^{(y)}(y)$ is the quadratic phase induced by the chirp, as given by Eq. (14) with z replaced by y. The acquired signal is:

$$s(t) = \int\int dxdy \rho_0(x,y) e^{\imath\left[\phi_e^{(x)}(x)+k_x x\right]+\imath\left[\phi_e^{(y)}(y)+k_y y\right]+\imath\omega_{cs}t}, \quad (144)$$

where the time-dependence of k_x, k_y has now been made implicit. Since $\phi_e^{(y)}(y)$ is quadratic, y can be integrated over by employing the stationary phase approximation, while treating x, t, k_x, k_y as constants:

$$s(t) = \sqrt{2\pi\imath} e^{\imath\phi_a^{(y)}(y_0(k_y),k_y)} e^{\imath\omega_{cs}t} \delta y \int dx e^{\imath\left[\phi_e^{(x)}+k_x x\right]} \rho_0(x, y_0(k_y)), \quad (145)$$

where δy is the voxel size along the spatially-encoded axis as given by Eq. (92) (for z), and $y_0(k_y) \equiv y_0(k_y(t))$ is the position of the stationary point as a function of[25] k_y, obtained by solving the following equation, $\frac{d\phi_a^{(y)}}{dy} = 0$:

$$y_0(k_y) = y_{\text{initial}} + \left(\frac{L_y}{\gamma G_e T_e}\right)k_y, \quad (146)$$

$$y_{\text{initial}} = \frac{L_y}{2} - \frac{\omega_{cs}}{\gamma G_e}. \quad (147)$$

[25] The stationary point equation, $\frac{d\phi_a^{(y)}}{dy} = 0$ does not contain time explicitly, and hence the time-dependence of the stationary point enters only implicitly, via its dependence on $k_y(t)$. In the 2D case, the stationary point y_0 retains its linearity in k_y, even though it is no longer linear in time.

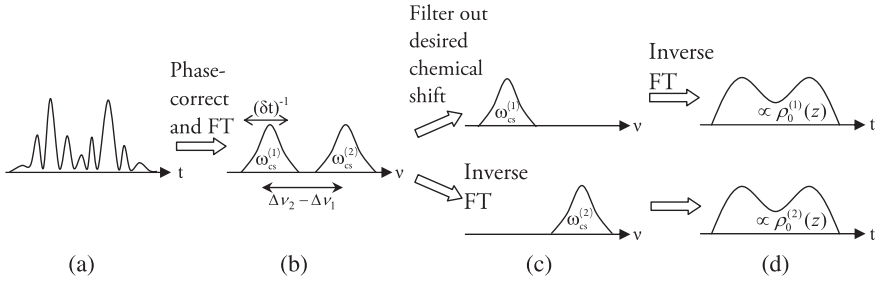

Fig. 50. Spatially-encoded chemical shift imaging. The signal shown in (a) is the sum of two signals $s(t) = s^{(1)}(t) + s^{(2)}(t)$, originating from two different chemical shifts, $\omega_{cs}^{(1)}$ and $\omega_{cs}^{(2)}$. According to Eq. (91), the signals are of the form $s^{(p)}(t) \propto \rho_0^{(p)}(z_0(t))e^{i\phi_a(z_0(t),t)}$, where $\rho_0^{(1)}(z), \rho_0^{(2)}(z)$ are the spin densities being imaged and $z_0(t)$ is the acquisition path, given by Eq. (139). After removing those parts of the phase that are shared by both components – that is, those parts which are independent of the chemical shift (see Eq. (140)) – the signal becomes $s(t) \propto \rho_0^{(1)}(z_0(t))e^{i\Delta\nu_1 t} + \rho_0^{(2)}(z_0(t))e^{i\Delta\nu_2 t}$, where $\Delta\nu_p = \left(1 + \frac{T_e}{T_a}\right)\omega_{cs}^{(p)}$. (b) The signal is Fourier transformed. The Fourier transform of each spin density $\rho_0^{(p)}(z)$ occupies a region $\frac{1}{\delta t}$, the width of which is determined by the voxel size. The two regions are separated by $\Delta\nu_2 - \Delta\nu_1 = \left(1 + \frac{T_e}{T_a}\right)(\omega_{cs}^{(2)} - \omega_{cs}^{(1)})$. By filtering out a particular region (c), the spectral contents of a particular signal $s^{(p)}(t)$ $(p = 1, 2)$ can be singled out. All that remains at this point is to Fourier transform back to the time-domain (d), which is proportional to the image domain and hence to $\rho_0^{(p)}(z)$.

The coordinates of the qth point in the set $0, 1, 2, \ldots$ in Fig. 51a are

$$k_{y,q} = 2q\gamma G_{a,y}\Delta T_{a,y}, \tag{148}$$

$$y_q = y_{\text{initial}} + \frac{2q\gamma G_{a,y}\Delta T_{a,y}L_y}{\gamma G_e T_e}, \tag{149}$$

$$t_q = t_0 + 2q(\Delta T_{a,y} + \Delta T_{a,x}), \tag{150}$$

and hence the phase $\phi_q \equiv \phi_a^{(y)}(y_q, k_{y,q}) + \omega_{cs}t_q$ of the qth point is:

$$\phi_q = \frac{2\gamma G_{a,y}^2 \Delta T_{a,y}^2 L_y}{G_e T_e} q^2 + \gamma G_{a,y}\Delta T_{a,y} q + \left[\left(1 - \frac{G_{a,y}}{G_e}\right) + \Delta T_{a,x}\right] 2q\omega_{cs} + t_0\omega_{cs}. \tag{151}$$

Eq. (151) is a discretized 2D analog of Eq. (140). The terms that are independent of ω_{cs} are shared by all points and can be removed using post-processing, while the part proportional to ω_{cs} is linear in q. A particular chemical shift can be singled out by Fourier transforming each row, filtering out the desired peak and transforming back.

An experimental example of this procedure is outlined Fig. 52. This was carried out on a sample containing HDO and $CHCl_3$, which form two immiscible liquid phases. By phase-correcting, Fourier transforming, filtering the data for each peak along the spatially-encoded axis, and making an inverse FT, the 2D image arising from each chemical compound can be recovered – all of this while still preserving the single-scan nature of the experiment.

6.1.2. Single-scan spectroscopic imaging in inhomogeneous fields

Chemical shift imaging is severely challenged by inhomogeneous fields, as variations in the magnetic field will often overshadow the differences in chemical shifts, which tend to be much smaller in magnitude. It is generally impossible to implement spectroscopic imaging acquisitions in a single-scan under inhomogeneous conditions. Equally challenged is the spatially encoded method: an attempt to acquire such a spectroscopic imaging data set containing DMSO and HDO under severe B_0 distortions is shown in Fig. 53, where it is seen that phase-correcting and Fourier transforming the resulting signal does not yield any meaningful peaks in frequency space. However, the ability of SPEN MRI to acquire images in inhomogeneous fields can be combined with its ability to spectrally differentiate between images, to resolve this challenge. Indeed, it was shown in Section 5.4.1 how, by tailoring the phase profile of the excitation RF and the acquisition gradients, one can acquire an image in the presence of a non-ideal B_0 field, assuming the chemical shift Ω was set to zero. The effects of introducing a non-zero chemical shift on both excitation and acquisition will now be examined in more detail, and methods to compensate for these effects will be shown.

During acquisition, the phase of the spins that we shall now consider will be given by:

$$\phi_a(z, t_2) = \phi_e(z) + k(t_2)z + \Delta\omega(z)t_2 + \Omega_2 t_2. \tag{152}$$

On the one hand, the position of the stationary acquisition point is unaffected by the chemical shift Ω_2, as it is found by differentiating $\phi_a(z, t_2)$ according to z (Eq. (112)), which is independent of the $\Omega_2 t_2$ term. On the other hand, the presence of a chemical shift Ω_1 during excitation entangles the position z and time t_1. When computing the chirp frequency, $\phi_c(t)$, in our preceding treatment of field inhomogeneity, the assumption was made that $\Omega_1 = 0$. However, the actual phase created by a chirped $\frac{\pi}{2}$ excitation pulse is given by Eq. (13), in which $\omega_e(z)$ is dependent on the chemical shift: $\omega_e(z) = \gamma G_e z + \Delta\omega(z) + \Omega_1$. Thus, the phase given by Eq. (13) would have an additional $\Omega_1(T_e - t_z)$ term added to it, where t_z, given by Eq. (124), is a non-linear function of z. This additional term, which dephases the spins during acquisition, is chemical-shift dependent and cannot be eliminated using a single $\frac{\pi}{2}$ excitation chirp, even by varying its instantaneous frequency non-linearly. The approaches introduced in Section 5.4 to compensate for ΔB_0 will fail when dealing with multiple chemical sites. The essence of this problem stems from the fact that using just one $\frac{\pi}{2}$ chirped pulse affords a single degree of freedom, and yet there are two constraints now to fulfill. (i) The phase $\phi_e(z)$ must be chosen such that the voxel size (Eq. (110)) remains constant throughout acquisition, and (ii) that part of the phase $\phi_e(z)$ which is dependent on the chemical shift Ω_1 must be made linear when evaluated along the acquisition trajectory $z_0(t)$ (Eq. (111)). Since $z_0(t)$ is linear in t, the second condition is equivalent to demanding that the coefficient of Ω_1 in $\phi_e(z)$be linear in z. The solution to this dilemma is to introduce an additional degree of freedom; for instance, employing a second refocusing π-chirp. With this additional degree of freedom, one can satisfy both constraints. The reader is referred to reference [12] for the technical details. The results are reproduced here, carried out on the same sample used in Fig. 53. These results (Fig. 54) demonstrate the excellent spectral resolution and spatial definition that two modulated RF-driven encodings can provide, satisfying both constraints and yielding individual images from the different chemical sites.

6.2. Single-sweep imaging-derived 2D NMR spectroscopy

Section 6.1 discussed a chemical shift imaging approach, entailing the extraction of multidimensional images corresponding to

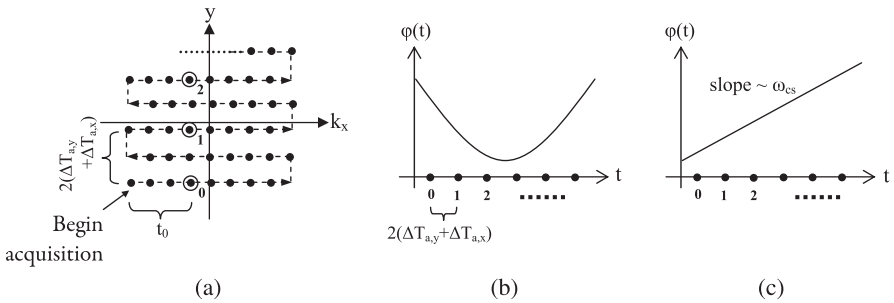

Fig. 51. Hybrid chemical shift imaging (see Fig. 43 for pulse sequence). (a) Each spatially encoded column (the circled points $0, 1, 2, \ldots$) can be treated as a one-dimensional experiment with a dwell time of $2(\Delta T_{a,x} + \Delta T_{a,y})$. For simplicity, assume only the positive rows are used, although the same arguments can be easily applied when using both negative and positive rows. (b) The phase of each column is quadratic when plotted as a function of q, the index of the points, with the quadratic term independent of the chemical shift. (c) By removing the quadratic term, the remaining set of points will have a phase linear in both k and the chemical shift, ω_{cs}. At this point, the techniques described previously in, e.g., Fig. 50, can be applied directly.

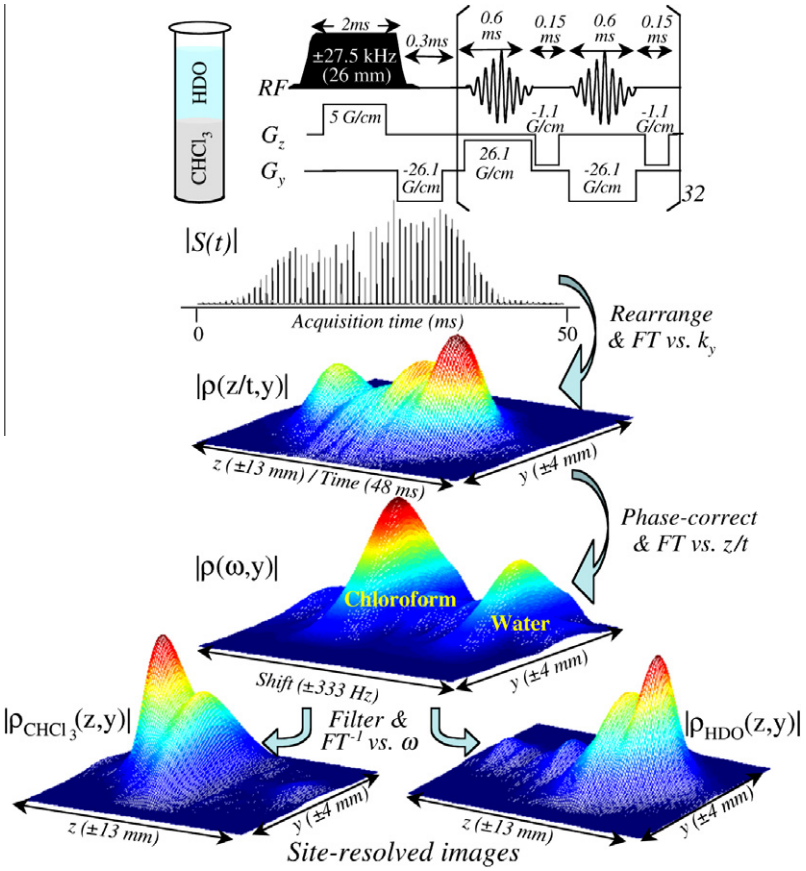

Fig. 52. Hybrid chemical shift imaging, carried out on a sample of $CHCl_3$ and HDO, which form two exclusive phases within the 5 mm NMR sample. The signals from both sides can be seen to interfere irregularly. Once rearranged, phase corrected and Fourier transformed over both axes, the individual spectral peaks, corresponding to each of the compounds, can be clearly seen. By filtering out one or the other and Fourier transforming back along the spatially-encoded axis, the signal originating from each can be computed and the corresponding image reconstructed.

different 1D spectroscopic lines in a sample. This section is concerned with the opposite endeavor, namely, to the extraction of 2D spectroscopic data from a spatially-encoded imaging experiment, also within a single-scan. As before, use is here made of the information contained in the phase of a signal stemming from the spatially encoded spin ensemble.

The main ideas underlying this alternative approach to UF2DNMR are summarized in Fig. 55. In Section 6.1 it was shown how one could extract a 1D spectrum from a spatially-encoded image, acquired in the presence of an acquisition gradient. The positions of the spectral peaks were determined by the excitation pulse; within the context of a 2D NMR experiment, the spectrum thus obtained reflects the peaks along the indirect-domain, Ω_1. By repeatedly alternating the acquisition gradient, the modulation of the image imposed by a second, direct-domain chemical shift Ω_2 can become observable along the direct t_2 axis. These notions can be recast in mathematical terms. Following a chirped $\frac{\pi}{2}$ excitation, the phase of the spins in the $\hat{x}\hat{y}$-plane is given by Eq. (14). Assuming a symmetric chirp with $O_f = -O_i = \frac{\Delta O}{2}$, $\Delta O = \gamma G_e L_e$ and $R = \frac{\Delta O}{T_e}$, and denoting $k^{(e)}_{\max} = \gamma G_e T_e$,

$$\phi_e(z) = -\frac{k^{(e)}_{\max} z^2}{2L_e} + k^{(e)}_{\max}\left(\frac{1}{2} - \frac{\Omega_1}{\gamma G_e L_e}\right) z + \frac{k^{(e)}_{\max} L\left(1 - \frac{2\Omega_1}{\gamma G_e L_e}\right)^2}{8} + \frac{\pi}{2}. \tag{153}$$

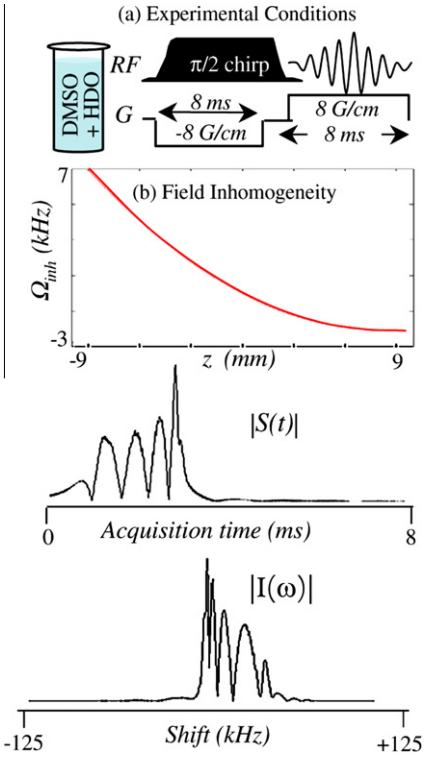

Fig. 53. Attempted chemical shift imaging on a 5 mm sample containing DMSO and HDO, in an inhomogeneous field. The field inhomogeneity, modulus of acquired signal, and modulus of spectral density following phase correction are plotted, showing the impossibility of differentiating between the two spectral peaks.

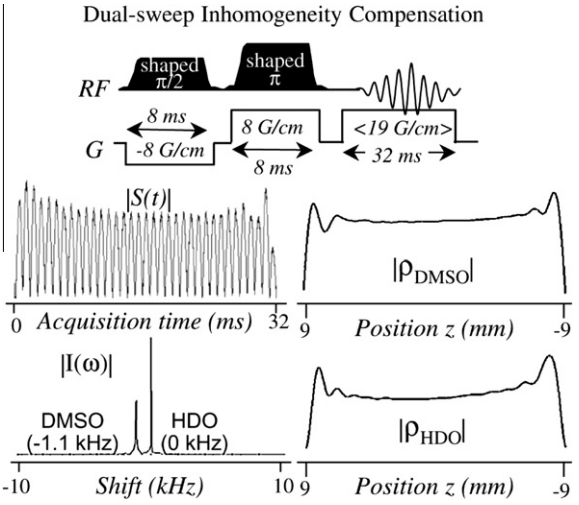

Fig. 54. Chemical shift imaging in inhomogeneous fields with B_0 correction applied. The experiment was carried out on the same sample as in Fig. 53. Two chirped pulses were used, as described in the text, to excite the sample, ensuring the images have a phase with a quadratic term independent of the chemical shift and a linear term proportional to the chemical shift. The acquired signal had its quadratic phase consequently removed, and was Fourier transformed to yield a spectrum, from which the two images – of the DMSO and the HDO – were filtered.

The acquired signal, $s(k,t_2)$, given by applying the stationary phase approximation (Eq. (91)), will then mainly originate from the point z_0 for which the acquisition phase $\phi_a(k,t_2)=\phi_e(z)+kz+\Omega_2 t_2$ is at a minimum: $\frac{d\phi_a}{dz}=0$. Differentiating and equating to zero, one obtains:

$$z_0(k,\Omega_1)=\frac{L}{2}\left(1+\frac{k}{k_{\max}^{(e)}}\right)-\frac{\Omega_1}{\gamma G_e}. \tag{154}$$

Note that this point is a function of k and Ω_1 but not of t_2 or Ω_2. The total phase of the signal $s(t)$, given by $\phi_a(k,t_2)=\phi_e(z_0(k,\Omega_1))+kz_0(k,\Omega_1)+\Omega_2 t_2$, can then be readily computed as

$$\phi_a(k,t_2)=\left[\frac{L_e}{2k_{\max}^{(e)}}k^2+\frac{L_e}{2}k-\frac{\pi}{2}\right]-\frac{\Omega_1}{\gamma G_e}k+\Omega_2 t_2. \tag{155}$$

Observe that, when viewed as a function of k and t_2, this phase appears to naturally separate into three components; one independent of Ω_1 and Ω_2 having both a quadratic and linear dependency on k, one linear in k and Ω_1, and one linear in t_2 and Ω_2. All chemical shifts will thus share the first term (akin to the quadratic time term introduced in Section 6.1), which can therefore be removed via post-acquisition processing. Then, by monitoring the FID in the presence of an alternating gradient, G_a, one can collect data for multiple values of k,t_2. Viewed in the $k-t_2$ plane (Fig. 55c), Eq. (155) implies that the acquired data will be modulated along the k-axis by the indirect domain frequencies, Ω_1, and along the t_2 axis by the direct domain frequencies, Ω_2. A Fourier transform along both axes then yields a 2D spectrum in one scan, as is illustrated in Fig. 55.

7. Summary

Spatial encoding, as encompassing the monitoring of spin evolutions on the basis of selective frequency-swept pulses and of magnetic field gradients, provides a new way for measuring NMR spectra or MRI images. In contrast to time-domain schemes or to continuous-wave approaches, these new RF/gradient combinations can act together to create interaction-dependent spatial patterns of spin magnetizations or coherences extending throughout a sample. These patterns can then be read-out with the aid of a second set of gradients while digitizing the data, to endow NMR/MRI acquisitions with hitherto unavailable capabilities.

The present Review described various facets of these new approaches to monitor NMR spectra and MRI images. We began with a thorough introduction on how to visualize the effects of swept RF pulses – be them of an excitation or refocusing nature – applied in the presence of linear field gradients. It was then discussed how, in a spectroscopic setting, the idea of spatial encoding can be exploited to compress an nD spectroscopic NMR experiment into a single-scan. Numerous acquisition schemes capable of retrieving this kind of results for a variety of 2D experiments were presented, and their relative merits and limitations were surveyed.

Similar ideas were shown to have applications in other spectroscopic paradigms involving multi-scan experiments, such as Hadamard spectroscopy. It was once again shown that by partitioning the sample and exciting different patterns for each site, one could produce a single-scan, sub-second version of a complex experiment. Similar versions of multi-scan phase cycling have also been demonstrated [71].

The final part extended these spatially-selective encoding concepts in what we believe are novel imaging sequences, though related to decades-old developments in this field. By suitable excitation protocols, the spins in the sample can, in these MRI settings, be made to interfere destructively – except within a particular voxel which can be chosen at will. This voxel can be shifted along a predefined trajectory, set by shaping the acquisition gradients, yielding a signal proportional to the spin density along that path. Therefore, spatially encoded imaging differs from conventional Fourier imaging by acquiring images in real rather than in **k**-space. The point-by-point nature of the ensuing approach can

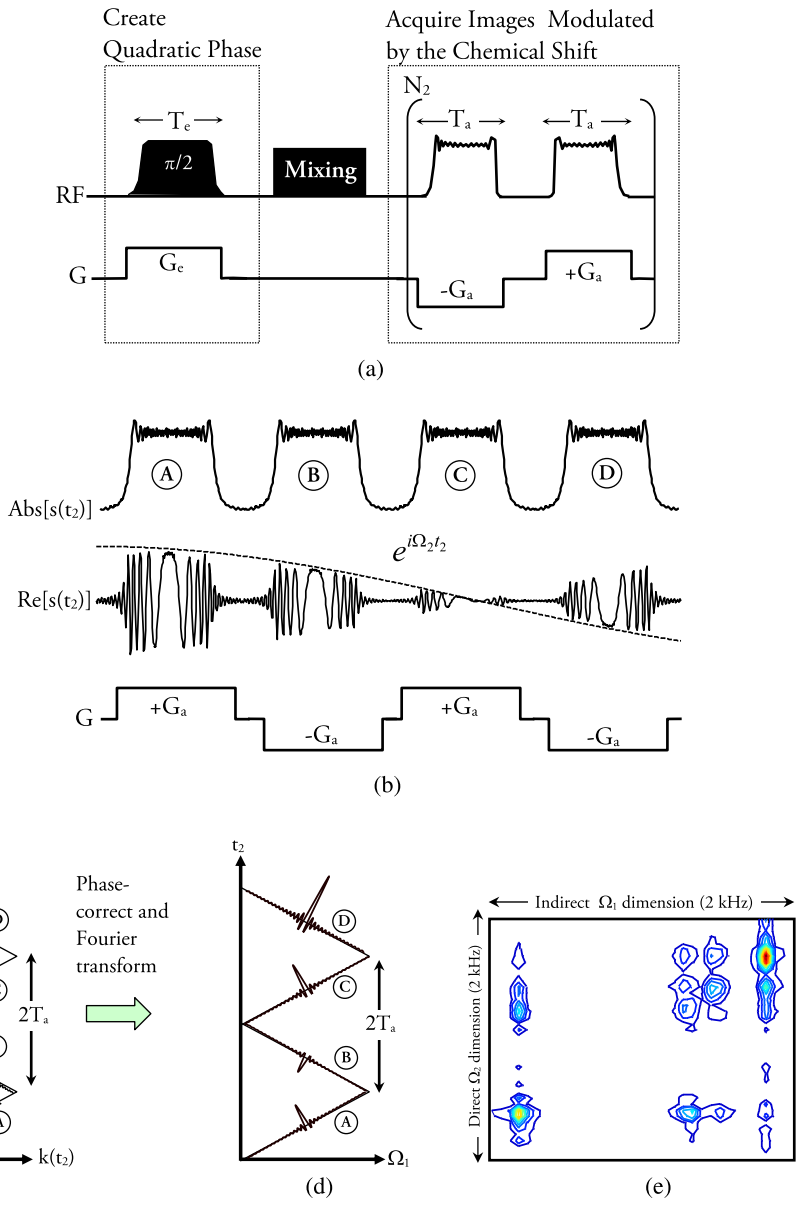

Fig. 55. Single sweep spectroscopy. (a) Pulse sequence used. (b) Both the modulus and the real part of the acquired signal are shown as a function of t_2, the acquisition time, for a particular chemical shift Ω_1 along the indirect domain – the actual signal would consist of a superposition of many such signals which would originate from different Ω_1 and interfere among themselves, as illustrated in Fig. 50a. (c) The signal is arranged along the acquisition trajectory in the $k - t_2$ plane, and consequently phase corrected and Fourier transformed along the k-axis, yielding an echo at Ω_1 (d). From this point onwards, the same post-processing used in UF2DNMR can be applied to extract the 2D spectrum – compare and contrast with Fig. 17. (e) A 2D TOCSY spectrum acquired experimentally using this methodology, on a sample containing n-butylchloride, dissolved in $CDCl_3$. The spectrum was acquired on a 500 MHz Varian iNova spectrometer. Parameters used were $T_e = 19.75$ ms, $G_e = 0.5$ Gauss/cm, a 40 ms DIPSI-2 mixing with a bandwidth of 10 kHz, $N_2 = 40, G_a = 40 \frac{\text{Gauss}}{\text{cm}}$, and a total of 3200 acquisition points.

then address a number of challenging measurements, including the single-scan acquisition of images arising from different chemical sites, or in the presence of field inhomogeneities.

Overall, it is hoped that as the technical details underlying these new methods become clearer and as their user-base expands, further improvements will materialize and new, unforeseen applications of spatial-encoding will emerge – both in the spectroscopy and imaging realms.

Acknowledgements

We are grateful to Drs. Mor Mishkovsky, Yoav Shrot, Patrick Giraudeau, Noam Ben Eliezer and Maayan Gal for the insight and material provided in the compilation of this work. A.T. acknowledges the Clore Foundation for a Graduate Fellowship; L.F. acknowledges support from a Helen and Martin Kimmel Award.

Appendix A. Spatial-spectral pulse design

This appendix concerns itself with the technical details involved in the design of spatial-spectral (SPSP) pulses, such as those used throughout Section 4. While this is a known topic in imaging applications [46], it is not so widely appreciated among NMR spectroscopists, and hence we deemed its inclusion pertinent. Still, the design of such pulses draws from several familiar concepts like the small tip-angle approximation, the associated idea of polychromaticity, and DANTE-like pulses; all of and can be discussed before delving into the particulars of the pulse design involved in customized spatial-spectral encoding.

A.1. Small tip-angle approximation

RF excitation pulses are inherently non-linear in nature: the effect of a pulse is not proportional to its duration or power. For example, applying a particular on-resonance irradiation for a given duration might tip the spins by 90° and result in maximal signal, but doubling the intensity of that RF will not double the signal strength; on the contrary, it will tip the spins by 180°, and the signal will correspondingly drop back to zero. However, for small tip angles, there exists a linear relationship [47] between the applied RF as a function of time, $B_1(t)$, and the resulting spin profile in the $\hat{x}\hat{y}$-plane as a function of frequency, $M_+(\omega)$; namely, that $M_+(\omega)$ is then proportional to the Fourier transform of $B_1(t)$:

$$M_+^{(f)}(\omega) = \imath M_0 e^{-\imath\frac{\omega t_p}{2}} \int_{-\infty}^{\infty} \widetilde{B}_1(t) e^{-\imath\omega t} dt + M_+^{(i)}(\omega) e^{-\imath\omega t_p}, \tag{156}$$

where $M_+^{(i)}(\omega)$ is the distribution of spins in the $\hat{x}\hat{y}$-plane as a function of offset prior to the pulse, $M_+^{(f)}(\omega)$ is the distribution resulting after applying the RF pulse, M_0 is the equilibrium value of the magnetization and $B_1(t)$ is the RF pulse as a function of time. When starting out from equilibrium, $M_{xy}^{(i)}(\omega) = M_0$, but in general these two quantities are independent, and $M_{xy}^{(i)}(\omega)$ can assume any form – it can, for example, equal the distribution created by a previous RF pulse, if such was applied. Note that $M_+^{(i)}(\omega), M_+^{(f)}(\omega), B_1(t)$ are all complex numbers which describe a vector lying in the $\hat{x}\hat{y}$-plane of the Bloch sphere, where the real part signifies the x-component of the vector and the imaginary part signifies its y-component. Furthermore, the quantity $\widetilde{B}(t)$ has been introduced, which is obtained by centering $B_1(t)$ about $t = 0$; that is, if $B_1(t)$ is non-zero in the interval $[0, T_p]$, then $\widetilde{B}(t) \equiv B\left(t - \frac{T_p}{2}\right)$.

The existence of a Fourier relationship between the excitation profile and the RF pulse facilitates the design of many simple excitation pulses. For example, to excite a sinc-like shape of width $\Delta\omega$ in frequency space, one needs to use a rectangular RF pulse of duration $\sim \frac{1}{\Delta\omega}$, which is the Fourier transform of the sinc function. Eq. (156) also furnishes an arsenal of useful design tools, all a direct application of well known Fourier transform relations. For example, to shift the excitation pattern in frequency space by an amount $\delta\omega$, the RF pulse needs to be multiplied by a linearly increasing phase $B_1(t) \to B_1(t)e^{\imath\delta\omega t}$. These approximations are also used to design spatially selective pulses, as a soft pulse which excites a region $[\nu_a, \nu_b]$ in frequency space will excite a region $[z_a, z_b]$ in real space once a gradient G is applied, where $z_a = \frac{\nu_a}{\gamma G}, z_b = \frac{\nu_b}{\gamma G}$. Despite its name, the small tip-angle approximation holds even for fairly large pulse angles – up to 90° – to a remarkably good degree.

A.2. Polychromaticity

The linearity of the small tip angle approximation reveals that, if two excitation pulses $B_{1,a}(t), B_{1,b}(t)$ with corresponding excitation profiles $M_+^{(a)}(\omega), M_+^{(b)}(\omega)$ are added up, then the combined RF pulse $B_1^{(\Sigma)}(t) = B_{1,a}(t) + B_{1,b}(t)$ will lead to an excitation profile given by $M_+^{(\Sigma)}(\omega) = M_+^{(a)}(\omega) + M_+^{(b)}(\omega)$. It turns out that this holds even for large flip angles, so long as the pulses address different regions in frequency space. Pulses created this way, by adding independent sub-pulses, are termed polychromatic pulses [72,73]. The concept of polychromaticity is very powerful. As an example, consider a pulse $B_1(t)$ which excites a particular region in frequency space, centered about ν_0 and having a width $\Delta\nu$. By forming, for example, $B_1(t) - B_1(t)e^{\imath 2\pi\delta\nu t}$, one can excite simultaneously two regions of width $\Delta\nu$, one centered around ν_0 and the other about $\nu_0 + \delta\nu$, with opposite phases (see Fig. 56).

A.3. DANTE pulses

An intuitive approach to selective excitation is presented by the DANTE sequence [74], which consists of a train of small-tip-angle pulses spaced Δt apart. As DANTE will also be a common ingredient of spatial-spectral RF pulses, such a train is briefly outlined in Fig. 57a, along with the corresponding pattern excited in frequency space in Fig. 57b. In particular, observe the following:

- The excitation profile is repetitive both in time and in frequency, and is modulated in the latter by an envelope (the dashed line in Fig. 57b).
- There are three timescales involved; the duration of each hard pulse, δt, the spacing between the pulses, Δt, and the total duration of the train, $T_a = N(\Delta t + \delta t)$, where N is the number of hard-pulses applied. Correspondingly, there are three frequency scales in the excitation profile; the width of each peak, $\sim \frac{1}{T_a}$, the distance between peaks, $\sim \frac{1}{\Delta t}$ and the width of the outer envelope, $\sim \frac{1}{\delta t}$.
- The shape of the outer envelope (the dashed line in Fig. 57b) is given by the Fourier transform of an individual pulse. In Fig. 57, the pulses have rectangular shapes, so the overall envelope is sinc-like.
- The shape of each excitation peak is given by Fourier transforming the overall envelope of the pulse. In Fig. 57a, the envelope is rectangular (not explicitly drawn), and hence each peak in Fig. 57b is sinc-like.
- The position of the central lobe in Fig. 57b in frequency space is determined by the phases of the hard-pulses in Fig. 57a. In particular, it is possible – as it is with any small tip angle excitation pulse – to introduce a linearly increasing phase $e^{\imath k\alpha}$ to the kth peak, which will shift the entire pattern by an amount $\Delta\nu = \frac{\alpha}{\Delta t + \delta t}$.

All of these features can be readily explained by using the small tip angle approximation and merely Fourier transforming the pulse train in Fig. 57a to obtain the pattern shown in Fig. 57b.

DANTE pulses can be employed to excite a certain frequency region as follows. First, choose the total length of the pulse, $T_a = N(\Delta t + \delta t)$, such that the width of each excitation peak $\frac{1}{T_a}$ is equal to the width of the region to be excited in frequency space. Then, choose Δt small enough that the spacing $\frac{1}{\Delta t}$ is larger than twice the spectral width of the sample; this ensures there is only one excitation lobe within the spectral range of the sample. Finally, choose the desired center frequency ν_0 to be excited, by adding a linear phase $e^{\imath k\alpha}$ to the pulses. This centers the lobe around the frequency range $\nu_0 \pm \frac{\Delta\nu}{2}$ that we wish to excite.

A.4. The design of spatial-spectral pulses

The three concepts presented – the small tip angle approximation, polychromaticity and DANTE pulses – tie in together in the design of spatial-spectral pulses capable of exciting a SPSP-pattern as shown, for example, in Fig. 29. According to the principle of polychromaticity, instead of designing a single pulse with that profile, one can design a pulse capable of exciting a particular well-defined region in the (z, ν) plane of dimensions $\Delta z \times \Delta\nu$, centered about some point (z_0, ν_0), and then add the pulses up. For example, exciting the pattern in Fig. 29b would entail generating and adding up 16 RF pulses with appropriate phases: $B(t) = \sum_{k=1}^{4}\sum_{p=1}^{4} e^{\imath\eta_{k,p}} B_{k,p}(t)$, where $B_{k,p}(t)$ is designed to excite the kth peak in the pth slice and $\eta_{k,p}$ is set to either 0 or π to mimic the form of a Hadamard matrix. The original problem has thus been reduced to the problem of designing $4 \times 4 = 16$ pulses $B_{k,p}(t)$, selective in both position and frequency.

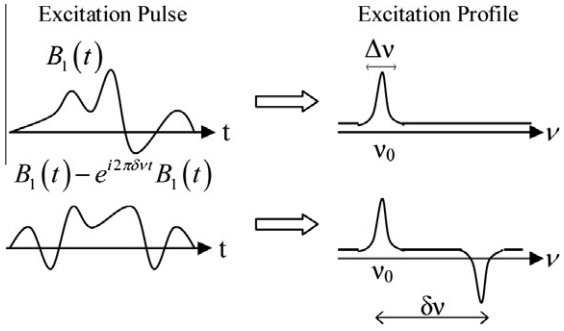

Fig. 56. Polychromatic pulses rely on the principle of superposition: the frequency response of the vectorial sum of two RF fields equals the sum of their individual responses provided they do not overlap. On the top row, a particular RF field is given, with its frequency response plotted on the right. On the bottom row, that field is reproduced with a phase $-e^{i2\pi\delta\nu t}$, which shifts and inverts its frequency response, and then adds to itself. The resulting response, shown on the right, is the sum of the individual responses.

By using the small tip angle approximation, one can devise a pulse that will excite a slab of thickness Δz, centered about z_0, in the presence of a gradient G. The precise form of the pulse will depend on the desired profile. For example, if a rectangular region is to be excited, a truncated sinc pulse of duration $t_c \equiv \frac{1}{\gamma G \Delta z}$ should be used, $B_1(t) \propto \mathrm{sinc}\left[\gamma G \Delta z\left(t - \frac{t_c}{2}\right)\right] e^{i\gamma G z_0 t}$. Note the linear phase $e^{i\gamma G z_0 t}$, which maintains the profile's center at z_0. As the sinc pulse is infinite in its extent it must be truncated, and this truncation will lead to an imperfect rectangular profile. Such issues can be addressed by the many optimization schemes that abound in the literature [36,75,37]; the full range of that discussion is outside the scope of this review.

Having chosen an approach to designing a spatially selective pulse (e.g., the linear approximation), there is still the problem of spectral selectivity to be dealt with. Applied as-is, the aforementioned $B_1(t)$ would excite all chemical shifts in the chosen slice equally. To remedy this problem, the spatial pulse is partitioned into N identical copies, each of tip angle $\frac{\pi/2}{N}$, and each is applied during the positive iteration of an alternating excitation gradient, as illustrated in Fig. 58. To gain an understanding of how this affords spectral selectivity, consider the phase acquired by a spin in the sample having position z and chemical shift ω_0:

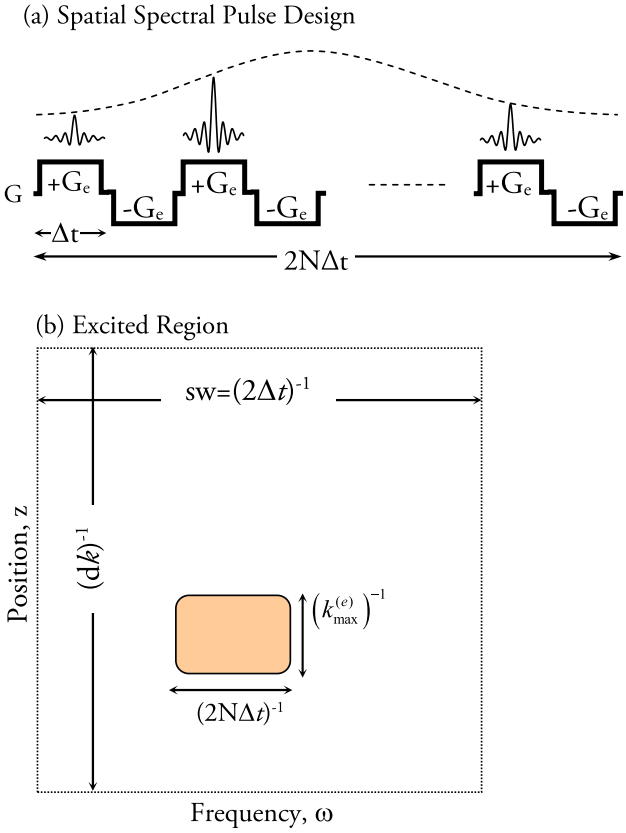

Fig. 58. The design of a spatial-spectral pulse. A spatially selective pulse is partitioned into N identical copies and applied in the presence of an alternating gradient. Here, δt is the duration of the positive lobe of the applied gradient and Δt is the duration of the negative lobe, where $\delta t = \Delta t$. By definition, $k_{\max} = \gamma G_e T_e$, the maximal value of $k^{(e)}(t) = \gamma \int G_e(t')dt'$ attained throughout excitation. A notational distinction has been made in order to emphasize the similarity with that of Fig. 57a was used. An overall envelope serves to set the spectral excitation pattern, and a linearly increasing phase (not indicated in the figure) serves to center the spectral excitation lobe.

$$\phi(t) = \omega_0 t + k(t)z, \tag{157}$$

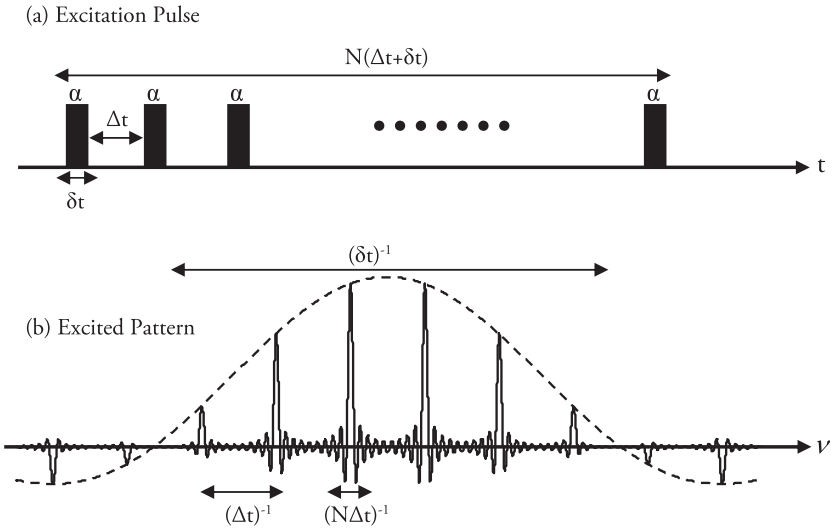

Fig. 57. (a) The DANTE excitation sequence consists of a train of equispaced pulses. The pulses can have any shape, and can also be modulated by an arbitrary overall envelope. In the above figure the shape of the pulses is rectangular, and the envelope is also rectangular. (b) The corresponding frequency response of the pulse shown in (a). It consists of a basic form – the shape of which is the Fourier transform of the envelope in (a), in this case a sinc – repeated infinitely in both directions, with an overall modulation given by the Fourier transform of a single pulse in (a), which is once again a sinc.

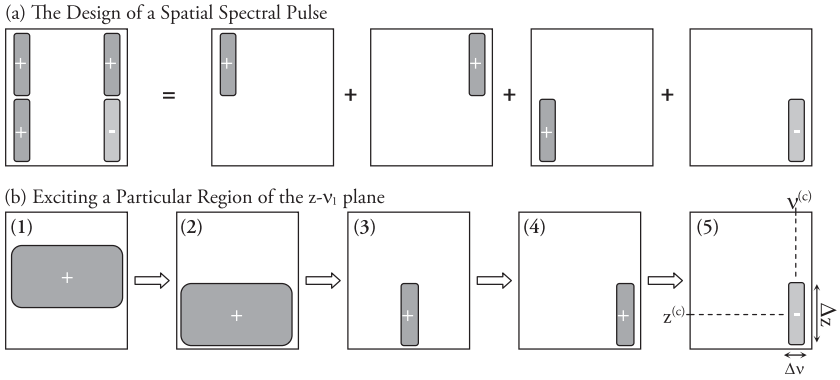

Fig. 59. (a) A spatial-spectral Hadamard pattern in the $z - v_1$ plane can be created by adding up individual spatial-spectral RF pulses, each exciting a particular region and phase. (b) The individual RF pulses can be constructed by first designing a spatially selective pulse (1), shifting it (2) by multiplying it by a linear phase, and then employing a DANTE-like pulse-train design to create the spectral selectivity (3) and shifting it (4) by multiplying the kth pulse in the train by $e^{ik2T_e v_{shift}}$. Finally, the entire pulse can be multiplied by the phase (5) corresponding to the appropriate element in the Hadamard matrix.

where, as previously noted, $k(t) = \gamma \int_0^t G(t')dt'$. Note that the total phase acquired between two temporal points during the excitation, $\Delta t + \delta t$ apart, is merely

$$\Delta\phi = \omega_0(\delta t + \Delta t). \tag{158}$$

Since that temporal distance corresponds to a single gradient period, the total area bound by it equals zero. Eq. (158) reveals that, while in each gradient iteration the pulse serves to excite a well defined spatial region, the overall evolution on a timescale larger than a single gradient iteration is dictated by a spin's chemical shift alone; in other words, all spins having the same chemical shift will be affected by the overall envelope of the pulse similarly, regardless of their position. This is a convenient way of separating the spatial selectivity from the spectral one.

In effect, the design shown in Fig. 58 mimics that of the DANTE pulse shown in Fig. 57: like the DANTE, the gradient-refocused structure will target a spin's chemical shift, regardless of its position. In accordance with the discussion previously presented for DANTE pulses, one can single out a region of interest in frequency space: by choosing $T_a \equiv N(\Delta t + \delta t)$, one excites a region of width $\Delta v \approx \frac{1}{T_a}$; by taking Δt to be small enough, the spacing $\frac{1}{\Delta t}$ can be made larger than twice the spectral width of the sample, making the excitation unequivocal and ensuring that no other peaks outside the region Δv are targeted; and, finally, by adding a linear phase to the peaks, one can choose the desired center frequency v_0 one wishes to excite. All this ensures that one excites a region $v_0 \pm \frac{\Delta v}{2}$ – and nothing else. Notice also that there is a minor difference between Figs. 58 and 57: an overall envelope has been added in Fig. 58. As previously discussed, the Fourier transform of this envelope dictates the spectral excitation profile. In Fig. 58a Gaussian envelope has been chosen, which will result in a Gaussian region being excited about the central frequency.

A spatial-spectral pulse capable of exciting a desired Hadamard pattern – for example, the one in Fig. 31b – can be constructed by adding RF pulses polychromatically, each of which excites a well-defined region in the $z - v_1$ plane with a phase corresponding to an entry in the Hadamard matrix, as shown in Fig. 59a. Thus, the problem of designing such a pulse can be reduced to the problem of designing a single RF pulse, capable of exciting a given region of dimensions $\Delta z \times \Delta v$ centered around a particular point $(z^{(c)}, v^{(c)})$ in the $z - v_1$ plane. The design of such a pulse is described next. The design process is outlined in Fig. 59b, with the steps elaborated upon in detail below.

1. A spatially-selective pulse, $B_{spat}(t)$, is created, which excites a slice of width Δz (Fig. 59b-1). Denoting by L the physical length of the sample, one has $\frac{L}{\Delta z} = N_{peaks}$, as a total of N_{peaks} slices are needed to parallelize the 2D Hadamard experiment. To ensure the desired selectivity, one sets $k_{max}^{(e)} \equiv \gamma G_e T_e = \frac{2\pi}{\Delta z}, dk^{(e)} \equiv \gamma G_e dt = \frac{2\pi}{L}$ (see Fig. 58), where dt is the physical dwell time during acquisition, T_e the total pulse duration and G_e the excitation gradient. As T_e will be set below by the spectral requirements, it can be treated as a constant. Solving for Ge and dt yields:

$$\gamma G_e = \frac{2\pi N_{peaks}}{LT_e}, \tag{159}$$

$$dt = \frac{2\pi}{\gamma G_e L}. \tag{160}$$

Note that the ratio $\frac{T_e}{dt}$ is equal to the number of points used to digitize $B_{spat}(t)$. The Fourier transform of the shape of $B_{spat}(t)$ is used to determine the profile of the excited region. For example,

$$B_{spat}(t) = \begin{cases} B_{spat,0} \exp\left[-\left(\alpha\Delta\Omega\left(t - \frac{T_e}{2}\right)\right)^2\right] & \text{for } 0 \leqslant t \leqslant T_e \\ 0 & \text{otherwise} \end{cases}, \tag{161}$$

would result in a Gaussian profile.[26] For simplicity, the RF pulse should be kept real and symmetrical about $\frac{T_e}{2}$.

2. Center the spatial excitation profile about $z^{(c)}$ (Fig. 59b-2):

$$B_{spat}^{(shifted)}(t) = B_{spat}(t)e^{i\gamma G_e z^{(c)} t}. \tag{162}$$

3. Introduce spectral selectivity (Fig. 59b-3) by oscillating the gradient G_e, as shown in Fig. 58, and apply $B_{spat}^{(shifted)}(t)$ during each positive gradient lobe. To ensure sufficient selectivity along the v_1 frequency axis, choose $N_1 = (2T_e\Delta v)$, where N_1 is the number of repetitions of the gradient; and to guarantee that the DANTE-type spectral excitation does not target additional peaks within the indirect spectral width SW_1, select $T_e = \frac{1}{2SW_1}$. The form of the resulting spatial-spectral RF pulse is:

$$B_{SPSP}(t) = \sum_{k=0}^{N_1} A_k B_{spat}^{(shifted)}(t - 2kT_e). \tag{163}$$

The discrete Fourier transform of the envelope defined by $A_0, A_1, \ldots, A_{N_1-1}$ is proportional to the shape of the spectral profile.

[26] α is a factor – equal to approximately 3 for a Gaussian excitation – inserted to calibrate the full width at half height (FWHH) of the profile. $B_{spat,0}$ is used to calibrate the pulse tilt angle.

4. Center the spectral profile about $\nu^{(c)}$ (Fig. 59b-4) by multiplying each pulse in the train by a piecewise constant phase:

$$B_{SPSP}^{(shifted)}(t) = \sum_{k=0}^{N_1} A_k e^{ik\nu^{(c)}2T_e} B_{spat}^{(shifted)}(t - 2kT_e). \quad (164)$$

5. Introduce the desired phase ϕ (Fig. 59b-5) – determined by the appropriate entry in the Hadamard matrix – by multiplying $B_{SPSP}^{(shifted)}(t)$ by $e^{i\phi}$.

References

[1] F. Bloch, Nuclear induction, Phys. Rev. 70 (1946) 460.
[2] D.M. Grant, R.K. Harris (Eds.), Encyclopedia of NMR, John Wiley & Sons, 1996.
[3] M.H. Levitt, Spin Dynamics, John Wiley & Sons, 2008.
[4] P.C. Lauterbur, Image formation by induced local interactions: examples employing NMR, Nature 6 (1973) L422.
[5] R. Damadian, Tumor detection by nuclear magnetic resonance, Science 171 (1971) 1151.
[6] P. Mansfield, P.K. Grannell, NMR 'diffraction' in solids?, J Phys. C Solid State Phys. 6 (1973) L422.
[7] L. Frydman, A. Lupulescu, T. Scherf, Principles and features of single-scan two-dimensional NMR spectroscopy, J. Am. Chem. Soc. 125 (2003) 9204–9217.
[8] L. Frydman, T. Scherf, A. Lupulescu, The acquisition of multidimensional NMR spectra within a single scan, Proc. Natl. Acad. Sci. USA 99 (2002) 15858–15862.
[9] Y. Shrot, L. Frydman, Single-scan NMR spectroscopy at arbitrary dimensions, J. Am. Chem. Soc. 125 (2003) 11385–11396.
[10] Y. Shrot, L. Frydman, Spatially encoded NMR and the acquisition of 2D magnetic resonance images within a single scan, J. Magn. Res. 172 (2005) 179–190.
[11] A. Tal, L. Frydman, Spatial encoding and the single-scan acquisition of high definition MR images in inhomogeneous fields, J. Magn. Res. 182 (2006) 179–194.
[12] A. Tal, L. Frydman, Spectroscopic imaging from spatially encoded single-scan multidimensional MRI data, J. Magn. Res. 189 (2007) 46–58.
[13] J. Jeener, Ampere International Summer School II, Tech. rep., Basko Polje, Yugoslavia, 1971.
[14] R.R. Ernst, Application of Fourier transform spectroscopy to magnetic resonance, Rev. Sci. Instrum. 37 (1966) 93.
[15] L. Braunschweiler, R.R. Ernst, Coherence transfer by isotropic mixing: application to proton correlation spectroscopy, J. Magn. Res. 53 (1983) 521–528.
[16] W.P. Aue, E. Bartholdi, R.R. Ernst, Two-dimensional spectroscopy. Application to nuclear magnetic resonance, J. Chem. Phys. 64 (1976) 2229–2246.
[17] A. Bax, R. Freeman, Investigation of complex networks of spin–spin coupling by two-dimensional NMR, J. Magn. Res. 44 (1981) 542.
[18] G. Bodenhausen, D.J. Ruben, Natural abundance nitrogen-15 NMR by enhanced heteronuclear spectroscopy, J. Chem. Phys. Lett. 69 (1980) 185–199.
[19] L. Muller, Sensitivity enhanced detection of weak nuclei using heteronuclear multiple quantum coherence, J. Am. Chem. Soc. 101 (1979) 4481–4484.
[20] S. Macura, R.R. Ernst, Elucidation of cross relaxation in liquids by two-dimensional NMR spectroscopy, Mol. Phys. 41 (1980) 95–117.
[21] J. Jeener, B.H. Meier, P. Bachmann, R.R. Ernst, Investigation of exchange processes by two-dimensional spectroscopy, J. Chem. Phys. 71 (1979) 4546–4553.
[22] B. Shapira, A. Lupulescu, Y. Shrot, L. Frydman, Lineshape considerations in Ultrafast 2D NMR, J. Magn. Res. 166 (2004) 152–163.
[23] M. Garwood, L. DelaBarre, The return of the frequency sweep: designing adiabatic pulses for contemporary NMR, J. Magn. Res. 153 (2001) 155–177.
[24] C.P. Slichter, Principles of Magnetic Resonance, third ed., Springer-Verlag, 1992.
[25] J.M. Boehlen, I. Burghardt, M. Rey, G. Bodenhausen, Frequency-modulated "chirp" pulses for broadband inversion recovery in magnetic resonance, J. Magn. Res. 90 (1990) 183–191.
[26] R. Fu, G. Bodenhausen, Broadband decoupling in NMR with frequency-modulated 'chirp' pulses, Chem. Phys. Lett. 245 (1995) 415–420.
[27] A. Abragam, Principles of Nuclear Magnetism, Oxford University Press, 1983.
[28] M. Deschamps, G. Kervern, D. Massiot, G. Pintacuda, L. Emsley, P.J. Grandinetti, Superadiabaticity in magnetic resonance, J. Chem. Phys. 129 (2008) 204110.
[29] N.S. Andersen, W. Kockenberger, A simple approach for phase-modulated single-scan 2D NMR spectroscopy, Magn. Reson. Chem. 43 (2005) 795–797.
[30] B. Shapira, Y. Shrot, L. Frydman, Symmetric spatial encoding in Ultrafast 2D NMR spectroscopy, J. Magn. Res. 178 (2006) 33–41.
[31] Y. Shrot, A. Tal, L. Frydman, New developments in the spatial encoding of spin interactions for single-scan 2D NMR, Magn. Res. Chem. 47 (2009) 415–422.
[32] Y. Shrot, L. Frydman, Ultrafast two-dimensional NMR spectroscopy using constant acquisition gradients, J. Chem. Phys. 125 (2006) 204507.
[33] A. Tal, B. Shapira, L. Frydman, A continuous phase-modulated approach to spatial encoding in Ultrafast 2D NMR spectroscopy, J. Magn. Res. 176 (2005) 107–114.
[34] Y. Shrot, B. Shapira, L. Frydman, Ultrafast 2D NMR spectroscopy using a continuous spatial encoding of the spin interactions, J. Magn. Res. 171 (2004) 162–169.
[35] P. Pelupessy, Adiabatic single-scan two-dimensional NMR spectroscopy, J. Am. Chem. Soc. 125 (2003) 12345.
[36] J.M. Pauly, P.Le Roux, D. Nishimura, A. Macovski, Parameter relations for the Shinnar-Le Roux selective excitation pulse design algorithm, IEEE Trans. Med. Imaging 10 (1991) 53–65.
[37] N. Gershenzon, K. Kobzar, B. Luy, S. Glaser, T. Skinner, Optimal control design of excitation pulses that accommodate relaxation, J. Magn. Res. 188 (2007) 330–336.
[38] Y. Shrot, L. Frydman, The effects of molecular diffusion in ultrafast two-dimensional nuclear magnetic resonance, J. Chem. Phys. 128 (2008) 164513.
[39] P. Mansfield, Spatial mapping of chemical shifts in NMR, Magn. Res. Med. 1 (1984) 370.
[40] M. Unser, Sampling – 50 years after Shannon, Proc. IEEE 88 (2000) 569–587.
[41] P. Giraudeau, S. Akoka, Sensitivity losses and line shape modifications due to molecular diffusion in continuous encoding Ultrafast 2D NMR experiments, J. Magn. Res. 192 (2008) 151.
[42] Y. Shrot, L. Frydman, Spatial encoding strategies for Ultrafast multidimentional nuclear magnetic resonance, J. Chem. Phys. 128 (2008) 052209.
[43] M. Gal, M. Mishkovsky, L. Frydman, Real time monitoring of chemical transformation by ultrafast 2D NMR spectroscopy, J. Am. Chem. Soc. 128 (2006) 951–956.
[44] M. Mishkovsky, L. Frydman, Progress in hyperpolarized Ultrafast 2D NMR spectroscopy, Chem. Phys. Chem. 9 (2008) 2340–2348.
[45] L. Frydman, D. Blazina, Ultrafast two-dimensional nuclear magnetic resonance spectroscopy of hyperpolarized solutions, Nat. Phys. 3 (2007) 415–419.
[46] C.H. Meyer, J.M. Pauly, A. Macovski, D.G. Nishimura, Simultaneous spatial and spectral selective excitation, Magn. Res. Med. 15 (1990) 287–304.
[47] J. Pauly, D. Nishimura, A. Macovski, A *k*-space analysis of small tip angle excitation, J. Magn. Res. 81 (1989) 43.
[48] E. Kupce, R. Freeman, Two-dimensional Hadamard spectroscopy, J. Magn. Res. 162 (2003) 300–310.
[49] E. Kupce, R. Freeman, Frequency-domain Hadamard spectroscopy, J. Magn. Res. 162 (2003) 158–165.
[50] E. Kupce, T. Nishida, R. Freeman, Hadamard NMR spectroscopy, Prog. NMR Spectrosc. 42 (2003) 95–122.
[51] E.D. Nelson, M.L. Fredman, Hadamard spectroscopy, J. Opt. Soc. Am. 60 (1970) 1664–1669.
[52] E. Kupce, R. Freeman, Fast multidimensional NMR of proteins, J. Biomol. NMR 25 (2003) 349–354.
[53] J. Hadamard, Resolution dune question relative aux determinants, Bull. Sci. Math. 17 (1893) 240.
[54] R.E.A.C. Paley, On orthogonal matrices, J. Math. Phys. 12 (1933) 311–320.
[55] R.R. Ernst, G. Bodenhausen, A. Wokaun, Principles of Nuclear Magnetic Resonance in One and Two Dimensions, Oxford University Press, 1987.
[56] W. Tadej, K. Zyczkowski, A concise guide to complex Hadamard matrices, Open Syst. Inform. Dynam. 13 (2006) 133–177.
[57] Y. Shrot, L. Frydman, Spatial/spectral encoding of the spin interactions in ultrafast multidimensional NMR, J. Chem. Phys. 131 (2009) 224516.
[58] A.D. Elster, Gradient-echo MR imaging: techniques and acronyms, Radiology 186 (1993) 1–8.
[59] P.V.D. Meulen, J.P. Groen, J.M. Cuppen, Very fast MR imaging by field echoes and small angle excitation, Magn. Res. Imaging 3 (1985) 297–299.
[60] P. Mansfield, Multi-planar imaging formation using NMR spin-echo, J. Phys. C Solid State Phys. 10 (1977) L55–L58.
[61] C.B. Ahn, J.H. Kim, Z.H. Cho, High speed spiral-scan echo planar imaging, IEEE Trans. Med. Imaging MI-5 (1986) 2.
[62] F. Schmitt, M.K. Stehling, R. Turner, Echo Planar Imaging: Theory, Technique and Application, Springer-Verlag, Berlin, 1998.
[63] F. Farzaneh, S.J. Riederer, N.J. Pelc, Analysis of T_2 limitations and off-resonance effects on spatial solution and artifacts in echo-planar imaging, Magn. Res. Med. 14 (1990) 123–139.
[64] V. Guillemin, S. Sternberg, Geometric Asymptotics, AMS, 1977.
[65] S. Kunis, Nonequispaced FFT generalisation and inversion, Ph.D. thesis, University of Lubeck, Germany, 2006.
[66] N.B. Eliezer, Y. Shrot, L. Frydman, High-definition, single-scan 2D MRI in inhomogeneous fields using spatial encoding methods, Magn. Reson. Imaging 28 (2010) 77–86.
[67] R. Chamberlain, J.-Y. Park, C. Corum, E. Yacoub, K. Ugurbil, C.R. Jack Jr., M. Garwood, Raser: a new ultrafast magnetic resonance imaging method, Magn. Reson. Med. 58 (2007) 794–799.
[68] D.I. Hoult, R.E. Richards, The signal-to-noise ratio of the nuclear magnetic resonance experiment, J. Magn. Res. 24 (1976) 71.
[69] T.R. Brown, B.M. Kincaid, K. Ugurbil, NMR chemical shift imaging in three dimensions, Proc. Natl. Acad. Sci. 79 (1982) 3523.
[70] R.E. Sepponen, J.T. Sipponen, J.I. Tanttu, A method for chemical shift imaging: demonstration of bone marrow involvement with proton chemical shift imaging, J. Comput. Assist. Tomogr. 8 (1984) 58.
[71] D.M. Parish, T. Szyperski, Simultaneously cycled NMR spectroscopy, J. Am. Chem. Soc. 130 (2008) 4925–4933.
[72] E. Kupce, R. Freeman, Polychromatic selective pulses, J. Magn. Res. A 102 (1993) 122–126.

[73] E. Kupce, R. Freeman, Wideband excitation with polychromatic pulses, J. Magn. Res. A 108 (1994) 268–273.
[74] G.A. Morris, R. Freeman, Selective excitation in Fourier transform nuclear magnetic resonance, J. Magn. Res. 29 (1978) 433–462.
[75] J. Magland, C.L. Epstein, Practical pulse synthesis via the discrete inverse scattering transform, J. Magn. Res. 172 (2005) 63–78.
[76] M. Mishkovsky, L. Frydman, Interlaced Fourier transformation of Ultrafast 2D NMR data, J. Magn. Res. 173 (2005) 344–350.
[77] N. Ben-Eliezer, M. Irani, L. Frydman, Super-resolved spatially-encoded single-scan 2D MRI, Magn. Reson. Med. 63 (2010) 1594–1600.
[78] E. Kupce, R. Freeman, An adaptable NMR broadband decoupling scheme, Chem. Phys. Lett. 250 (1996) 523–527.

Glossary

AM: Amplitude Modulated
COSY: COrrelation SpectroscopY
CSI: Chemical Shift Imaging
DANTE: Delays Alternating with Nutations for Tailored Excitations
DIPSI: Decoupling In the Presence of Scalar Interactions
EPI: Echo Planar Imaging
EPSI: Echo Planar Spectroscopic Imaging
EXSY: EXchange SpectroscopY
fbw: Filter Bandwidth
FID: Free Induction Decay
FM: Frequency Modulated
FOV: Field Of View
FT: Fourier Transform
FWHH: Full Width at Half Height
GRE: Gradient Echo
HSQC: Heteronuclear Single Quantum Coherence
HMQC: Heteronuclear Multiple Quantum Coherence
MRI: Magnetic Resonance Imaging
MRS: Magnetic Resonance Spectroscopy
nD: *n*-Dimensional
NMR: Nuclear Magnetic Resonance
NOESY: Nuclear Overhauser Effect SpectroscopY
PM: Phase Modulated
SNR: Signal- to-Noise Ratio
UF: UltraFast
UFNMR: UltraFast 2D Nuclear Magnetic Resonance
SPEN MRI: Spatially Encoded Magnetic Resonance Imaging
RF: Radio Frequency
SLR: Shinnar-Le Roux RF pulse design algorithm
SPSP: SPatial-SPectral
SW: Spectral Width
TOCSY: TOtal Correlation SpectroscopY